Elsevier Editorial System(tm) for Geochimica et Cosmochimica Acta

Manuscript Draft

Manuscript Number: GCA-D-19-00862R1

Title: Aluminium distribution in an Earth's non-primitive lower mantle

Article Type: Article

Corresponding Author: Dr. Costanza Bonadiman, PhD

Corresponding Author's Institution: University of Ferrara

First Author: Marcello Merli, PhD

Order of Authors: Marcello Merli, PhD; Costanza Bonadiman, PhD; Alessandro Pavese, PhD

Abstract: The aluminium incorporation mechanism of perovskite was explored by means of quantum mechanics in combination with equilibrium/off-equilibrium thermodynamics under the pressure-temperature conditions of the Earth's lower mantle (from 24 to 80 GPa). Earth's lower mantle was modelled as a geochemically "not-primitive" object because of an enrichment by 3 wt% of recycled crustal material (MORB-component). The chemical composition of the "non primitive" lower mantle takes into account both chondrite and pyrolite reference models to represent the lower mantle's primitive composition.
The capacity of perovskite to host Al was modelled through an Al2O3 exchange process in an unconstrained Mg-perovskite+Mg-Al-perovskite+free-Al2O3(corundum) system. Aluminium is globally incorporated principally via an increase in the amount of Al-bearing perovskite [Mg-Al-pv(80 GPa)/Mg-Al-pv(24 GPa)□1.17], rather than by an increase in the Al2O3-content of the average chemical composition which changes little (0.11-0.13, mole fraction of Al2O3) and tends to decrease in Al. The Al2O3 distribution in the lower mantle was described through the probability of the occurrence of given compositions of Al-bearing perovskite. The probability of finding Mg-Al-perovskite is comparable to Al-free Mg-perovskite's. Perovskite with Al2O3 mole fraction up to 0.15 has an occurrence probability of ~28% at 24 GPa, increasing up to ~43% at 80 GPa; on the contrary, perovskite compositions in the range 0.19-0.30 Al2O3 mole fraction drop their occurrence probability from 9.8 to 2.0%, over the same P-range. In light of this, the distribution of Al in the lower mantle shows that, among the possible Al-bearing perovskite phases, the (Mg0.89Al0.11)(Si0.89Al0.11)O3 composition is the likeliest, providing from 5 to 8% of the bulk perovskite in the pressure range from 24 to 80 GPa. The occurrence of the Al-richest composition, i.e. (Mg0.71Al0.29)(Si0.71Al0.29)O3, is a rare event (probability of occurrence < 1.7%). This study predicts that perovskite may globally host Al2O3 in terms of 4.3 and 4.8 wt% (with respect to the non-primitive lower mantle mass), thus accounting for ~ 90% and 100% of the bulk Al2O3 estimated in the framework of pyrolite and chondrite reference models, respectively. A calcium-ferrite-type phase (on the MgAl2O4-NaAlSiO4 join) seems to be the only candidate that can compensate for the 10% gap of the perovskite Al-incorporation capacity, in the case of a pyrolite non-primitive lower mantle model.

Università degli Studi di Ferrara

TO: Geochimica et Cosmochimica Acta -Editor in chief:

Jeffrey Catalano

Dear Editor,

Please find enclosed the revised manuscript "**Aluminum distribution in an Earth's *non–primitive* lower mantle"** by Marcello Merli, Costanza Bonadiman (corresponding author) and Alessandro Pavese for potential publication with Geochimica et Cosmochimica Acta.

The text has been revised according to the Associate Editor's and referees' suggestions.

Thank you very much for your consideration and handling.

For the authors,

Costanza Bonadiman

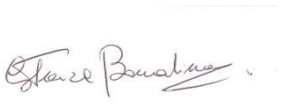

Costanza Bonadiman Physics and Earth Sciences Dept. Polo Scientifico-Tecnologico- University of Ferrara- Via Saragat, 1-44100 Ferrara, Italy . bdc@unife.it

*Response to Comments

TO: Geochimica et Cosmochimica Acta -Editor in chief:

Jeffrey Catalano

Dear Editor,

Please find enclosed the revised manuscript "**Aluminum distribution in an Earth's *non–primitive* lower mantle"** by Marcello Merli, Costanza Bonadiman (corresponding author) and Alessandro Pavese for potential publication with Geochimica et Cosmochimica Acta.

The responses to the Associated Editor and Reviewer's comments, along with the changes introduced in the revised version, are discussed and reported in red below.

With best regards,

Costanza Bonadiman

Associate Editor Report:
Dear Dr. Bonadiman,

The new version of your manuscript entitled "Aluminium distribution in an Earth's non-primitive lower mantle" for which you are corresponding author has been seen by one of the original reviewers and I have also looked through it myself. The reviewer and myself find that you successfully taken into account the vast majority of criticisms made and generally clarified the contribution. However, the reviewer raises a couple of minor issues that would benefit from modification. Furthermore, while I acknowledge that the English has been greatly improved the text still has some rough edges. I would just like to point out line 241 where the word "sheer" is probably not of use, and line 619 where the sentence appears to be missing something.
Reply: The text has been revised accordingly.

Reviewer #1: The authors have addressed all of my concerns, particularly in explaining their model and assumptions in significantly more detail. For example, they have added appendices that describe their procedure and have expanded the methodology section. They have also added references where needed and improved the English throughout the manuscript. Although there are many assumptions in their model, the authors have now explained the reasons for these assumptions (e.g., the choice to omit iron, how the Gibbs free energy was calculated, the omission of thermal/vibrational contributions, and the choice of Mg/Si ratio), and they have changed the wording of the text to be less dismissive of the implications of these assumptions. I believe that the study's findings on aluminum's distribution in the lower mantle is indeed important for our understanding of the chemistry of the deep Earth and combined with their thorough explanation of the methodology, this manuscript would be
a good contribution to GCA. Below are just a couple questions.

- Apologies about the repeated question, but I still don't understand how a saturation of perovskite's capacity
to host aluminum is a sign for a phase transition to post-perovskite when you don't have post-perovskite in your model?
Authors reply: We agree with R1 that care must be paid about the inferences we drew from the *cor*/perovskite ratio. In such a view, we have changed the text of the revised version accordingly and removed any mention to the question above from the Abstract. However, given that we think that these inferences might be an interesting starting point for a further discussion, we have reported, in the "Discussion" section, arguments to uphold our statements (lines 642-650). With this in mind, the caption of Fig.4 has been changed accordingly.

Also, it seems strange to describe that region as quasi-independent of pressure when you fit a polynomial that clearly has a minimum after which you add an arrow upwards to indicate the possibility of an increase in Al2O3 relative to Mg-Al-pv at higher pressure.
Authors reply: We have discussed the nature of the region 60-80 GPa in a more general way, to include the occurrence of a weak *P*-dependence or a poorly defined minimum (lines 565-566). The use of the arrow (Fig.4) is therefore to be considered in the frame of the comment above.

- line 608: "the phase fraction of Mg-Al-pv remarkably grows upon increasing P" -- I'm not sure what is implied by "remarkably" as there is only a modest increase from 0.41 to 0.48.
Authors reply: "Remarkably" has been removed; however, to underline the Al-content change we mention its relative percentage of increase (16%) in the revised version (line 609);

- line 591: if the error is in fact 2.2 kJ/mol for Navrotsky's measurement, your value is in excellent agreement
Authors reply: In the revised version, we stressed that "…observation and theoretical estimate are in good agreement with one another." (line 594).

Aluminium distribution in an Earth's *non–primitive* lower mantle

Marcello Merli[1], Costanza Bonadiman[2*], Alessandro Pavese[3]

[1] *Department of Earth and Marine Sciences, University of Palermo, Via Archirafi 36, 90123 Palermo, Italy.*

[2] *Department of Physics and Earth Sciences, University of Ferrara, Via Saragat 1, 44122 Ferrara, Italy*

[3] *Department of Earth Sciences, University of Turin, Via Valperga Caluso 32, 10100 Turin, Italy*

[*]Correspondence: Costanza Bonadiman

e-mail: costanza.bonadiman@unife.it

Key-words: Aluminium distribution, Earth's lower mantle; aluminium bearing perovskite; pyrolite, chondrite reference model; MORB-component; enriched lower mantle composition; open system.

ABSTRACT

The aluminium incorporation mechanism of perovskite was explored by means of quantum mechanics in combination with equilibrium/off-equilibrium thermodynamics under the pressure-temperature conditions of the Earth's lower mantle (from 24 to 80 GPa). Earth's lower mantle was modelled as a geochemically "not-primitive" object because of an enrichment by 3 wt% of recycled crustal material (MORB-component). The chemical composition of the "*non primitive*" lower mantle takes into account both chondrite and pyrolite reference models to represent the lower mantle's primitive composition.

The capacity of perovskite to host Al was modelled through an Al_2O_3 exchange process in an unconstrained Mg-perovskite+Mg-Al-perovskite+free-Al_2O_3(corundum) system. Aluminium is *globally* incorporated principally *via* an increase in the amount of Al-bearing perovskite [*Mg-Al-pv*(80 GPa)/*Mg-Al-pv*(24 GPa)≈1.17], rather than by an increase in the Al_2O_3-content of the average chemical composition which changes little (0.11-0.13, mole fraction of Al_2O_3) and tends to decrease in Al. The Al_2O_3 distribution in the lower mantle was described through the probability of the occurrence of given compositions of Al-bearing perovskite. The probability of finding Mg-Al-perovskite is comparable to Al-free Mg-perovskite's. Perovskite with Al_2O_3 mole fraction up to 0.15 has an occurrence probability of ~28% at 24 GPa, increasing up to ~43% at 80 GPa; on the contrary, perovskite compositions in the range 0.19-0.30 Al_2O_3 mole fraction drop their occurrence probability from 9.8 to 2.0%, over the same *P*-range. In light of this, the distribution of Al in the lower mantle shows that, among the possible Al-bearing perovskite phases, the $(Mg_{0.89}Al_{0.11})(Si_{0.89}Al_{0.11})O_3$ composition is the likeliest, providing from 5 to 8% of the bulk perovskite in the pressure range from 24 to 80 GPa. The occurrence of the Al-richest composition, *i.e.* $(Mg_{0.71}Al_{0.29})(Si_{0.71}Al_{0.29})O_3$, is a rare event (probability of occurrence < 1.7%). This study predicts that perovskite may *globally* host Al_2O_3 in terms of 4.3 and 4.8 wt% (with respect to the non-primitive lower mantle mass),

thus accounting for ~ 90% and 100% of the bulk Al_2O_3 estimated in the framework of pyrolite and chondrite reference models, respectively. A calcium-ferrite-type phase (on the $MgAl_2O_4$-$NaAlSiO_4$ join) seems to be the only candidate that can compensate for the 10% gap of the perovskite Al-incorporation capacity, in the case of a pyrolite non-primitive lower mantle model.

1. INTRODUCTION

The mantle is the Earth's largest division by volume, originally marked by a planetary Siderophile/Lithophile element fractionation. Refractory Lithophile Elements (RLE) condensed from a gas of solar nebula composition at the highest temperature (>1400 K at 10^{-4} atm) compatible with the nebula's physical constraints (Lodders, 2003). RLEs' chemical behaviour prevented metal and sulphide phases from entering both chondrites and metallic cores during the planetary differentiation (Lodders, 2003; Kaminski and Javoy, 2013; Mahan et al., 2018). RLEs include Ca and Al among the major elements, the full group of rare earth elements (REE), U and Th. The chemical characteristics of such elements support the primitive Earth's mantle model that preserves the solar ratios of RLEs (Wasson and Kallemeyn, 1988; Lodders et al.,2009; Wang and Jacobsen, 2016).

Aluminium is the sixth most abundant element on Earth: it is a purely refractory lithophile element and its natural abundance is provided by the stable isotope ^{27}Al. The radioactive isotope ^{26}Al quickly decayed in ^{26}Mg (^{26}Al half-life = $7.17 \pm 0.24 \times 10^5$ yr; Norris et al., 1983, Wu and Browne, 1997) during the early stage of the solar system's evolution (Lee et al., 1977; Lodders, 2003; Baker et al., 2012). The ^{26}Al decay provided substantial heating to the proto planetary bodies, and its isotopic daughter is one of the most widely used extinct radioactivity chronometers (Bizzarro, et al., 2005; Spivak-Birndorf et al. 2009; Wimpenny et al., 2019).

Taking into account the geochemical behaviour of aluminium, it is unlikely that a large amount of such element may enter the Earth's core, though it provides a major constituent of many minerals at any depth of the Earth's mantle and crust. Aluminium is also one of the main components of any melt generated from the upper mantle, in terms of 9-21 wt% Al_2O_3 on average (source: PetDB Petrological Database). Melt crystallization, segregation, rise and cooling, led to the formation of the crust over the Earth's history. An intriguing aspect is that

74 Al, as a crustal component, partially, or entirely, was transported into the mantle, through
75 subduction. Such a process could involve mantle portions well below the magma source
76 regions (Young et al., 2005; Tsuchiya and Tsuchiya, 2008; Wang and Jacobsen, 2016).
77 Seismic tomography reveals that near the Earth's mantle transition zone, which marks the
78 boundary between upper and lower mantle, repositories of crustal material occur (Christensen
79 and Yuen, 1984; Billen, 2010, King et al., 2015). They exhibit different dynamic behaviours:
80 i) stagnation in the mantle transition zone (Japan trench; Honda, 2017 and references therein);
81 ii) stagnation in the uppermost lower mantle (Peruvian Andes; Fukao and Obayashi 2013); iii)
82 continuous descent, seemingly unhindered, into the lower mantle (Farallon plate, North
83 America; Sigloch et al., 2008). Such tomographic observations suggest a mechanism of global
84 mantle convection with an abundant mass exchange between distinct geochemical reservoirs
85 lying in both the upper and lower mantle (van der Hilst et al., 1997; Nolet et al., 2007).
86 More recently, geochemical models, aimed at explaining the isotopic evolution of the silicate
87 Earth (Kumari et al., 2016; Jones et al., 2019) or at tracing the distribution of key components
88 (H_2O and Fe-Mg) in the lower mantle (Walter et al., 2015; Merli et al., 2016; 2017), have
89 depicted the Earth's mantle as a chemical reservoir ("pyrolite") involving uninterrupted
90 geochemical reactions and energy/matter flows.
91 In particular, Kumari et al. (2016) estimated that about 60% of the entire mantle is as depleted
92 in fusible elements (*i.e.* Al and Ca) as its upper portion, whereas the remaining mantle is non-
93 primitive, containing a small fraction of transient and isolated recycled crustal materials.
94 Jones et al. (2019), combining the geodynamic model of mantle convection with isotope and
95 trace element geochemistry, suggest that the subduction and accumulation of dense oceanic
96 crust produce in the deep mantle a large mass of material enriched in incompatible trace
97 elements. The quoted authors also state that an equivalent of 50-70% of the current
98 continental crust mass was accumulated earlier than 3 Ga ago, and that the crustal recycling
99 and reworking dominated over juvenile additions to the continental crust, since the end of the

Archean (2.5 Ga). This suggests that since the end of the Hadean age (~ 4.6-3.8 Ga) the Earth's lower mantle has been enriched with crustal components.

Understanding the structure and chemical-physical behavior of the slabs subducted into the mantle is out of the scope of the present work. Conversely, we focus on the chemical rearrangement of the main lower mantle mineral phases in the case of a full mixing between crustal slabs and primordial lower mantle. In such a view, aluminium may be an effective "*probe*" among the major elements.

The present work deals with the modelling of Al-incorporation in perovskite, the major phase in the lower mantle, and the resulting Al-distribution, by means of quantum mechanics calculations in combination with equilibrium/off-equilibrium thermodynamics and cluster expansion technique. The cluster expansion approach allows the investigation of large atom clusters, thus providing an effective tool to model solid mixing in a statistical framework (see Merli et al. 2015, and references therein). Because of the complexity of the natural processes, it is convenient to start from a "reference" mineral phase, *i.e.* $MgSiO_3$-perovskite, whose Al-enrichment is investigated. We explore the *P*-range from 24 to 80 GPa, to unquestionably leave the perovskite-to-post perovskite transition aside (Murakami et al., 2004; Tsuchiya and Tsuchiya, 2008; Shim et al., 2008).

Our main goal is to estimate the maximum intrinsic capacity of perovskite to incorporate aluminium and its phase proportion with respect to the Al-free perovskite fraction, as a function of *P*-*T*. Subsequently, the resulting Al-partitioning will be used to discuss the global mechanism of storage of aluminium in the lower mantle.

2. GEOCHEMISTRY

2.1 Lower mantle geochemical model

Cosmochemical arguments supporting a chondritic bulk Earth composition (chondrite reference model) imply that the lower mantle must be enriched in Si with respect to a primitive upper mantle (PUM; Javoy et al., 2010; Murakami et al., 2012; Kaminski, and Javoy 2013), save that the Earth's core should be able to host ~4-6 wt% Si (McDonough 2014, Badro et al., 2014) to balance the Earth's Si-budget against the Sun's and chondrite's [$Mg/Si_{(PUM)}$~1.21-1.31 *versus* $Mg/Si_{(lower\ mantle)}$~1.01]. Conversely, according to petrological data and chondritic constraints the lower mantle is chemically equivalent to the primitive upper mantle (pyrolite reference model; McDonough and Sun,1995; Lyubetskaya and Korenaga, 2007).

Tomographic images of subducted slabs plunging into the deep mantle have been interpreted in terms of an efficient mass transfer between upper and lower mantle domains. This supports large scale mixing and therefore a homogenous Mg/Si distribution (*i.e.* pyrolite) throughout the mantle (Sigloch et al., 2008; van der Hilst et al., 1997). However, only a limited number of slabs actually sink into the lower mantle, given that most of the subducted ones flatten and seem to stagnate at either ~660 km or ~1,000 km depth (Fukao and Obayashi 2013). This points towards a comparatively ineffective mixing process and contrasts the notion of a vigorous global mantle convection. Recently, Ballmer et al. (2017) have hypothesised the presence of stable large-scale high-viscosity bridgmanite-enriched ancient mantle structures (BEAMS) that have been residing in the Earth's lower mantle since the early stage of our planet's formation. Their numerical model also predicts the incorporation of limited amounts of crustal material from shallow to deep mantle, particularly during the early stages. Such crustal portions provide stretched and stirred long-lived "fossil" fragments, in keeping with tomographic observations. Therefore, large-scale heterogeneities may account for the Earth's bulk composition, bringing the lower mantle's Mg/Si ratio closer to the solar-chondritic one unlike the upper mantle.

151 Hereafter, we shall refer to either the "pyrolite model" (based on the pyrolite composition
152 throughout the mantle) or the "chondrite model" (relying on different compositions between
153 upper and lower mantle) to describe the lower mantle.
154 Whatever bulk composition model is used to interpret the mantle's dynamics, the crustal
155 components plunging into the lower mantle cause large/small-scale changes of its phase
156 composition (Irifune et al. 1996; McDonough, 2016; Nestola et al., 2018).
157
158 2.2 **Enriched (*non-primitive*) lower mantle bulk composition**
159
160 Both chondrite and pyrolite lower mantle models are used here to estimate the non-primitive
161 lower mantle compositions. The bulk chemical composition of the lower mantle is generally
162 described in terms of its five major oxides (MgO, FeO, CaO, Al_2O_3 and SiO_2), which account
163 for ~98.5 wt% of the Earth's mantle mass (Mc Donough, 2016; Palme and O'Neill, 2014).
164 Na_2O occurrence, even if of modest impact on the large-scale geophysical and geochemical
165 modelling (Bina and Helffrich, 2014; Palme and O'Neill, 2014 Chust et al., 2017), is still
166 important in terms of the resulting minor mineral phases that affect the Al distribution in the
167 lower mantle. Experiments and observations on natural samples reveal that potential Al-
168 bearing lower mantle phases may also include K, Fe^{3+} and OH as major elements (*i.e.*: Kato et
169 al., 2013; Wang et al., 2015; Pamato et al., 2015; Harte and Richardson, 2012). In particular,
170 Al-bearing phases are able to host potassium if they form in a system containing at least ~
171 0.09 wt% K_2O (Kato et al., 2013). Note that the mid-ocean-ridge basalt (MORB) average
172 composition has 0.08-0.12 wt% K_2O (Gale et al., 2013), whereas pyrolite and chondrite lower
173 mantle models are estimated to bear ~0.03 and <0.01 wt% K_2O, respectively (McDonough
174 and Sun, 1995; Javoy et al., 2010). Therefore, K-bearing phases are not expected to play a
175 relevant role as potential aluminium hosts among the lower mantle phases. Although ferric
176 iron is able to affect Al^{3+} storage in perovskite-like structures *via* $Fe^{3+}\leftrightarrow Al^{3+}$ replacement

(Kurnosov et al., 2017), the $Fe^{3+}/\sum Fe_{tot}$ ratio in the primitive Earth's mantle is supposed to be very small, *i.e.* ~0.03, according to mass balance calculations (Palme and O'Neill, 2014). Bulk H_2O (hosted as OH-group) in the lower mantle influences the aluminium content incorporated by perovskite through the formation of Al-bearing hydrous phases. However, the bulk H_2O content is comparatively modest and estimated ~1500 ppm, in both pyrolite and chondrite lower mantle models (Merli et al., 2016; Muir and Brodholt, 2018).

Let us consider the lower mantle as a geochemically non-primitive object because it is mixed with a fraction of recycled crustal material (*i.e.* MORB-component). In this view, Al_2O_3 and CaO, hosted in lower mantle minerals, are potential "*probes*" which mark the occurrence of such a geodynamic process (Guignot and Andrault, 2004, Hirose et al., 2005; Korenaga, 2009; Irifune et al., 2010; Ricolleau et al., 2010).

The MORB chemical composition is enriched in incompatible major elements (aluminium, calcium and, to a lesser extent, iron) and depleted of compatible elements (magnesium) with respect to the mantle (Table 1). Therefore, a MORB-like composition at lower mantle *P-T* conditions cannot give Fe-periclase, whereas high-pressure SiO_2-rich phases (*e.g.* Ca-perovskite and bridgmanite) and additional aluminium-rich phases are expected to occur. Following experimental results about MORB bulk compositions (14-16 wt% Al_2O_3) under lower mantle conditions (30-90 GPa), the newly formed Al_2O_3-rich phases (NAL-type phase and $CaFe_2O_4$-type phase, *i.e.* CF-phase, on the join $MgAl_2O_4$-$NaAlSiO_4$) may account for about 10-12 mol% by phase composition (Guignot and Andrault, 2004, Ricolleau et al., 2010).

Assuming that subducted crustal fragments have been sliding down into the mantle over the past 4 billion years (the most generous estimate is about 11 wt% of the whole mantle; Li and McNamara, 2013), aluminium-rich domains should have developed, in contrast to expectations from a primitive lower mantle's composition (Stixrude and Lithgow-Bertelloni, 2012).

We model such an enrichment using the simple binary mixing equation of Faure (1986) to combine primitive lower mantle compositions (pyrolite and chondrite, corresponding to the end-members "A" and "A1", respectively; see Table 1) with a crust-type-composition (end-member "B"; MORB-like silicate glass; see Table 1). End-member B is close to the N-MORB average of Gale et al. (2013) and has been largely used in H*P* experiments (*i.e.* Hirose et al., 1999; 2005 Funamori et al., 2000; Guignot and Andrault, 2004; Ricolleau et al., 2010). According to the extensive compilation provided by the PetDB-database of chemical data from mid-ocean ridge basalts, the water concentrations lie in the range 0.05-1.0 wt%. The amount of H_2O stored in the deep mantle, computed by experiments and mass balance models (Ghosh et al., 2014; Marty, 2012), is in the range 800-2700 ppm (*i.e.* 0.08-0.27 wt%). Taking into account such figures and the tomographic observations that suggest that only small fractions of descending slabs reach the lower mantle (Ballmer et al. 2017), we model a non-primitive lower mantle composition by a chemical mixing of primitive pyrolite/chondrite compositions with a 3 wt% end-member B's contribution (0.1 wt% of H_2O). The resulting compositions are reported in Table 1. Such chemical mixing ideally reproduces a non-primitive lower mantle as predicted by modelling the isotopic evolution of the silicate Earth: ~3 wt% of the total mantle mass is expected to be stored and ultimately mixed within ~1 Ga in the lower mantle (Christensen and Hofmann 1994; Kumari et al., 2016; White, 2015).

3. METHODS

3.1 Chemical probability of formation: aluminium-bearing phases in the lower mantle

The probability that a phase "J" forms at *P-T*, *i.e.* $p(J|P,T)$, can be roughly estimated in terms of $p(J|P,T) \propto p(J,chem) \times \exp(-\Delta G(P,T)_{formation}/RT)$, where $p(J,chem)$ is the probability of having the required chemical species for J under the constraint of a given available elemental budget

and $\Delta G(P,T)_{\text{formation}}$ is the formation Gibbs energy. p(J,chem) is termed "*chemical probability of formation*", to underline that it reflects the likelihood of having the required elements to form the J-phase, and it is calculated as follows.

Let us assume X_k to represent the fractional abundance value of the k^{th}-oxide, in a generic system. Given that

$$\sum_{k=1,\mathrm{M}} X_k = 1 \qquad (1)$$

then X_k can also be associated with the *probability* of having the k^{th}-oxide, if the oxides are supposed to be uniformly distributed as a function of space. The chemical composition of the J-phase is then expressed formally as

$$\mathrm{J} = \sum_k n_k X_k \qquad (2)$$

Therefore, the probability of finding one mole of the J-phase as a function of its pure chemical composition, p(J,chem), is provided by the joint events of i) having (n_1-moles of X_1)(n_2-moles of X_2)…. and ii) not having any species with stoichiometric coefficient equal to 0. This corresponds to the following joint probability:

$$p(\mathrm{J},\mathrm{chem}) \propto \prod_k p(k)^{n_k} \times (1 - \sum_m p(m)) \propto \prod_j X_j^{n_j} \times (1 - \sum_m X_m) \qquad (3)$$

where $p(k)$ and $p(m)$ are the probabilities of finding the k^{th} and m^{th} oxide, respectively; the subscript k is associated with the chemical species with stoichiometric coefficients other than zero, whereas m is related to those with stoichiometric coefficients equal to zero. The p(J,chem) values calculated in this way are then normalized so that their sum yields unity.

Table 2 reports major phases and potential Al-bearing phases that experiments, numerical modelling and exceptional observations on natural findings indicated as possible minerals in a non-primitive lower mantle (Table 1).

Preliminary calculations led us to rule out periclase as a host of aluminium, save that the Al-incorporation takes place with the contribution of H (Merli et al., 2016). In such a case, the amount of Al involved would be negligible, anyway. Panero et al. (2006) estimated regular solution parameters of 12 and 66 kJ/mol for perovskite and akimotoite, respectively. Taking

into account i) the significantly lower energy for Al-incorporation in perovskite than in akimotoite and ii) the restricted range of occurrence of the latter (Panero et al., 2006), we exclude akimotoite as a possible competitor to uptake Al in the *P-T* region under investigation (Stebbins et al., 2001; Li et al. 2008; Tschauner et al., 2018). Majorite garnet, which is the main host of aluminium in the mantle transition region in both pyrolite and basaltic compositions (Irifune and Ringwood, 1993; Litasov and Ohtani, 2007), is transformed into Mg-perovskite+Ca-perovskite at pressures corresponding to the uppermost lower mantle. Experiments show that aluminium is mostly incorporated by Mg-perovskite/bridgmanite in pyrolite or chondrite compositions under lower mantle *P-T* conditions (Irifune et al.,1996; Ricolleau t al., 2008), whereas separate aluminous phases form in basaltic compositions (Hirose et a.,1999; 2005) at the same *P-T* conditions.

In a non-primitive lower mantle, aluminium is partitioned between perovskite/bridgmanite and minor Al-bearing phases, such as:

i) alkali rich NAL-structure phases, like those on the join $NaMg_2Al_{4.8}Si_{1.15}O_{12}$-$KMg_2Al_{4.8}Si_{1.15}O_{12}$ (Gasparik et al., 2000; Kato et al., 2013; Wu et al., 2016). However, as stated above, K-bearing phases are unlikely to develop in the lower mantle because of the lack of a sufficient amount of potassium;

ii) CF-structure and NAL-structure polymorphs, on the join $MgAl_2O_4$-$NaAlSiO_4$ (Imada et al., 2011; 2012; Irifune et al., 1991). Note that the CF-structure was observed to stabilize at a higher pressure (~ >40 GPa) than the NAL-structure (~ 24-40 GPa) (Imada et al., 2011; Guignot and Andrault, 2004);

iii) possible hydrous solid solutions involving D-phase, H-phase and δ-AlOOH (Ghosh and Schmidt, 2014; Pamato et al., 2015; Walter et al., 2015; Fukuyama et al., 2017).

In the case of NAL- and CF-phases, we chose to calculate a *chemical probability of formation* p(J,chem) for a reference NAL/CF-mineral, that is $Na_{0.265}Fe_{0.245}Mg_{0.375}Ca_{0.035}Al_{1.1}Si_{0.715}O_4$. Such a composition is obtained from Guignot and Andrault (2004), by averaging those that

281 the authors labelled with "CF^{A}" and "CF^{B1}", neglecting Ti and normalizing to 4 oxygen atoms
282 and 3 cations.
283 Hereafter we shall use the following acronyms, for the sake of brevity: *Mg-pv*, "Mg-
284 perovskite", for perovskite tout court, *i.e.* MgSiO3; *Mg-Al-pv*, "Al-perovskite", for Al bearing
285 Mg-perovskite, *i.e.* $(Mg,Al)(Si,Al)O_3$; *Mg-Fe-pv*, "bridgmanite", for Fe-bearing Mg-
286 perovskite, *i.e.* $(Mg,Fe)SiO_3$; *Ca-pv*, "Ca-perovskite", for Ca-bearing perovskite, *i.e.*
287 $(Ca,Mg)SiO_3$; "perovskite", for any solid mixing, or end member, occurring in the lower
288 mantle and having perovskite-type structure; *Fe-pe*, "Fe-periclase", *i.e.* (Mg,Fe)O; *CF*, "CF-
289 phase", for a phase in the $MgAl_2O_4$-$NaAlSiO_4$ join.
290
291 **3.2 Aluminium incorporation mechanisms of perovskite**
292
293 To evaluate the aluminium distribution in a non-primitive lower mantle, we model the Al-
294 uptake capacity of perovskite, which is the lower mantle phase able to host aluminium to such
295 an extent as to provide a relevant storage by volume (Jeanloz and Knittle, 1989; Ricolleau et
296 al.,2009).
297 We introduce the notion of "maximum Al-uptake capacity" of perovskite. "Maximum Al-
298 uptake capacity"-conditions are set through a *virtual* competition between $MgSiO_3$ and Al_2O_3
299 (ideal *pure* alumina phase) to accommodate Al, at lower mantle *P-T* conditions and in a SiO_2-
300 MgO-Al_2O_3 system. Corundum (*cor*) is the least "prejudicial" phase as an Al-host, given that
301 it does not require any further chemical species but aluminium to form and is the Al_2O_3-
302 polymorph stable in the *P-T* range of interest (Merli and Pavese 2018).
303 The incorporation mechanism of a trivalent cation in perovskite is supposed to occur through
304 three main reactions (Navrotsky et al., 2003; Akber-Knutson et al., 2005 and references
305 therein):
306 (i) $Si^{4+} + Mg^{2+} = M^{3+} + M^{3+}$

(ii) $Si^{4+} = M^{3+} + 1/2\ V^{0}_{O}$

(iii) $Si^{4+} = M^{3+} + H^{+}$.

Reaction (i), which takes place *via* a charge-coupled-mechanism, is the likeliest one, as shown by energy calculations (Yamamoto et al., 2003; Akber-Knutson et al., 2005; Zhang and Oganov, 2006). A comparison between incorporation mechanisms (i) and (ii) reveals that the former is slightly exothermic, in contrast with the endothermic behaviour of the latter (Navrotsky et al., 2003). NMR-measurements point to the occurrence of a charge-coupled mechanism (Stebbins et al., 2001), in agreement with calculations of Akber-Knutson and Bukowinski (2004), who suggest that Al tends to replace both Si and M^{2+}, in a high pressure and high temperature regime. As to reaction (iii), we assume contents of H_2O, *i.e.* H^+ supplier, and Al_2O_3 as much as 1500 ppm (0.15 wt%) and 4.76 wt%, respectively (Table 1), in keeping with the lower mantle Al-richest composition obtained by mixing pyrolite with 3% MORB-component (Table 1). In such a case, even if all the hydrogen from the dissociation $OH_2 \rightarrow OH^- + H^+$ contributed to an exchange mechanism like (iii), just 0.08 mol fraction aluminium might be accounted for. Moreover, according to the H_2O-partitioning estimated by Merli et al. (2016), periclase is able to account for 1/3 of the trapped H_2O, thus reducing further the role of reaction (iii) as a possible relevant mechanism to Al-incorporation in perovskite.

Therefore, the Al-uptake in perovskite is modelled by the replacement of Mg-Si with Al-Al, according to the exchange reaction reported below using the formalism of Kröger-Vink (Kröger, 1972)

$$Al_2O_3 + [Mg_{Mg}]^X + [Si_{Si}]^X \leftrightarrow [Al_{Mg}]^{\bullet} + [Al_{Si}]' + MgSiO_3. \quad (4)$$

Assuming λ-mole of Al_2O_3 to be exchanged in the *Mg-Al-pv*, *Mg-pv* and *cor* system, then equ.(4) leads to

$$(1-\lambda)MgSiO_3 + \lambda\ Al_2O_3 \Leftrightarrow (Mg_{1-\lambda}Al_{\lambda})(Si_{1-\lambda}Al_{\lambda})O_3. \quad (5)$$

In reaction (5) iron can affect the energy through a replacement like $Mg^{2+} \Leftrightarrow Fe^{2+}$ and competes with aluminium in terms of $Al^{3+} \Leftrightarrow Fe^{3+}$. However, we chose to neglect Fe as we are developing a first approximation model, which would provide general trends rather than details. Our choice can be further supported by the following arguments.

- The general reaction that accounts for Al_2O_3 entering in bridgmanite turns out to be

$$(Mg_{1-x}Fe_x^{2+})SiO_3 + \lambda Al_2O_3 = \left(Mg_{1-x-\lambda/2}Fe_{x-\lambda/2}^{2+}Al_\lambda\right)(Si_{1-\lambda}Al_\lambda)O_3 + \lambda\,(Mg_{\frac{1}{2}}Fe_{\frac{1}{2}}^{2+})SiO_3 \quad (6)$$

where we assume that Al replaces the same quantity of Mg and Fe^{2+}, the latter dwelling at the 12-coordination site, only (Kaminsky and Lin, 2017). The parametrization of the Gibbs energy used in the present work relies upon the cluster expansion technique (Merli et al., 2015; 2017). Such a method leads to expressing energy as a function of the number of interacting atomic pairs that belong to the same cluster determined as a function of the distance between the involved chemical species. Assuming Fe-Al pair entering the perovskite structure as much as 0.1-0.2 moles (*i.e.* Kurnosov et al., 2017; Kaminsky and Lin, 2017), the probability of having a Fe-Al interacting pair belonging to the first/second cluster is ~5-6 %. Therefore, most of the interactions with aluminium atoms are due to the pure Mg-Si matrix, which governs the "maximum intrinsic capacity" of perovskite to incorporate Al.

The role of Fe^{3+} is extensively debated and still largely uncertain. *Mg-Fe-pv* is potentially the major Fe^{3+} acceptor, but Kaminsky and Lin (2017) indicated that in natural lower mantle bridgmanites iron most likely occurs as ferrous at the 12-coordination sites. Conversely, Kurnosov et al. (2017) claim $Fe^{3+}/\Sigma Fe_{tot} = 0.33$, in synthetic bridgmanite with ferric iron sited at the same coordination site, under lower mantle conditions (P~ 35 GPa; 1300 km depth; Ismailova et al. 2016). Mass balance calculations, in turn, predict an impact of ferric iron in terms of $Fe^{3+}/\sum Fe_{tot}$~0.03, with

respect to the Earth's mantle abundances (Palme and O'Neill, 2014). If we consider as a first level of approximation pyrolite (*Mg-Fe-pv* =76 wt%; FeO_{tot} = 8.05 wt%) and chondrite (*Mg-Fe-pv* =85 wt%; FeO_{tot} = 8.12 wt%) lower mantle models (Table 1), and apply the Kurnosov et al. (2017) Fe^{3+}/Fe_{tot} ratio to *Mg-Fe-pv*, the resulting Al^{3+}/Fe^{3+} mole ratios in bridgmanite are ~3.6 and ~2.9 for pyrolite and chondrite models, respectively. Tests based on calculations that we carried out to reproduce the replacement schemes Si + Mg ⇔ Al + Fe^{3+} *versus* Si + Mg ⇔ Al + Al, indicate that the second reaction is favoured over the former one [in agreement with the results of Nishio-Hamane et al. (2005)].

3.3 Reaction models

The Al-uptake mechanism in perovskite according to reaction (5) is addressed using two approaches: i) the *open system model*, which exploits the notion of stationary thermodynamic state and allows an exchange of matter between system and reservoir (Prigogine 1968); ii) the *closed system model*, which relies on equilibrium thermodynamics, therefore excluding any sort of matter exchange. In an open system, the stationary state replaces the equilibrium state and exhibits thermodynamic observables, which remain invariant over time. Details about the open system model are reported in APPENDIX I.1-.2-.3 and a brief overview is given below.

3.3.1 Open system model

We would like to exploit the capacity of an open system to exchange matter with a reservoir, in combination with a formalism as close as possible to the consolidated equilibrium thermodynamics' one. Such a model provides a flexible tool to address problems in which the intrinsic exchanging/incorporation capacity of a given substance can be investigated, without any sort of constraint or restraint (APPENDIX I.1).

The key requirement is the fulfilment of the following equation, associated to reaction (5) *via* the equilibrium constant K (APPENDIX I.2-3):

$$K(P,T,\lambda) = exp[-\Delta G_0(P,T,\lambda)/\mathrm{R}T] = a_{Mg-Al-pv}/\left(a_{Mg-pv}^{1-\lambda} \times a_{cor}^{\lambda}\right) \approx x_{Mg-Al-pv}/\left(x_{Mg-pv}^{1-\lambda} \times x_{cor}^{\lambda}\right) \quad (7.a)$$

where x_j=phase proportion of the jth-component/phase (*cor*: corundum); a_j=jth-component/phase's activity. In equ.(7.a) the activity coefficient is approximated to unity (see APPENDIX I.3 and APPENDIX II). Expanding ΔG_0, it follows that:

$$\Delta G_0(P,T,\lambda) = \mu_0(P,T,\lambda)_{Mg-Al-pv} - \lambda \times \left[\mu_0(P,T)_{cor} - \mu_0(P,T)_{Mg-pv}\right] - \mu_0(P,T)_{Mg-pv}. \quad (7.b)$$

where μ_0 is the part of the chemical potential depending on λ, P and T, only (Ottonello 1997; 2010). For convenience, we split the chemical potential of Al-incorporating perovskite (*Mg-Al-pv*) into an Al-free part, *i.e*. pure perovskite (*Mg-pv*), and a part dependent on aluminium, that is

$$\mu_0(P,T,\lambda)_{Mg-Al-pv} = \mu_0(P,T)_{Mg-pv} + \Delta\mu_0(P,T,\lambda)_{Mg-Al-pv}, \quad (7.c)$$

where $\Delta\mu_0(P,T,\lambda)_{Mg\text{-}Al\text{-}pv}$, which accounts for the solid mixing occurrence and provides the very core of our computational model, is calculated by the cluster expansion method (Merli et al 2015, 2017).

Using equ.(7.c), equ.(7.b) becomes

$$\Delta G_0(P,T,\lambda) = \Delta\mu_0(P,T,\lambda)_{Mg-Al-pv} - \lambda\left[\mu_0(P,T)_{cor} - \mu_0(P,T)_{Mg-pv}\right]. \quad (8)$$

At given (P,T,λ)-values, we seek the {$x_{Mg\text{-}Al\text{-}pv}$, $x_{Mg\text{-}pv}$, x_{cor}}-sets that fulfil

a) equ.(7.a),

b) $x_{Mg\text{-}Al\text{-}pv}$, $x_{Mg\text{-}pv}$, $x_{cor} \geq 0$,

c) $x_{Mg\text{-}Al\text{-}pv} + x_{Mg\text{-}pv} + x_{cor} = 1$.

Among the solutions that satisfy the constraints a), b) and c), we chose the one that minimizes the Gibbs energy, namely $x_{Mg\text{-}Al\text{-}pv} \times \mu_0(P,T,\lambda)_{Mg\text{-}Al\text{-}pv} + x_{Mg\text{-}pv} \times \mu_0(P,T)_{Mg\text{-}pv} + x_{cor} \times \mu_0(P,T)_{cor}$. In

doing so, we obtain a triple, yielding *Mg-Al-pv*/*Mg-pv*/*cor* phase proportions, for each (P,T,λ) point, *i.e.* $\{x_{Mg\text{-}Al\text{-}pv}, x_{Mg\text{-}pv}, x_{cor}\}(P,T,\lambda)$. The preservation of the total chemical composition of the system constituted by each $\{x_{Mg\text{-}Al\text{-}pv}, x_{Mg\text{-}pv}, x_{cor}\}(P,T,\lambda)$-triple is not required. The resulting system therefore behaves as an open system that can exchange 2Al ⇔ Mg+Si with a reservoir. In general, we are interested in modelling *observables* whose values are averages over the λ-range, so that they depend ultimately on *P*-*T* only. For instance:

$$\{x_{Mg-Al-pv}, x_{Mg-pv}, x_{cor}\}(P,T) = \frac{1}{C}\int_{\lambda-inf}^{\lambda-sup}\{x_{Mg-Al-pv}, x_{Mg-pv}, x_{cor}\}(P,T,\lambda)\,\mathrm{d}\lambda \qquad (9.\mathrm{a})$$

$$\lambda_{Al2O3}(P,T) = \int_{\lambda-inf}^{\lambda-sup}\lambda \times x_{Mg-Al-pv}(P,T,\lambda)\,\mathrm{d}\lambda / x_{Mg-Al-pv}(P,T) \qquad (9.\mathrm{b})$$

$$Tot_{Al2O3}(P,T) = \frac{1}{C}\int_{\lambda-inf}^{\lambda-sup}\left[\lambda \times x_{Mg-Al-pv}(P,T,\lambda) + x_{Al2O3}(P,T,\lambda)\right]\mathrm{d}\lambda \qquad (9.\mathrm{c})$$

where: C is a normalization constant; λ-sup=0.3 and λ-inf=0, upper and lower thresholds of λ, respectively (for λ>0.3, $x_{Mg\text{-}Al\text{-}pv}$ is negligible on the *P*-*T* range explored); λ_{Al2O3} of (9.b) is the *average* Al_2O_3 mole fraction *per* formula unit; Tot_{Al2O3} is the total Al_2O_3 stored by the (*Mg-Al-pv*)+(*Mg-pv*)+*cor* system.

3.3.2 Closed system model

For the sake of completeness, we also present the closed system model. We seek the equilibrium conditions of reaction (5) for a closed system, *i.e.* a chemically adiabatic one. Let ξ represent the aluminium occupancy factor in *Mg-Al-pv* [*i.e.* $(Mg_{1-\xi}Al_{\xi})(Si_{1-\xi}Al_{\xi})O_3$]. Therefore, we have to minimize, with respect to ξ, the Gibbs energy of the system (*Mg-pv*)+(*Mg-Al-pv*)+*cor*, *i.e.*

$$G = n_{cor} \times \mu_0(P,T)_{cor} + n_{pv} \times \mu_0(P,T)_{Mg-pv} + n_{Mg-Al-pv} \times \mu_0(P,T,\xi)_{Mg-Al-pv}, \qquad (10)$$

under the constraints of the conservation of mass:

$$M_{Al2O3} = n_{cor} + n_{Mg\text{-}Al\text{-}pv} \times \xi \qquad (11)$$

$$M = M_{SiO2} = M_{MgO} = n_{Mg\text{-}pv} + n_{Mg\text{-}Al\text{-}pv} \times (1-\xi), \qquad (12)$$

where M_{Al2O3}, M_{SiO2} and M_{MgO} are *fixed* total amounts in moles of Al_2O_3, SiO_2 and MgO.

Using the constraints above, equ.(10) becomes

$$G = \left(M_{Al2O3} - n_{Mg-Al-pv} \times \xi\right) \times \mu_0(P,T)_{cor} + \left(M - n_{Mg-Al-pv} \times (1-\xi)\right) \times \mu_0(P,T)_{Mg-pv} + n_{Mg-Al-pv} \times \mu_0(P,T,\xi)_{Mg-Al-pv}. \quad (13)$$

The Gibbs energy minimum condition requires

$$\frac{\partial G}{\partial \xi} = 0,$$

from which the following equation is derived

$$-\mu_0(P,T)_{cor} + \mu_0(P,T)_{Mg-pv} + \frac{\partial \mu_0(P,T,\xi)_{Mg-Al-pv}}{\partial \xi} = 0. \quad (14)$$

Equ.(14) formalises the equilibrium conditions for closed systems (Chust et al. 2017). Its solution, expressed by $\xi_{\text{closed system}}$, yields the composition of Al-bearing perovskite that minimises the Gibbs energy of equ.(13).

$\xi_{\text{closed system}}$ also minimises (7.b). In fact, taking into account equ.(7.c), equ.(14) is equivalent to setting $\frac{\partial \Delta G_0(P,T,\lambda)}{\partial \lambda} = 0$ in equ.(8), which implies that $K(P,T,\xi_{\text{closed system}})$ achieves an extreme value that shifts reaction (5) towards its right-hand side member as much as possible.

3.4 Computational

Structure relaxations were performed at a given pressure and 0 K by the HF/DFT-CRYSTAL14 program (Dovesi el al., 2009), which implements "A*b-initio* Linear-Combination-of-Atomic-Orbitals" for periodic systems. Only static pressure (P_{static}=-$\partial E_{\text{static energy}}/\partial V$) and zero-point pressure (P_{zp}==-$\partial E_{\text{vibration energy at 0K}}/\partial V$) were taken into account, given that even adding a correction for thermal contributions would not significantly change our results and the conclusions would be unaffected. A zero-point pressure was estimated by quantum mechanics calculations and using *pure perovskite* only, resulting in ~5 GPa. The

WCGGA functional (Wu and Cohen, 2006) was used, with a hybridization rate of 28%. Such a proportion was adopted because it provides a more satisfactory agreement with observations in terms of perovskite structure, than other choices do. The tolerances governing the accuracy of the integrals of the self-consistent-field-cycles were set at (in Ha units): 10^{-8} for coulomb overlap, 10^{-8} for coulomb penetration, 10^{-8} for exchange overlap, 10^{-8} for exchange pseudo-overlap in direct space, 10^{-16} for exchange pseudo-overlap in reciprocal space and 10^{-9} for threshold for SCF-cycles' convergence. The Mg basis set from Causà et al. (1986) was extended by the addition of diffuse *sp* and *d* shells (85-11G* contraction). Oxygen and aluminium were modelled by means of the O8-411d1 and 85-11G* basis sets of Corà (2005) and Catti et al. (1994), respectively. The outer shells' coefficients were optimised by means of the "billy" utility by Towler (2015). The eigenvalue level shifting technique was used (level shift of 0.2 Ha) to avoid conducting solutions and accelerate convergence.

The approach of Merli et al. (2015 and 2017) relying upon the cluster expansion technique was adopted to model the solid mixing in *Mg-Al-pv*. Such a method makes it possible to parametrize energy as a function of pair interactions, thus allowing one to model in a statistical framework even large atom clusters that would be difficult to handle otherwise. We expressed the Al-dependent part of the chemical potentials in equ.(7.b) as

$$\Delta\mu_0(P,T,\lambda)_{Mg-Al-pv} = \mu_0(P,T,\lambda)_{Mg-Al-pv} - \mu_0(P,T)_{pv} = \lambda \times [\mu_0(P,T,\lambda)_{Mg-Al-pv} - \mu_0(P,T)_{cor}] + \delta\mu_0(P,T,\lambda)_{Mg-Al-pv}. \quad (15)$$

$\delta\mu_0(P,T,\lambda)$, in turn, was developed in terms of

$$\delta\mu_0(P,T,\lambda)_{Mg-Al-pv} = (1-\lambda) \times \lambda \times \sum_{l=0,L;m=0,M;n=0,N} p_{lmn} P^l T^m \lambda^n. \quad (16)$$

We used perovskite's supercells, composed of (2×2×1), (2×1×2) and (1×2×2) elementary cells. A total of 80 independent Al-configurations were randomly sampled over the interval 24-80 GPa and used to calculate the pair-interaction parameters of the cluster expansion as a function of *P*, following the strategy of Merli et al. (2017). We then simulated 10^5-10^6 *Mg-Al-*

pv independent configurations in 1024 atom clusters, using the pair-interaction parameters previously determined, to carry out statistical thermodynamics calculations (Merli et al. 2015), and model the Gibbs energy of Al-bearing perovskite thereby.

ΔG_0 in equ.(7.b) were calculated neglecting the atomic vibration contribution, *i.e.* the one including zero-point vibration energy, thermal vibration energy and vibration entropy (in full: $\Delta G_{0,vib}$). In general, calculating $\Delta G_{0,vib}$ in a solid mixing that is modelled *via* a super-cell method is a difficult task, because of the complexity of compromising between representativeness of a cluster, computing time and achievable precision (about the role of vibrational components, see: van de Walle and Ceder, 2002). However, combining quantum calculations with semi-empirical potentials (GULP code; Gale 1997; 2005), which allow the investigation of large atomic clusters' lattice dynamics, we estimated, by harmonic approximation, $\Delta G_{0,vib}$ for 4 Al-Al configurations in perovskite at 20 and 70 GPa, with 0.25 Al_2O_3 mole fraction. In this way we compared $\Delta G_{0,vib}$ with $\Delta G_{0,stat+conf}$, *i.e.* the static contribution with the addition of configuration entropy, which we actually calculated. We observed $|\Delta G_{0,vib}/\Delta G_{0,stat+conf}|$~3%, in the thermal range of interest, *i.e.* 2000-3000 K. Therefore, taking into account the modest estimated weight of the thermal contribution in the solid mixing, we chose to leave it aside (as for neglecting vibration contribution, see for instance: Mohn and Trønnes 2016; Burton and van de Walle, 2003).

4. RESULTS

4.1 Chemical probability of formation of lower mantle phases

The bulk aluminium content (largest value: 4.76 wt%, related to pyrolite lower mantle mixed with 3% of crustal component; Table 1) and the available amounts of alkali elements and H_2O make the *chemical probability of formation* [*p*(J,chem)] for the minor Al-bearing phases <

505 0.9% with respect to the total phases formed under the constraint of a non-primitive lower
506 mantle composition (Table 1; Table 2). As expected, the *p*(J,chem) of *Mg-Fe-pv+Mg-pv+Ca-*
507 *pv+Fe-pe* in a non-primitive lower mantle is >78%, regardless of the geochemical model
508 used. It is worth noting that *p*(J,chem) of *Mg-Al-pv* is as large as ~96%, considering the Al-
509 bearing phases only (Table 3). The hydrous phases are *quasi* irrelevant, whereas the NAL/CF-
510 type phase exhibits a *p*(J,chem) as large as 3.87-3.57% (Table 3).
511 If we used *p*(J,chem) as an "actual" *probability of finding a given phase*, then Al would
512 distribute in terms of 4/5 *versus* 1/5 between *Mg-Al-pv* and *CF* (the CF-phase is able to host
513 almost six times as much aluminium as perovskite). This estimate is to be taken with due care
514 as *p*(*Mg-Al-pv*,chem) and *p*(*CF*,chem) quantify only the probability of having the "least
515 condition" for a given phase to form, regardless of the energy contribution and inter-phase
516 competition to capture the involved elements. Altogether, perovskite is the main candidate to
517 incorporate aluminium by far, though *CF*, too, exhibits a potential capacity for Al-storing.
518
519 **4.2 Al-uptake in perovskite: open system model *versus* closed system model**
520
521 The main advantages of using an *open system model* with respect to a *closed system model* are
522 the following:
523 -neglecting the chemical composition invariance allows the system to evolve *unconstrained*,
524 driven by the mixing Gibbs energy of the solid solution of *Mg-Al-pv*. This provides the most
525 favourable condition to estimate the *Mg-Al-pv*'s intrinsic maximum capacity to host Al,
526 resorting to a simple system composed of perovskite in combination with free-alumina (*cor*),
527 the latter accounting for the aluminium not incorporated by the former because of saturation;
528 -such a method makes it possible i) to achieve an average depiction of the output of a given
529 chemical process and ii) to explore a mechanism of Al-storage taking into account not only

the Al-occupancy in perovskite, but also the amount of perovskite that is able to host aluminium *versus* the fraction of Al-free perovskite (*Mg-Al-pv*/*Mg-pv*).

Reaction (5) was investigated using the *P*-*T* curve parametrised by Merli et al. (2016) as follows

T(K) = 11.290 × P (GPa) +1648,

for 24< P < 80 (GPa). Such a curve represents a lower mantle in a whole mantle convention of limited thermal efficiency (Mattern et al., 2005; Stixrude and Lithgrow-Bertelloni, 2005), thus approaching the layered mantle convection models (Brown and Shankland, 1981; Anderson, 1982 ; Valencia-Cardona et al., 2017).

4.2.1 Al-uptake in perovskite from open system model

Figure 1 shows $K(P,T,\lambda)$ of equ. (7.a) as a function of λ, at three chosen *P*-*T* points. In general, the larger the value of *K*, the more reaction (5) shifts to the right, *i.e*. towards *Mg-Al-pv*. For each *P*-*T* point, $K(P,T,\lambda)$ has a maximum that changes from about 0.17 (24 GPa/1919 K) to 0.26 (80 GPa/2551 K). This means that there is an Al-exchange λ-value that maximises the tendency to promote *Mg-Al-pv* at each *P*-*T* point of the geotherm. We now introduce the function $K(P,T)_{ave}$, which corresponds to the average of the equilibrium constant of reaction (5), *i.e*. $K(P,T)_{ave}=<K(P,T,\lambda)>_{\lambda}$. $K(P,T)_{ave}$ provides an overview of the general tendency of the aluminium incorporation process to shift either to the right or left in reaction (5) along the chosen *P*-*T* path (Fig. 2). $K(P,T)_{ave}$ calculated over Al-exchange processes between corundum and perovskite from 0 to 0.3 λ-value, tends to increase upon increasing *P*, *i.e*. reaction (5) shifts more and more to its right-hand side member $[(Mg_{1-\lambda}Al_{\lambda})(Si_{1-\lambda}Al_{\lambda})O_3]$. Two trends of $K(P,T)_{ave}$ are observable: one below and one above ~60 GPa, characterised by 0.008 and 0.02 GPa^{-1} slopes, respectively (Fig. 2). They are reflective of the growing differences between the $K(P,T,\lambda)$-curves, for λ > 0.15 (Fig. 1). On the explored *P*-*T* interval, the content of free-Al_2O_3,

555 *i.e. cor*, takes a very small average figure of 0.0010(±1), in terms of phase proportion.
556 Conversely, Al-free (*Mg-pv*) and Al-bearing (*Mg-Al-pv)* perovskite phases amount to
557 0.56(±2) and 0.44(±2), respectively (Fig. 3). *Mg-Al-pv* increases from 0.41 to 0.48 phase
558 proportion, from 24 to 80 GPa: this hints at a tendency to develop more and more
559 (Mg,Al)(Si,Al)O_3-phase upon *P* (Fig. 3).
560 The *cor/Mg-Al-pv* ratio monotonically decreases with increasing pressure up to 70 GPa (Fig.
561 4), from more than 0.022 to about 0.017, meaning that some 98 wt% of available Al_2O_3 is
562 taken by perovskite, in agreement with the results shown in Figures 1-3. In the range 60-80
563 GPa the data are rather scattered and weakly *P*-dependent. They indicate either some sort of
564 "saturation" (with respect to perovskite) or a poorly defined minimum. The aluminium uptake
565 capacity of perovskite is described *via* λ_{Al2O3}, see equ.(9.b), that gives the average Al_2O_3 mole
566 fraction *per* formula unit (Fig. 5). At 32 GPa perovskite hosts Al_2O_3 at its maximum capacity
567 (λ_{Al2O3}= 0.134 Al_2O_3 mole fraction) and preserves such an occupancy figure up to ~50 GPa
568 (Fig. 5). The occupancy starts to monotonically decrease beyond 50 GPa, with a slope of
569 about -0.0009 GPa^{-1} (λ_{Al2O3} = 0.105 Al_2O_3 mole fraction, at 80 GPa; Fig. 5). This takes place
570 in combination with an increase of the phase fraction of Al-bearing perovskite.
571
572 *4.2.2 Al-uptake in perovskite from a closed system model*
573 The Al-occupancy factor $\xi_{closed\ system}$, as reported in equations (10)-(11) and (12), minimises
574 the Gibbs energy and maximises the equilibrium constant of equ.(7.a), *i.e.* if $\lambda=\xi_{closed\ system}$
575 then $K(P,T,\lambda)$ takes its maximum value. $\xi_{closed\ system}$ exhibits a linear and increasing trend,
576 trailing down the mantle (Fig. 6). This implies that the perovskite structure incorporates more
577 and more aluminium as the pressure increases, if the system is *chemically adiabatic* and *cor*
578 only competes to host Al. Such a result can be seen in terms of that if a given amount of Al
579 must be "*perforce*" accommodated over perovskite and *cor*, then aluminium chooses

progressively the former with respect to the latter with increasing *P*, thus yielding a shift of reaction (5) to the right.

4.3 Solid mixing model performances with respect to some experimental data

We tested the physical soundness of our mixing energy model comparing its predictions with some experimental results related to *Mg-Al-pv* properties.

The enthalpy formation of the reaction 0.05 Al_2O_3 (*cor*) + 0.95 $MgSiO_3$ = $Mg_{0.9}Si_{0.9}Al_{0.1}O_3$ was measured to be as large as -0.8(±2.2) kJ/mol by Navrotsky et al. (2003). Such a figure is to be compared with -1.1 kJ/mol from our calculations. Although our estimation is 40% larger than the experimental value, the exothermic nature of the reaction is correctly predicted and, taking into account the uncertainty of measurements, observation and theoretical estimate are in good agreement. In Figure 7, we report the absolute values of the discrepancy between measurements (Walter et al., 2004) and our predictions on the Al-bearing perovskite cell volume. In most cases, the deviation lies below 0.8%, and just for three experimental points we observe a discrepancy above 1%. Altogether, the average disagreement is about 0.4% and indicates a chemical-physical soundness of the solid mixing model we are using.

5. DISCUSSION

5.1 Aluminium storage mechanism

Our results from the open system model point to a complex mechanism of Al-uptake in perovskite as a function of pressure (Figs.3-5). In particular, the aluminium storage involves both the *Mg-Al-pv* phase proportion and the average Al_2O_3-mole fraction incorporated by *Mg-Al-pv* (*i.e.* λ_{Al2O3}; see equ.(9.b)). Whereas λ_{Al2O3} (Fig. 5) changes comparably little and, in

606 general, moderately decreases at large pressures, the phase fraction of *Mg-Al-pv* grows by
607 ~16% upon increasing *P* (Fig. 3).
608 We underline that our model relies on mass transfer reactions within a chemically
609 unconstrained open system constituted by *Mg-pv+Mg-Al-pv+cor* that act as Al-Mg-Si
610 exchangers with an ideal reservoir; therefore, the calculated maximum Al-uptake capacity in
611 perovskite is independent of the geochemical frame.
612 A lower mantle composition with chondritic Mg/Si ratio of ~1.01 implies an amount of
613 perovskite from 83 up to 90 wt%, juxtaposed to the pyrolitic composition that predicts
614 perovskite in the narrow range of 75-78 wt% (Lyubetskaya and Korenaga, 2007, McDonough,
615 2016). The relative proportion of this phase in a lower mantle mixed with 3% of MORB-like
616 component does not significantly vary with respect to the reference models (Table 1). This is
617 consistent with the fact that the total *chemical probability of formation*, *p*(J,chem), of the Mg-
618 rich perovskite-type phases (*i.e. Mg-pv+Mg-Fe-pv+Mg-Al-pv*) does not significantly change
619 between the primitive (A and A1) and non-primitive (A+3%B and A1+3%B) lower mantle
620 models (Table 2).
621 The predicted *total* Al_2O_3 that *Mg-Al-pv* may accommodate is shown in Figure 8, along with
622 the *bulk* Al-content inferred for primitive and enriched lower mantle compositions. We point
623 out two aspects:
624 (i) the average *total* Al_2O_3 that perovskite (76 and 85 wt% in pyrolite and chondrite reference
625 models, respectively) hosts is 4.28 and 4.78 wt% of the lower mantle mass. Such figures
626 prove that perovskite is able to accommodate *almost* the entire budget of Al_2O_3 estimated for
627 non-primitive lower mantle compositions. Perovskite exhibits an average Al-hosting capacity
628 of ~90%, in the case of pyrolite model (Al_2O_3: 4.76 wt%), and > 100%, in the case of
629 chondrite model (Al_2O_3: 4.31wt%). See also Table 1 and Figure 8;
630 (ii) the *total* Al_2O_3 stored by *Mg-Al-pv* as a function of *P-T* (Fig. 8) varies in a comparatively
631 narrow range from 24 to about 60 GPa (~4.18-4.24 wt% and ~4.67-4.75 wt%, for pyrolite and

chondrite models, respectively), while it decreases going down the mantle (3.99 and 4.47 wt%, for pyrolite and chondrite models, respectively), at 80 GPa. This may be related to the occurrence of the already mentioned change of trend exhibited by the average equilibrium constant (Fig. 2). The decrease of the λ_{Al2O3}-values (Fig. 5) and the "saturation" of the Al_2O_3-partitioning between perovskite and *cor* (Fig. 4) point to: i) a progressive reduction in the Al-storage capacity of *Mg-Al-pv*; ii) a change of the *cor*/*Mg-Al-pv* trend that might reflect the onset of instability in perovskite, probably leading to the formation of other aluminium hosting phases (*i.e*. structural change to post-perovskite; Murakami et al., 2004; Shim et al., 2008; Tsuchiya and Tsuchiya, 2008; Tateno et al., 2009). We believe that it is physically incongruous that at *P*~ 60-80 GPa the *cor*/perovskite molar ratio inverts its decreasing trend, as this suggests that *Mg-Al-pv* loses competitiveness with respect to *cor* in hosting aluminium upon increasing *P*. In fact: i) *cor* undergoes a phase transition to the rhodium-oxide-like phase in the range of ~80-100 GPa (Thomson et al., 1996; Funamori and Jeanloz, 1997; Merli and Pavese, 2018); ii) the Al-content in perovskite monotonically decreases with pressure (60-80 GPa; Fig.5), thus implying a reduction of the strain, which is due to the occurrence of species other than Mg-Si. Such a reduction of the strain is expected to promote the stability of a perovskite-like structure.

Altogether, it can be observed that:

i) aluminium is *globally* incorporated foremost *via* an increase of the Al-bearing perovskite amount, rather than by an increase of the Al_2O_3-content in *Mg-Al-pv* chemical composition;

ii) the perovskite phase is able to accommodate an Al-excess consistent with 3 wt% MORB-component mixed with primitive lower mantle compositions, up to 100% and 90% of the Al_2O_3-budget, in the case of chondrite and pyrolite models, respectively.

At higher pressure than those investigated here, the transformations of corundum to a more stable structure (~80-100 GPa) as above-mentioned and of perovskite to the $CaIrO_3$-like phase (often called post-perovskite) at ~120 GPa (Murakami et al., 2004) might account for the

change of the trend related to the Al-storage capacity of perovskite (Fig. 4). In fact, calculated phase equilibria in the $MgSiO_3$-Al_2O_3 system, modelled at *P-T* conditions relevant for the Earth's deepest mantle (80-140 GPa/2000-4000 K), predict the appearance of (Al-bearing)-post-perovskite coexisting with Mg-perovskite between 90 and 105 GPa, at *T* =2000 and 3000 K, respectively (Tsuchiya and Tsuchiya, 2008). According to the phase diagrams of these authors, the perovskite structure can accommodate up to ~0.19 moles of Al_2O_3 at 80 GPa and 2000 K, whereas at 3000 K the solubility of alumina increases up to ~0.4 moles. Interpolation yields ~0.3 moles of Al_2O_3 at 80 GPa and 2550 K. Such results can be compared with ours achieved by the closed system model, which relies on the same equilibrium thermodynamics approach. It is worth noting that the closed system model yields the Al_2O_3-composition of *Mg-Al-pv* that mostly shifts reaction (5) to the right, *i.e.* $K(P,T,\xi_{closed\ system})$ has a maximum. $\xi_{closed\ system}$ in turn, has an increasing trend trailing down the lower mantle (Figs. 1 and 6), providing an Al_2O_3-content of ~0.26 moles at *P*=80 GPa, in agreement with Tsuchiya and Tsuchiya (2008).

5.2 Composition of *Mg-Al-pv* in the lower mantle

There is a controversy on whether the negative buoyancy associated with subducted oceanic crust can overcome the viscous forces in the dynamic regions of Core-Mantle-Boundary (CMB) and accumulate into large thermochemical piles (*i.e.* large low-shear-velocity provinces, LLSVP: Li and McNamara, 2018). Conversely, a general *consensus* is that most of the subducted crust is variably stirred into the background mantle and completely dissolved, in a time span that varies from 0.1 to 1 Ga (Kumari et al., 2016; White, 2015; Foley and Rizo, 2017; Yu et al., 2018).

Using the phase proportions of *Mg-pv*, *Mg-Al-pv* and *cor* as a function of the exchanged alumina according to reaction (5), we can reconstruct the probability to find *Mg-Al-pv* with a

given composition in Al_2O_3 (*i.e. occurrence probability*: p_o%). Note that p_o% must not be confused with the *chemical probability of formation*, *i.e.* *p*(J,chem), discussed in section 3.1 and that represents the mere probability to have the right oxide combination to form a given phase.

The probability of the occurrence of perovskite with low Al_2O_3-content *per* formula unit (0.01-0.15 mole fraction) is ~28% at 24 GPa/1919 K, and increases up to ~43% at 80 GPa/2550 K. In general, low alumina compositions (0.01-0.15 mole fractions) are dominant at any *P-T* explored (Fig. 9). On the contrary, the occurrence of *Mg-Al-pv* with high alumina contents in the range 0.19-0.30 mole fraction drops from ~9.8% to ~2%, passing from 24 GPa/1919 K to 80 GPa/2550 K, respectively. Compositions of natural Al-bearing perovskite, occurring as diamond inclusions and "*claimed*" to be ascribable to the lower mantle (Kaminsky, 2012; Harte and Richardson 2012; Harte et. 1999), lie in the Al_2O_3-range associated with the largest occurrence probability (*i.e.* p_o%). Leaving any opinion about their representativeness of the lower mantle mineralogy aside, there is a consistency between observations and our predictions (Fig. 9).

To conclude, *Mg-Al-pv* competes with *Mg-pv* to the phase composition of the lower mantle (Fig. 3) and the probability to find *Mg-Al-pv* in the lower mantle is almost of the same order of magnitude as *Mg-pv* (Fig. 9). In addition, the distribution of Al in *Mg-Al-pv* shows that, among the possible Al-bearing perovskite phases, the $(Mg_{0.89}Al_{0.11})(Si_{0.89}Al_{0.11})O_3$ composition is the likeliest, providing some 8% of the bulk perovskite at 80 GPa (Fig. 9). The occurrence of the Al-richest composition, *i.e.* $(Mg_{0.71}Al_{0.29})(Si_{0.71}Al_{0.29})O_3$, is always a very rare event, *i.e.* $p_o\% < 1.7\%$.

6. CONCLUSIONS

709 We modelled the capacity of perovskite to uptake aluminium in a non-primitive Earth's lower
710 mantle, because of an enrichment by 3 wt% of recycled crustal material (MORB-component).
711 The investigated region stretches from 24 to 80 GPa and is geochemically described in the
712 framework of pyrolite and chondrite reference models. The open system model here used to
713 predict perovskite Al-incorporation capacity is independent of the geochemical framework.
714 Aluminium is *globally* incorporated foremost *via* an increase of the Al-bearing perovskite
715 amount [*Mg-Al-pv*(24 GPa)/*Mg-Al-pv*(80 GPa)≈1.17], rather than by an increase of the Al_2O_3-
716 content in its chemical composition. At 32 GPa perovskite hosts Al_2O_3 at its maximum
717 capacity (λ_{Al2O3}=0.134 Al_2O_3 mole fraction) and conserves such a figure up to ~50 GPa; at
718 higher pressure, a continuous decrease of Al_2O_3-content in *Mg-Al-pv* composition takes place
719 up to 80 GPa (λ_{Al2O3}=0.107 Al_2O_3 mole fraction).
720 Approaching 80 GPa, perovskite reaches some sort of "saturation" of its capacity to host
721 aluminium, which can be considered as a prelude to instability, most likely leading to the
722 formation of other phases (*i.e*. structural change to post-perovskite) that accommodate Al.
723 This is in keeping with the resulting phase equilibria in the $MgSiO_3$-Al_2O_3 system, earlier
724 modelled at *P-T* conditions relevant for the Earth's deepest mantle (80-140 GPa/2000-4000
725 K).
726 The probability to observe a perovskite composition having an Al_2O_3 mole fraction up to 0.15
727 is about 28% at 24 GPa, increasing to 43% at 80 GPa; on the contrary, compositions in the
728 range 0.19-0.30 Al_2O_3 mole fraction drop their occurrence probability from 9.8 to 2.0%. In
729 light of this, the Al-content of perovskite cannot be directly related to *P-T* conditions of
730 formation, save that "large" Al_2O_3 contents suggest unlikely deep provenance, within the
731 range here explored.
732 The *total* Al_2O_3 that perovskite (amounting to 76 and 85 wt%, in pyrolite and chondrite
733 reference models, respectively) may host is on average 4.3-4.8 wt% of the lower mantle mass.
734 In particular, perovskite alone can account for an Al_2O_3-storage capacity that accommodates

735 100% Al_2O_3 predicted by a non-primitive chondrite model, and 90% Al_2O_3, forecast by a non-
736 primitive pyrolite model. Calcium-ferrite type phases are possible competitors of perovskite
737 in hosting aluminium (up to 1/5 of available Al), though their low *chemical probability of*
738 *formation* likely reduces such potential. In the case of a non-primitive pyrolite lower mantle,
739 Al-bearing phases other than perovskite should exist, and the CF-type phase is a candidate
740 that might compensate for the 10% gap in perovskite Al-incorporation capacity.
741
742 **AKNOWLEDGEMENTS**
743
744 This work was partly supported by PRIN-2015 20158A9CBM Grant (C.B) and PRIN 2017 -
745 2017L83S77 (A.P). The paper benefited from the English language editing provided by Steve
746 Deforie and Barbara Galassi (Brighton, U.K). The Authors are indebted to the associated
747 Editor and two anonymous Referees for their comments and suggestions, which remarkably
748 improved the quality of the originally submitted manuscript.
749
750 **APPENDIX I**
751
752 **I.1 Open and closed systems**
753
754 An open system is permeable to both energy (heat and work) and matter, which are
755 exchanged between the system and a reservoir (De Groot and Mazur 1984; Mikhailov and
756 Ertl 2017). A closed system is able to exchange with a reservoir energy only. Let us assume to
757 have a generic system in which the following reaction occurs (we restrict our discussion to
758 one reaction only, for the sake of simplicity)

$$\sum_j \nu_j A_j = \sum_k \nu_k A_k \Longrightarrow \sum_l \nu_l A_l = 0 \qquad \text{(I. a)}$$

where $\{A_j\}$ and $\{A_k\}$ are "reactants and products" or "phases", which we shall term "reactants" *tout court*. The evolution as a function of time of the l^{th}-reactant is given by

$$\frac{dn_l}{dt} = \nu_l \frac{d\varepsilon}{dt} + \frac{d\Delta n_l}{dt} \qquad \text{(I. b)}$$

where n_l means number of moles of the l^{th}-reactant; ε is the reaction rate; the first term of the right-hand side member represents the change in n_l due to the reaction (I.a); the second term accounts for a matter exchange with a reservoir.

We split the entropy of such a system into two terms (Prigogine 1968):

$$\frac{dS_{ext}}{dt} = \frac{\delta Q}{T} - \sum_l \frac{\mu_l}{T} \frac{d\Delta n_l}{dt} \qquad \text{(I. c)}$$

$$\frac{dS_{int}}{dt} = -\sum_l \frac{\nu_l \mu_l}{T} \frac{d\varepsilon}{dt} \qquad \text{(I. d)}$$

where S_{ext} is the contribution by an exchange of heat and matter with an external reservoir; S_{int} represents the entropy produced by the reaction itself. Combining equ.(I.b), (I.c) and (I.d), it follows that

$$\frac{dS}{dt} = \frac{\delta Q}{T} - \sum_l \frac{\nu_l \mu_l}{T} \left(\frac{d\varepsilon}{dt} + \frac{1}{\nu_l} \frac{d\Delta n_l}{dt} \right) \qquad \text{(I. e)}$$

where S is the total entropy. We focus our attention on *stationary* processes, which are not necessarily at equilibrium. They exhibit observables that do not change over time (Pokrovskii 2013), and therefore

$$\frac{dn_l}{dt} = 0 \qquad \text{(I. f. 1)}$$

$$\frac{dS}{dt} = 0 \qquad \text{(I. f. 2)}$$

Taking into account (I.b), (I.e) and (I.f.1), the fulfilment of the constraint (I.f.2) requires that δQ=0. Therefore, it can be concluded that a stationary system is characterized by a possible exchange of matter with a reservoir, but not an exchange of heat.

I.2 Open system representation

The correct treatment of a system like the one introduced above requires, in principle, to be able to formulate explicitly both (I.c) and (I.d). Our aim is simpler, as we would like to exploit the capacity of an open system to freely exchange matter with a reservoir, in combination with a formalism as close as possible to the consolidated equilibrium thermodynamics' one. Such a model provides a flexible tool to approach problems in which one investigates the intrinsic exchanging/incorporation capacity of a given substance, without any sort of constraint or restraint.

An internal observer (*i.e.* an observer who measures the system's observables only, unaware of the matter flow) perceives a stationary open system as one that is under equilibrium conditions (P,T and $\{n_j\}$ do not change over time and δQ=0). Therefore, all the state functions are invariant *versus* t and the system conserves its composition), with possible forward-backward reactions and without any in/out-flow of energy/matter. Let us represent the chemical potential of the l-reactant by the usual expression below,

$$\mu_l = \mu_{0l} + RTln(x_l) + RTln(\gamma_{l,int}) \qquad \text{(I. g)}$$

where μ_{0l} is the component that depends on P-T only, and coincides with the Gibbs energy of the l^{th}-reactant alone; $\gamma_{l,int}$ is the activity coefficient of the l^{th}-reactant according to the internal observer and incorporates any sort of deviation from ideal mixing.

Let us assume that $\{n_l\}$ can fluctuate, δn_i, in such a way that (I.f.1) is satisfied *on average*, yet preserving the global system's composition. Therefore, the internal observer perceives that the conservation of composition is achieved through a transformation of the reactants into each other, according to the classical relationship below

$$\frac{\delta n_l}{\nu_l} = \delta\hat{\varepsilon} \qquad \text{(I. h)}$$

for any l-reactant; $\delta\hat{\varepsilon}$ is the infinitesimal change of the reaction ratio, seen by the internal observer. Using the equation above, we have that

$$dG = \left[\sum_l \nu_l \mu_{0l} + RTln\left(\prod_l x_l^{\nu_l}\right) + RTln\left(\prod_l \gamma_{l,int}^{\nu_l}\right)\right] \delta\hat{\varepsilon} \qquad \text{(I. i)}$$

799 The internal observer states that dG=0, given that the system is supposed at equilibrium, and
800 from (I.i) the usual chemical equilibrium equation follows

$$exp\left(-\frac{\sum_l \nu_l \mu_{0l}}{RT}\right) = \frac{\prod_k x_k^{\nu_k}}{\prod_j x_j^{\nu_j}} \times \frac{\prod_k \gamma_{k,int}^{\nu_k}}{\prod_j \gamma_{j,int}^{\nu_j}} = K(P,T)_{int} \qquad \text{(I. k)}$$

801 An external observer (*i.e.* an observer that is aware of the matter flow) confirms that dG=0 as
802 the system lies in a stationary state, and using (I.b) expresses dG in terms of

$$dG = \left[\sum_l \nu_l \mu_{0l} + RTln\left(\prod_l x_l^{\nu_l}\right) + RTln\left(\prod_l \gamma_{l,ext}^{\nu_l}\right)\right] \delta\varepsilon + \left[\sum_l \delta\Delta n_l \mu_{0l} + RTln\left(\prod_l x_l^{\delta\Delta n_l}\right) + RTln\left(\prod_l \gamma_{l,ext}^{\delta\Delta n_l}\right)\right] \qquad \text{(I. l)}$$

803 where $\delta\Delta n_l$ is the fluctuation due to the amount of l-reactant supplied by the reservoir *via* a
804 matter flow; $\gamma_{l,ext}$ is the activity coefficient estimated by the external observer. Given that the
805 global system's composition does not change in a stationary state, then the following
806 relationship must hold for $\delta\Delta n_l$, too,

$$\frac{\delta\Delta n_l}{\nu_l} = \delta\zeta$$

807 which implies

$$dG = \left[\sum_l \nu_l \mu_{0l} + RTln\left(\prod_l x_l^{\nu_l}\right) + RTln\left(\prod_l \gamma_{l,ext}^{\nu_l}\right)\right](\delta\varepsilon + \delta\zeta) \qquad \text{(I. m)}$$

808 Equ.(I.m), in combination with dG=0, leads to an expression similar to (I.k), save the term
809 depending on the activity coefficients, *i.e.* $\prod_l \gamma_{l,ext}^{\nu_l}$, so that

$$exp\left(-\frac{\sum_l \nu_l \mu_{0l}}{RT}\right) = \frac{\prod_k x_k^{\nu_k}}{\prod_j x_j^{\nu_j}} \times \frac{\prod_k \gamma_{k,ext}^{\nu_k}}{\prod_j \gamma_{j,ext}^{\nu_j}} = K(P,T)_{ext} \qquad \text{(I. n)}$$

810 Therefore, the γ activity coefficients "collect" the deviations from equilibrium that the internal
811 and external observers detect. For (I.n) and (I.k) to coincide with one another, $\prod_l \gamma_{l,ext}^{\nu_l} =$
812 $\prod_l \gamma_{l,int}^{\nu_l}$ must hold.

An open system may change its composition evolving towards a stationary state, according to the expression below, for the l^{th}-reactant:

$$\int_0^{\infty} \frac{d\Delta n_l}{dt} dt = \Delta n_l(\infty) - \Delta n_l(0)$$

where it can be assumed that at $t \to \infty$ the open system has achieved a stationary state.

I.3 Reactant proportions and probability

What does it physically mean to neglect the activity coefficients in equations (I.n) and (I.k)? Let us assume that a system has a known average Gibbs energy value, *i.e.* $<G>$ at *P*-*T*, and that it may occupy given "states", each one with a probability $\{p_l\}$. Following a consolidated approach of statistical mechanics and information theory (Jaynes 1957a-b), we state that the likeliest and least prejudicial $\{p_l\}$-set constrained to yield $<G>$ must correspond to an extreme of the expression beneath

$$\Phi = -R \sum_l p_l \ln(p_l) + \psi \left[\sum_l p_l G_l - < G > \right] \qquad \text{(I. o)}$$

where G_l is the Gibbs energy of the l^{th}-state; R is the gas constant and ψ is a lagrangian multiplier. If one requires that $\delta\Phi=0$, then

$$p_l \propto \exp\left(-\frac{G_l}{RT}\right) \qquad \text{(I. p)}$$

taking $\psi=1/T$. Let us shape our system in terms of a multi-phase system, in which the "states" are represented by the "reactants" that can occur. Let the system undergo a reaction like (I.a) and be composed of the related reactants. We analyse equ.(I.a) in statistical terms. The occurrence of the left-hand or right-hand side member, can be modelled using the notion of "joint probability", thus obtaining

$$p_{left-hand\ side\ member} \propto \prod_j p_j^{\nu_j}$$

and

$$p_{right-hand\ side\ member} \propto \prod\nolimits_k p_k^{\nu_k}$$

We take the ratio $p_{right\text{-}hand\ side\ member}/p_{left\text{-}hand\ side\ member}$, and observe that it can be either written as

$$\prod\nolimits_l p_l^{\nu_l}$$

or formulated as

$$\prod\nolimits_l \left[exp\left(-\frac{G_l}{RT}\right)\right]^{\nu_l} = exp\left(-\frac{\sum_l \nu_l G_l}{RT}\right)$$

by means of (I.p). Hence, the equations above lead to

$$\prod\nolimits_l p_l^{\nu_l} = exp\left(-\frac{\sum_l \nu_l G_l}{RT}\right) \qquad \text{(I. q)}$$

Equ.(I.q) is readily likened to (I.n) and (I.k), neglecting the activity coefficients and setting for each phase $G_l \equiv \mu_{0l}$. Altogether, a chemical equilibrium equation is thus formulated in a very simple and general fashion, which holds for stationary systems, too. Therefore, neglecting the activity coefficient terms in (I.n) and (I.k) leads to revising the notion of "l^{th}-reactant proportion", x_l, in terms of "l^{th}-reactant occurrence probability", p_l, *i.e.* $x_l \equiv p_l$, once a given reaction is being considered.

APPENDIX II

II.1 Approximation to unity of the activity coefficients term of equ.(7.a)

The activity coefficient term of equ.(7.a) can be simplified as

$$\gamma = \frac{\gamma_1}{\gamma_2^{1-\lambda} \times \gamma_3^{\lambda}} \qquad \text{(II. a)}$$

where we replaced *Mg-Al-pv*, *Mg-pv* and *cor* with 1, 2 and 3, respectively. Let us introduce the geometric average of the $\gamma_{1,2,3}$s, *i.e.*

$$\gamma_{ave} = (\gamma_1 \times \gamma_2 \times \gamma_3)^{1/3}$$

851 and

$$\gamma_1 = \gamma_{ave} + \delta_1 \qquad \text{(II. b. 1)}$$

$$\gamma_2 = \gamma_{ave} + \delta_2 \qquad \text{(II. b. 2)}$$

$$\gamma_3 = \gamma_{ave} + \delta_3 \qquad \text{(II. b. 3).}$$

852 Replacing γs in (II.a) with (II.b.1-2-3), then it is obtained

$$\gamma = \frac{\left(1+\frac{\delta_1}{\gamma_{ave}}\right)}{\left(1+\frac{\delta_2}{\gamma_{ave}}\right)^{1-\lambda} \times \left(1+\frac{\delta_3}{\gamma_{ave}}\right)^{\lambda}} \approx \frac{\left(1+\frac{\delta_1}{\gamma_{ave}}\right)}{\left(1-(1-\lambda)\frac{\delta_2}{\gamma_{ave}}\right) \times \left(1-\lambda\frac{\delta_3}{\gamma_{ave}}\right)} \approx$$

$$\approx \left(1+\frac{\delta_1}{\gamma_{ave}}\right) \times \left(1+(1-\lambda)\frac{\delta_2}{\gamma_{ave}}\right) \times \left(1+\lambda\frac{\delta_3}{\gamma_{ave}}\right)$$

$$\approx 1 + \frac{\delta_1 + (1-\lambda)\delta_2 + \lambda\delta_3}{\gamma_{ave}} + o\left(\left(\frac{\delta}{\gamma_{ave}}\right)^2\right) \approx 1 \qquad \text{(II. c)}$$

853 The approximation above requires $\delta/\gamma_{ave}<1$, which holds in most cases. In fact, earlier excess
854 enthalpy determinations on some H*P*-minerals (for instance, Fe-periclase: Sreçec et al. 1987;
855 garnets: Geiger et al. 1987; olivine: Kojitani and Akaogi 1994; Al-perovskite: Akber-Knutson
856 and Bukowinski 2004; Panero et al. 2006) exhibit absolute Δ*H*-maximum-values that yield
857 average activity coefficients [estimated by $exp(\Delta H_{max}/RT)$, T=2000 K] lying between 1.07 and
858 1.34, with a geometric average of 1.2 and $<\delta/\gamma_{ave}>$~0.08. Note that $\delta_1+\delta_2(1-\lambda)+\delta_3\lambda$ is
859 expected to be in general small as the δs compensate each other, due to δ_1, δ_2, and δ_3 not
860 being of the same sign. Therefore, given that we can legitimately neglect the activity
861 coefficient in the case of equ.(7.a), x_ls and p_ls coincide with each other, according to
862 APPENDIX I.3.

REFERENCES

Akber-Knutson S. and Bukowinski M.S.T. (2004) The energetics of aluminium solubility into $MgSiO_3$ perovskite at lower mantle conditions. *Earth Planet. Sci. Lett.* **220**, 317–330

Akber-Knutson S., Steinle-Neumann G. and Asimow, P.D. (2005) Effect of Al on the sharpness of the $MgSiO_3$ perovskite to post-perovskite phase transition. *Geophys. Res. Lett.* **32,** L14303.

Anderson D.L. (1989) Composition of the Earth. *Science* **243**, 367–370.

Badro J., Cote A. S., Brodholt J. P. (2014) A seismologically consistent compositional model of Earth's core, *Proc. Nat. Acad. Sci*. USA., **111,** 7542–7545.

Baker J.A., Schiller M., Bizzarro M. (2012) ^{26}Al-^{26}Mg deficit dating ultramafic meteorites and silicate planetesimal differentiation in the early Solar System? *Geochim. et Cosmochim. Acta*, **77**, 415-431.

Ballmer M.D., Houser C., Hernlund J.W., Wentzcovitch R.M., and Hirose K. (2017) Persistence of strong silica-enriched domains in the Earth's lower mantle. *Nat. Geosci.* DOI: 10.1038/NGEO2898.

Billen, M. I. (2010) Slab dynamics in the transition zone. Phys. Earth Planet. Inter. 183, 296–308.

Brown J. M., Shankland T. J. (1981). Thermodynamic parameters in the Earth as determined from seismic profiles. *Geoph. J. Royal Astronom. Soc*. **66**, 579–596.

Christensen U. R., Yuen D. A., (1984) The interaction of a subducting lithospheric slab with a chemical or phase boundary. *J. Geophys. Res*. **89**, 4389–4402

Christensen, U. R., Hofmann A. W. (1994) Segregation of subducted oceanic crust in the convecting mantle, *J. Geophys. Res*., **99**, 19,867 –19,884.

887 Bina C.R. and Helffrich G. (2014) Geophysical Constraints on Mantle Composition. In:
888 *Treatise on Geochemistry, Second Edition,* Vol. 3 (eds: H.D. Holland and K.K Turekian),
889 Elsevier. Oxford pp. 41-65.
890 Bizzarro M., Baker J., Haack H., Lundgaard K. (2005) Rapid timescales for accretion and
891 melting of differentiated planetesimals inferred from ^{26}Al–^{26}Mg chronometry.
892 *Astrophys. J.*, **632**, L42-L44.
893 Burton B.P., van de Walle, A. (2003) First principles based calculations of the CaCO3–
894 MgCO3 subsolidus phase diagrams. *Phys. Chem. Miner.*, **30**, 88-97.
895 Catti M., Valerio G., Dovesi R. and Causà M. (1994) Quantum-mechanical calculation of the
896 solid-state equilibrium $MgO+\alpha\text{-}Al_2O_3 \rightleftarrows MgAl_2O_4$ (spinel) versus pressure. *Phys. Rev.*
897 *B*, **49**, 14179.
898 Causà M., Dovesi R., Pisani C. and Roetti, C. (1986) Electronic structure and stability of
899 different crystal phases of magnesium oxide. *Phys. Rev. B*, **33**, 1308-1316.
900 Chust T.C., Steinle-Neumann G., Dolejš D., Schuberth B. S. A. and Bunge H.P. (2017)
901 MMA-EoS: A Computational Framework for Mineralogical Thermodynamics. *J.*
902 *Geophys. Res.: Solid Earth*, **122**, 9881–9920. https://doi.org/10.1002/2017JB014501.
903 Corà F. (2005) The performance of hybrid density functionals in solid state chemistry: the
904 case of BaTiO3. *Mol. Phys*. **103**, 2483-2496.
905 De Groot S.R. and Mazur P. (1984) Non-equilibrium thermodynamics. Dover Publications.
906 Dovesi R., Saunders V.R., Roetti C., Orlando,R., Zicovich-Wilson C.M., Pascale F., Civalleri
907 B., Doll K., Harrison N.M., Bush I.J., D'Arco P., Llunell, M. (2009) CRYSTAL09
908 user's manual. University of Torino, IT, Torino.
909 Faure G. (1986) *Principles of Isotopic Geology* Wiley, New York.
910 Foley B.J., Rizo H. (2017) Long-term preservation of early formed mantle heterogeneity by
911 mobile lid convection: Importance of grainsize evolution. Earth Planet. Sci. Lett. **475**,
912 94–105

913 Fukuyama K., Ohtani E., Shibazaki Y., Kagi H., Suzuki A. (2017) Stability field of phase
914 Egg, $AlSiO_3OH$ at high pressure and high temperature: possible water reservoir in mantle
915 transition zone. *J. Mineral. Petrol. Sci*. **112**, 31-35.
916 Funamori N., Jeanloz R. (1997) High-Pressure Transformation of Al_2O_3 . *Science*, **278,** 1109-
917 1111. DOI: 10.1126/science.278.5340.1109.
918 Funamori N., Jeanloz R., Miyajima N., and Fujino K. (2000) Mineral assemblages of basalt in
919 the lower mantle, *J. Geophys. Res*., **105**, 26,037–26,043, doi:10.1029/2000JB900252
920 Gale A., Dalton C.A., Langmuir C.H., Su Y. and Schilling J.-G. (2013) The mean
921 composition of ocean ridge basalts. *Geochem. Geophys. Geosyst.***, 14,** 489–518,
922 doi:10.1029/2012GC004334.
923 Gale J.D. (1997) GULP-a computer program for the symmetry adapted simulation of solids.
924 *JCS Faraday Trans*, **93**, 629–637.
925 Gale J.D. (2005) GULP: Capabilities and prospects, *Z. Krist.*, **220**, 552-554.
926 Gasparik T., Tripathi A. and Parise J.B. (2000) Structure of a new Al-rich phase, [K,
927 Na]0.9[Mg, Fe]2[Mg, Fe, Al, Si]6O12, synthesized at 24 GPa. *Am. Mineral.*, **85**, 613–
928 618.
929 Geiger CA, Newton RC, Kleppa OJ (1987) Enthalpy of mixing of synthetic almandine-
930 grossular and almandine-pyrope garnets from high-temperature solution calorimetry.
931 *Geochim. Cosmochim. Acta*, **51**, 1755-1763.
932 Ghosh S. and Schmidt M.W. (2014) Melting of phase D in the lower mantle and implications
933 for recycling and storage of H2O in the deep mantle. *Geochim. Cosmochim. Acta*, **145**
934 72–88.
935 Guignot N. and Andrault D. (2004) Equations of state of Na–K–Al host phases and
936 implications for MORB density in the lower mantle. Phys Earth Planet. Int., 143-144:
937 107-128.

938 Harte B. and Richardson S. (2012) Mineral inclusions in diamonds track the evolution of a
939 Mesozoic subducted slab beneath West Gondwanaland. *Gond. Res*. **21,** 236–245.
940 Harte B., Harris J.W., Hutchison M.T., Watt G.R. and Wilding, M.C. (1999) Lower mantle
941 mineral associations in diamonds from Sao Luiz, Brazil. In: *Mantle Petrology: Field*
942 *Observations and High Pressure Experimentation*; *a tribute to Francis R. (Joe) Boyd*
943 *(*eds: Y. Fei, C.M. Bertka and B.O. Mysen). The Geochemical Society Special
944 Publication No 6, pp 125-153.
945 Hirose K., Fei Y., Ma Y., Mao H-K. (1999) The fate of subducted basaltic crust in the Earth's
946 lower mantle. *Nature* 397, 53–56.
947 Hirose K., Takafuji N., Nagayoshi S. and Ohishi Y. (2005) Phase transition and density of
948 subducted MORB crust in the lower mantle. *Earth Planet. Sci. Lett.* **237** 239– 251.
949 Honda S. (2017) Geodynamic Modeling of the Subduction Zone around the Japanese Islands.
950 *Monogr. Environ. Earth Planets,* **5** (2), 35–62.
951 Imada S., Hirose K., Komabayashi T., Suzuki T., Ohishi Y. (2012) Compression of
952 $Na_{0.4}Mg_{0.6}Al_{1.6}Si_{0.4}O_4$ NAL and Ca-ferrite-type phases. *Phys. Chem. Min*., **39**, 525-530.
953 Imada S., Hirose K., Ohishi Y. (2011) Stability of NAL and Ca-ferrite-type phases on the
954 join $NaAlSiO_4$-$MgAl_2O_4$. *Phys. Chem. Min*., **38**, 557-560.
955 Ismailova L., Bykova E., Bykov M., Cerantola V., McCammon C., Boffa Ballaran T., Bobrov
956 A., Sinmyo R., Dubrovinskaia N., Glazyrin K., Liermann H.P., Kupenko I., Hanfland M.,
957 Prescher C., Prakapenka V., Svitlyk V., Dubrovinsky L. (2016) Sgtability of Fe,Al-
958 bearing bridgmanite in the lower mantle and synthesis of pure Fe-bridgmanite. *Sci.*
959 *Advances*, **2**, e1600427.
960 Irifune T., Ringwood A.E., 1993 Phase transformations insubducted oceanic crust and
961 buoyancy relationships at depth of 600–800 km in the mantle. *Earth Planet. Sci.* **117**,
962 101–110.

963 Irifune T., Shinmei T., McCammon C.A., Miyajima N., Rubie D.C. and Frost D.J. (2010) Iron
964 partitioning and density changes of pyrolite in Earth's lower mantle. *Science* **327**, 193–
965 195.
966 Irifune T., Fujino K., Ohtani E. (1991) A new high-pressure form of $MgAl_2O_4$. *Nature*, **349**,
967 409-411.
968 Irifune T., Koizumi T., Ando, J. I. (1996) An experimental study of the garnet–perovskite
969 transformation in the system $MgSiO_3$–$Mg_3Al_2Si_3O_{12}$. *Phys. Earth Planet. In.* **96**, 147–157.
970 doi:10.1016/0031-9201(96)03147-0.
971 Jaynes E.T. (1957a) "Information Theory and Statistical Mechanics" (PDF). *Phys. Rev*. Series
972 II, **106**, 620–630.
973 Jaynes E.T. (1957b) "Information Theory and Statistical Mechanics" (PDF). *Phys. Rev*. Series
974 II, **108**, 171-190.
975 Javoy M., Kaminski E., Guyot F., Andrault D., Sanloup C., Moreira M., Labrosse S., Jambon
976 A., Agrinier P., Davaille A. and Jaupart C. (2010) The chemical composition of the
977 Earth: Enstatite chondrite models. *Earth and Planet. Sci. Lett*, **293**, 259-268. DOI:
978 10.1016/j.epsl.2010.02.033.
979 Jeanloz R., Knittle E. (1989) Density and composition of the lower mantle. *Phil.Trans. Royal*
980 *Soc Lon.* **A328(1599),** 377–389 doi:10.1098/rsta.1989.0042
981 Jones R.E. van Keken P. E., Hauri E., Tucker J. M., Vervoort, J., Ballentine C. J. (2019)
982 Origins of the terrestrial Hf-Nd mantle array: Evidence from a combined geodynamical-
983 geochemical approach. *Earth and Planet. Sci. Lett*, **518**, 26-39
984 Kaminski E. and Javoy, M. (2013) A two-stage scenario for the formation of the Earth's
985 mantle and core. *Earth Planet. Sci. Lett.* **365,** 97-107.
986 Kaminsky F. (2012) Mineralogy of the lower mantle: a review of super-deep mineral
987 inclusions in diamond. *Earth Sci. Rev*. **110**, 127–147.

Kaminsky F. and Lin J-F. (2017) Iron partitioning in lower mantle minerals: toward a chemically heterogeneous lower mantle. *Am Miner.*, **102**, 824-832.

Kato C., Hirose K., Komabayashi T., Ozawa H. and Ohishi, Y. (2013) NAL phase in K-rich portions of the lower mantle. *J. Geophys. Res.* **40**, 5085–5088.

King, S. D Frost . D. J., Rubie, D. C. (2015) Why cold slabs stagnate in the transition zone. *Geology* **43**, 231–234.

Kojitani H, Akaogi M (1994) Calorimetric study of olivine solid solutions in the system Mg_2SiO_4-Fe_2SiO_4. *Phys. Chem. Miner*., **20**, 536–540.

Korenaga J. (2009) A method to estimate the composition of the bulk silicate Earth in the presence of a hidden geochemical reservoir. *Geochim. Cosmochim. Acta,* **73,** 6952–6964.

Kröger F.A. (1972) *The Chemistry of Imperfect Crystals*. North-Holland, Amsterdam

Kumari S., Paul D. and Stracke A. (2016) Open system models of isotopic evolution in Earth's silicate reservoirs: Implications for crustal growth and mantle heterogeneity. *Geochim. Cosmochim. Acta* **195** 142–157.

Kurnosov A., Marquardt H., Frost D.J., Boffa Ballaran T. and Ziberna L. (2017) Evidence for a Fe^{3+}-rich pyrolytic lower mantle from (Al,Fe)-bearing bridgmanite elastic data. *Nature*, **543**, 543-546.

Lee T., Papanastassiou D.A., Wasserburg G.J. (1977) Al-26 in the early Solar-System – fossil or fuel. *Astrophys. J*., **211**, L107-L110.

Jie Li J., Viktor V. Struzhkin V.V., Mao H-k, Shu J., Hemley R.J., Fei Y., Mysen B., Dera P., Prakapenka V., Shen G. (2004) Electronic spin state of iron in lower mantle perovskite. *Proc. Nat. Acad. Sci*. USA., **101** 14027-14030

Li , L., Weidner, D.J., Brodholt, J., Alfè, D., Price, G.D. (2008) Ab initio molecular dynamics study of elasticity of akimotoite $MgSiO_3$ at mantle conditions. *Phys. Earth and Planet. Inter*. **173**, 115-120.

1013 Li M., McNamara A. K. (2013) The difficulty for subducted oceanic crust to accumulate at
1014 the Earth's core-mantle boundary. *J. Geophys. Res. Solid Earth*, **118**, 1807–1816,
1015 doi:10.1002/jgrb.50156
1016 Li M. , McNamara A. K. (2018) The influence of deep mantle compositional heterogeneity
1017 on Earth's thermal evolution. *Earth Planet. Sc. Lett.*, **500**, 86–96
1018 Litasov K. D., Ohtani E (2007) Effect of water on the phase relations in Earth's mantle and
1019 deep water cycle. Special Paper of the Geological Society of America, **421**, 115-156
1020 DOI: 10.1130/2007.2421(08)
1021 Lodders K. (2003) Solar system abundances and condensation temperatures of the elements.
1022 *Astrophys. J.* **591**, 220–1247.
1023 Lodders K., Palme H., and Gail H-P. (2009) Abundances of the elements in the solar system.
1024 In: *Astronomy and Astrophysics* Vol. VI/4B, Chap. 4.4 (ed. J.E Trumper). Landolt-
1025 Bornstein, New Series Berlin, Springer-Verlag, pp. 560-630.
1026 Lyubetskaya T. and Korenaga J. (2007) Chemical composition of Earth's primitive mantle
1027 and its variance *J. Geoph. Res.* **112**, B03211, doi:10.1029/2005JB004223.
1028 Mahan B., Siebert J., Blanchard I., Borensztajn S., Badro J. and Moynier F. (2018)
1029 Constraining compositional proxies for Earth's accretion and core formation through high
1030 pressure and high temperature Zn and S metal-silicate partitioning. *Geochim.*
1031 *Cosmochim. Acta*, **235**, 21-40.
1032 Marty B. (2012). The origins and concentrations of water, carbon, nitrogen and noble gases
1033 on Earth. *Earth Planet. Sci. Lett*. **313**, 56–66.
1034 Mattern E, Matas J., Ricard Y., Bass J. (2005) Lower mantle composition and temperature
1035 from mineral physics and thermodynamic modelling. *Geophys. J. Int.* **160**, 973–990.
1036 McDonough WF and Sun S-S (1995) The composition of the Earth. *Chem. Geol.* **120**: 223-
1037 253.
1038 McDonough W. F. (2014), Compositional model for the Earth's core. In The Mantle and

1039 Core, edited by R. W. Carlson, pp. 559–577, Elsevier, Amsterdam.
1040 Merli M. and Pavese A. (2018) Electron-density critical points analysis and catastrophe
1041 theory to forecast structure instability in periodic solids. *Acta Crystallograph. Section A*:
1042 *Foundations and Advances* **74**, 102-111.
1043 Merli M., Sciascia L., Pavese A. and Diella V. (2015) Modelling of thermo-chemical
1044 properties over the sub-solidus MgO–FeO binary, as a function of iron spin
1045 configuration, composition and temperature. *Phys. Chem. Min*. **42**, 347-362.
1046 Merli M., Bonadiman C., Diella V. and Pavese A. (2016) Lower mantle hydrogen partitioning
1047 between periclase and perovskite: A quantum chemical modelling. *Geoch. Cosmochim.*
1048 *Acta* **173**, 304-318.
1049 Merli M., Bonadiman C., Diella V., Sciascia L. and Pavese A. (2017) Fe-periclase reactivity
1050 at Earth's lower mantle conditions: *ab-initio* geochemical modelling. *Geochim.*
1051 *Cosmochim. Acta*, **214**, 14-29. https://doi.org/10.1016/j.gca.2017.07.030.
1052 Mikhailov A.S., Ertl G. (2017) Thermodynamics of Open Systems. In: Chemical Complexity.
1053 The Frontiers Collection. Springer, Cham.
1054 Mohn C.E. and Trønnes R. (2016) Iron spin state and site distribution in FeAlO3-bearing
1055 bridgmanite. *Earth Plan. Sci. Lett*., **440**, 178-186.
1056 Murakami M., Hirose K., Kawamura K., Sata N. and Ohishi Y. (2004) Post-perovskite phase
1057 transition in MgSiO3. *Science* **304**, 855-858
1058 Muir J.M.R., Brodholt J.P. (2018) Water distribution in the lower mantle: Implications for
1059 hydrolytic weakening. *Earth Plan. Sci. Lett*., **484** , 363-369. 10.1016/j.epsl.2017.11.051
1060 Murakami M., Ohishi Y., Hirao N. and Hirose K. (2012) A perovskitic lower mantle inferred
1061 from high-pressure, high-temperature sound velocity data. *Nature* **485,** 90- 95.
1062 Navrotsky A., Schoenitz M., Kojitani H., Xu H., Zhang, J., Weidner D.J. and Jeanloz R.
1063 (2003) Aluminium in magnesium silicate perovskite: Formation, structure, and energetics

of magnesium-rich defect solid solutions. *J. Geophys. Res.* **108**, B7, 2330, doi:10.1029/2002JB002055.

Nestola F., Korolev N., Kopylova M., Rotiroti N., Pearson D.G., Pamato M.G., Alvaro M., Peruzzo L, Gurney J.J., Moore A.E. and Davidson J. (2018) $CaSiO_3$ perovskite in diamond indicates the recycling of oceanic crust into the lower mantle. *Nature* **555**. 237-241.

Nishio-Hamane D., Nagai T., Fujino K., Seto Y., Takafuji N. (2005) Fe^{3+} and Al solubilities in $MgSiO_3$ perovskite: implication of the Fe^{3+}AlO3 substitution in $MgSiO_3$ perovskite at the lower mantle condition. *Geophy. Res. Lett*. **32**, L16306.

Nolet G., Allen R. and Zhao D. (2007) Mantle plume tomography. *Chem. Geol*. **241**, 248–263.

Norris T.L., Gancarz A.J., Rokop D.J., Thomas K.W. (1983) Half-life of ^{26}Al. *J. Geophys. Res*., **88** (S1), B331-B333.

Ohtani, E., Litasov, K., Suzuki, A., and Kondo, T. (2001) Stability field of new hydrous phase, δ-AlOOH, with implications for water transport into the deep mantle: *Geophys. Res. Lett.*, **28,** 3991–3993.

Ohtani E., Amaike Y., Kamada S., Sakamaki T. and Hirao N. (2014) Stability of hydrous phase H $MgSiO_4H_2$ under lower mantle conditions. *Geophys. Res. Lett.*, **41**, 8283-8287

Ottonello G. (1997) *Principles of Geochemistry*. Columbia University Press, New York

Ottonello G., Civalleri B., Ganguly J., Perger W.F., Belmonte D. and Vetuschi Zuccolini M., (2010) Thermo-chemical and thermos-physical properties of the high pressure phase Anhydrous B ($Mg_{14}Si_5O_{24}$): an *ab initio* all-electron investigation. *Am. Mineral*. **95**, 563–573.

Palme H. and O'Neill, H., (2014) . Cosmochemical estimates of mantle composition. In: *Treatise on Geochemistry*, 2nd Edition. Vol. 3 (ed. R. W Carlson). Elsevier, Oxford pp. 1–39.

1090 Pamato M.G., Myhill R., Boffa Ballaran T., Frost D.J., Heidelbach F. and Miyajima N. (2015)
1091 Lower-mantle water reservoir implied by the extreme stability of a hydrous
1092 aluminosilicate. *Nat. Geosci.* **8**, 75–79.
1093 Panero W.R., Akber-Knutson S. and Stixrude L. (2006) Al_2O_3 incorporation in MgSiO3
1094 perovskite and ilmenite. *Earth Planet. Sci. Lett*. **252**, 152-161.
1095 PetDB Petrological Database (https://www.earthchem.org/petdb)
1096 Prigogine I. (1968) Introduction to thermodynamics of irreversible processes. Third Edition.
1097 John Wiley & Sons Inc, N.Y. 9
1098 Pokrovskii V.N. (2013) A derivations of the main relations of non-equilibrium
1099 thermodynamics. *IRSN Thermodynamics,* 906136, pp 9. doi: 10.1155/2013/906136
1100 Ricolleau A., Fiquet G., Addad A., Menguy N., Vanni C., Perrillat J.P., Daniel I., Cardon H.,
1101 and Guignot N. (2008) Analytical transmission electron microscopy study of a natural
1102 MORB sample assemblage transformed at high pressure and high temperature, *Am. Min*.,
1103 **93**, 144–153, doi:10.2138/am.2008.2532.
1104 Ricolleau A., Fei Y., Cottrell E., Watson H.C., Deng L., Zhang L., Fiquet G., Auzende A.-L.,
1105 Roskosz M., Morard G. and Prakapenka V. (2009) Density profile of perovskite under the
1106 lower mantle conditions. *Geophys. Res. Lett*. **36**, L06302.
1107 Ricolleau A., Perrillat J.P., Fiquet G., Daniel I., Matas J., Addad A. Menguy N., Cardon H.,
1108 Mezouar M. and Guignot N. (2010) Phase relations and equation of state of a natural
1109 MORB: Implications for the density profile of subducted oceanic crust in the Earth's
1110 lower mantle. *J. Geophys. Res.*,**115**: B08202.
1111 Shim S-H, Catalli K., Hustoft J., Kubo A., Prakapenka V.B, Caldwell W.A., Kunz M.
1112 (2018) Crystal structure and thermoelastic properties of $(Mg_{0.91}Fe_{0.09})SiO_3$ postperovskite
1113 up to 135 GPa and 2,700 K. *Proc. Nat. Acad. Sci. U. S. A* **105**, 7382–7386
1114 Sreçec I., Ender A., Woermann E., Gans W., Jacobsson E., Eriksson G., Rosen E. (1987)
1115 Activity-composition relations of the magnesiowüstite solid solution series in equilibrium

with metallic iron in the temperature range 1050–1400 K. *Phys. Chem. Miner.*, **14**, 492–498.

Sigloch K., McQuarrie N. and Nolet G. (2008) Two-stage subduction history under North America inferred from multiple-frequency tomography, *Nat. Geosci.* **1**, 458–462, doi:10.1038/ngeo231.

Spivak-Birndorf, M. Wadhwa, P. Janney (2009) 26Al–26Mg systematics in D'Orbigny and Sahara 99555 angrites: implications for high-resolution chronology using extinct chronometers. *Geochim. Cosmochim. Acta*, **73**, 5202-5211.

Stebbins J.F., Kroeker S. and Andrault D. (2001) The mechanism of solution of aluminium oxide in MgSiO3 perovskite. *Geophys. Res. Lett*. **28**, 615–618.

Stixrude L., Lithgow-Bertelloni C. (2005), Thermodynamics of mantle minerals—I. Physical properties, *Geophys. J. Int*., **162**, 610–632.

Stixrude L. and Lithgow-Bertelloni C. (2012) Geophysics of chemical heterogeneity in the mantle. *Annual Rev. Earth Planet. Sci. Lett.* **40**, 569–595.

Tateno S., Hiros, K. Sata, N. and Ohishi, Y. (2009) Determination of post-perovskite phase transition boundary up to 4400K and implications for thermal structure in D''layer. *Earth Planet. Sci. Lett.* **277**, 130–136.

Thomson K. T., Wentzcovitch R. M. and Bukowinski, M. S. T. (1996) Polymorphs of Alumina Predicted by First Principles: Putting Pressure on the Ruby Pressure Scale. *Science* **274**, 1880–1882.

Towler M. (2015) CRYSTAL Resources Page. Theory of Condensed Matter http://www.tcm.phy.cam.ac.uk/~mdt26/crystal.html.

Tschauner O., Ma C., Prescherb C., Prakapenka V.B. (2018) Structure analysis and conditions of formation of akimotoite in the Tenham chondrite. *Meteor. and Planet. Sci*, **53**, 62-74.

Tsuchiya J., and Tsuchiya T. (2008) Post-perovskite phase equilibria in the $MgSiO_3$-Al_2O_3 system. *Proc. Nat. Acad. Sci. U. S. A* **105**, 19160-19164.

Valencia-Cardona J.J., Shukla G., Wu Z. , Houser C., Yuen D.A, Wentzcovitch R. M. (2017) Influence of the iron spin crossover in ferropericlase on the lower mantle geotherm. Geophys. Res.Lett., **44**, 4863–4871, doi:10.1002/2017GL073294.

van der Hilst R. D., Widiyantoro S. and Engdahl E. R. (1997) Evidence for deep mantle circulation from global tomography. *Nature* **386**, 578–584.

van de Walle A., Ceder G. (2002) The effect of lattice vibrations on substitutional alloy thermodynamics. *Rev. Mod. Phys*., **74**, 11-45.

Walter M.J., Kubo A., Yoshino T., Brodholt J.P., Koga K.T and Ohishi Y., (2004) Phase relations and equation-of-state of aluminous Mg-silicate perovskite and implications for Earth's lower mantle. *Earth Planet. Sci. Lett*. **222** 501–516.

Walter M.J. , Thomson A.R., Wanga W., Lord O.T., Ross J., McMahon S.C., Baron M.A., Melekhova E., Kleppe A.K. and Kohn S.C. (2015) The stability of hydrous silicates in Earth's lower mantle: Experimental constraints from the systems $MgO–SiO_2–H_2O$ and $MgO–Al_2O_3–SiO_2–H_2O$. *Chem. Geol.,* **418**, 16–29.

Wang K. and Jacobsen S.B. (2016) An estimate of the Bulk Silicate Earth potassium isotopic composition based on MC-ICPMS measurements of basalts. *Geochim. Cosmochim. Acta*, **173**, 223-232.

Wang X., Tsuchiya T., and Hase A. (2015) Computational support for a pyrolitic lower mantle containing ferric iron, Nat. Geosci., **8,** 556–559. doi:10.1038/ngeo2458.

Wasson J. T. and Kallemeyn G. W. (1988) Compositions of chondrites. *Philos. Trans. R. Soc. London, Ser. A,* **325**, 535 – 544.

White, W.M., 2015 Probing the Earth's deep interior through geochemistry. *Geochem. Perspect.***4 (2),** 95–251.

Wimpenny J., Sanborn M.E., Koefoed P., Cooke I.R., Stirling C., Amelin Y. and Qing-Zhu Yin Q-Z. (2019). Reassessing the origin and chronology of the unique achondrite Asuka

881394: Implications for distribution of 26Al in the early Solar System. *Geochim. Cosmochim. Acta*, **244**, 478–501.

Wu Y., Wu X., Lin J., McCammon C.A., Xiao Y., Chow P., Prakapenka V.B., Yoshino T., Zhai S. and Qin S. (2016) Spin transition of ferric iron in the NAL phase: Implications for the seismic heterogeneities of subducted slabs in the lower mantle. *Earth Planet. Sci. Lett.* **434** 91-100.

Wu S.C., Browne E. (1997). Comments on evaluation of ^{26}Al electron-capture and position decay data. Comments on Evaluation CEA. ISBN 2 7272 0211 3.

Wu Z. and Cohen R. E. (2006) More accurate generalized gradient approximation for solids. *Phys. Rev. B*, **73**:235116.

Yamamoto T., Yuen D.A. and Ebisuzaki T. (2003) Substitution mechanism of Al ions in MgSiO3 perovskite under high pressure conditions from first-principles calculations. *Earth Planet. Sci. Lett.* **206**, 617-625.

Young E.D., Simon J.I., Galy A., Russell S.S., Tonui E. and Lovera O. (2005) Supra-canonical ^{26}Al/^{27}Al and the residence time of CAIs in the solar protoplanetary disk. *Science* **308,** 5719.

Yu C., Day E.A., de Hoop M.V., Campillo M. and Goes S., Blythe R.A. and van der Hilst R.D. (2018) Compositional heterogeneity near the base of the mantle transition zone beneath Hawaii. *Nat. Comm*. **9**, 1266.

Zhang F. and Oganov A.R. (2006) Mechanisms of Al^{3+} incorporation in $MgSiO_3$ post-perovskite at high pressures. *Earth Planet. Sci. Lett.* **248**, 69-76.

Fukao Y. & Obayashi, M. 2013 Subducted slabs stagnant above, penetrating through, and trapped below the 660 km discontinuity. *J. Geophys. Res.* **118**, 5920 5938.

CAPTIONS TO THE FIGURES

Figure 1. Equilibrium constant, $K(P,T,\lambda)$, of the fundamental alumina exchange reaction (5) *versus* λ, which expresses the exchanged amount of Al_2O_3 in the *Mg-Al-pv*, *Mg-pv* and *cor* system. $K(P,T,\lambda)$, calculated by the open system model, is displayed at 24 GPa/1919 K (blue line), 44 GPa/2145 K (red line) and 80 GPa/2551 K (black line), by way of example. Black filled circles indicate the maxima at the three chosen *P-T* points, and correspond to the λ-values that most shift the reaction (1-λ) $MgSiO_3$+λ Al_2O_3 $\leftrightarrow$ $(Mg_{1-\lambda}Al_{\lambda})(Si_{1-\lambda}Al_{\lambda})O_3$ to the right (equ.5, of the text).

Figure 2. $K(P,T)_{ave}$ *versus P*, according to the chosen geotherm and calculated by the open system model. Blue line and red line show two different trends for the average equilibrium constant, $K(P,T)_{ave}$, of the reaction (5). Note that $K(P,T)_{ave}=\langle K(P,T,\lambda)\rangle_{\lambda}$ (see 4.2.1 section for further explanations).

Figure 3. Phase proportions of Al-free perovskite (*Mg-pv*), Al-bearing perovskite (*Mg-Al-pv*) and corundum (*cor*) *versus P*, according to the chosen geotherm. *Mg-Al-pv* fractions have an average Al_2O_3 composition provided by λ_{Al2O3}, calculated according to equ.(9.b) on the *P-T* range of interest and shown in Fig.5. Al-free perovskite is an extreme notion, which provides a "limit" to define a tendency of such mineral to incorporate aluminium.

Figure 4. Al_2O_3-partitioning between corundum and perovskite (*cor*(mol)/*Mg-Al-pv*(mol)) *versus P*, according to the chosen geotherm and calculated by the open system model. The red box shows the region of maximum Al-uptake for perovskite (saturation region), suggesting that at such *P-T* conditions the Al-incorporation is weakly dependent on pressure. At higher pressure, the *cor*/*Mg-Al-pv* ratio trend hints at a possible instability of perovskite (transition to another phase, such as post-perovskite, *ppv*?). See text for further discussion

Figure 5. Average Al_2O_3 mole fraction in perovskite, λ_{Al2O3}, determined by the open system model and calculated *via* equ.(9.b), as a function of *P* along the chosen geotherm. In the *P*-region 30-50 GPa, λ_{Al2O3} is *quasi* constant (interpolation solid line).

Figure 6. Al_2O_3 mole fraction in perovskite, $\xi_{closed\ system}$, determined by the closed system model and calculated *via* equ.(14), as a function of *P* along the chosen geotherm. At $\lambda=\xi_{closed\ system}$, $K(P,T,\lambda)$ takes an extreme value, so that reaction (5) is shifted to the right as much as possible.

Figure 7. Cell volume disagreement (%), between measurements and our calculations, in the case of Al-bearing perovskite, as a function of *P*. Experimental values from Walter et al (2004).

Figure 8. The predicted *total* Al_2O_3 (wt%) stored in *Mg-Al-pv*, calculated by the open system model, assuming perovskite amounts of 76% (red dots) and 85% (blue dots) of the lower mantle mass, in pyrolite and chondrite reference models (Table 1), respectively. Bulk Al_2O_3 contents of pyrolite (A) and chondrite (A1) primitive lower mantle models are shown by red and blue solid lines, respectively. Bulk Al_2O_3 contents of pyrolite-type and chondrite-type non-primitive lower mantle models calculated by adding a 3 wt% of MORB-component (B) are represented by red and blue dotted lines, respectively. MORB composition from Hirose et al. (1999). *P-T* region of 24-80 GPa/1919-2550 K is referred to the chosen geotherm.

Figure 9. Probability (p_o%) of *Mg-Al-pv* occurrence with a given Al_2O_3 mole content *per* formula unit, according to the open system model. Each curve is associated to key *P-T* values (*P* in legend), along the chosen geotherm. The Al_2O_3 contents of natural Al-bearing

perovskite (↔) *claimed* from the lower mantle, are provided by Kaminsky and Lin (2017). In the inset table, the absolute probability to find Al-bearing perovskite (*Mg-Al-Pv*) against Mg-perovskite (*Mg-pv*) is reported for the explored *P*-*T* region of the lower mantle.

Aluminium distribution in an Earth's *non–primitive* lower mantle

Marcello Merli[1], Costanza Bonadiman[2*], Alessandro Pavese[3]

[1] *Department of Earth and Marine Sciences, University of Palermo, Via Archirafi 36, 90123 Palermo, Italy.*

[2] *Department of Physics and Earth Sciences, University of Ferrara, Via Saragat 1, 44122 Ferrara, Italy*

[3] *Department of Earth Sciences, University of Turin, Via Valperga Caluso 32, 10100 Turin, Italy*

[*]Correspondence: Costanza Bonadiman

e-mail: costanza.bonadiman@unife.it

Key-words: Aluminium distribution, Earth's lower mantle; aluminium bearing perovskite; pyrolite, chondrite reference model; MORB-component; enriched lower mantle composition; open system.

ABSTRACT

The aluminium incorporation mechanism of perovskite was explored by means of quantum mechanics in combination with equilibrium/off-equilibrium thermodynamics under the pressure-temperature conditions of the Earth's lower mantle (from 24 to 80 GPa). Earth's lower mantle was modelled as a geochemically "not-primitive" object because of an enrichment by 3 wt% of recycled crustal material (MORB-component). The chemical composition of the "*non primitive*" lower mantle takes into account both chondrite and pyrolite reference models to represent the lower mantle's primitive composition.

The capacity of perovskite to host Al was modelled through an Al_2O_3 exchange process in an unconstrained Mg-perovskite+Mg-Al-perovskite+free-Al_2O_3(corundum) system. Aluminium is *globally* incorporated principally *via* an increase in the amount of Al-bearing perovskite [*Mg-Al-pv*(80 GPa)/*Mg-Al-pv*(24 GPa)≈1.17], rather than by an increase in the Al_2O_3-content of the average chemical composition which changes little (0.11-0.13, mole fraction of Al_2O_3) and tends to decrease in Al. The Al_2O_3 distribution in the lower mantle was described through the probability of the occurrence of given compositions of Al-bearing perovskite. The probability of finding Mg-Al-perovskite is comparable to Al-free Mg-perovskite's. Perovskite with Al_2O_3 mole fraction up to 0.15 has an occurrence probability of ~28% at 24 GPa, increasing up to ~43% at 80 GPa; on the contrary, perovskite compositions in the range 0.19-0.30 Al_2O_3 mole fraction drop their occurrence probability from 9.8 to 2.0%, over the same *P*-range. In light of this, the distribution of Al in the lower mantle shows that, among the possible Al-bearing perovskite phases, the $(Mg_{0.89}Al_{0.11})(Si_{0.89}Al_{0.11})O_3$ composition is the likeliest, providing from 5 to 8% of the bulk perovskite in the pressure range from 24 to 80 GPa. The occurrence of the Al-richest composition, *i.e.* $(Mg_{0.71}Al_{0.29})(Si_{0.71}Al_{0.29})O_3$, is a rare event (probability of occurrence < 1.7%). This study predicts that perovskite may *globally* host Al_2O_3 in terms of 4.3 and 4.8 wt% (with respect to the non-primitive lower mantle mass),

thus accounting for ~ 90% and 100% of the bulk Al_2O_3 estimated in the framework of pyrolite and chondrite reference models, respectively. A calcium-ferrite-type phase (on the $MgAl_2O_4$-$NaAlSiO_4$ join) seems to be the only candidate that can compensate for the 10% gap of the perovskite Al-incorporation capacity, in the case of a pyrolite non-primitive lower mantle model.

1. INTRODUCTION

The mantle is the Earth's largest division by volume, originally marked by a planetary Siderophile/Lithophile element fractionation. Refractory Lithophile Elements (RLE) condensed from a gas of solar nebula composition at the highest temperature (>1400 K at 10^{-4} atm) compatible with the nebula's physical constraints (Lodders, 2003). RLEs' chemical behaviour prevented metal and sulphide phases from entering both chondrites and metallic cores during the planetary differentiation (Lodders, 2003; Kaminski and Javoy, 2013; Mahan et al., 2018). RLEs include Ca and Al among the major elements, the full group of rare earth elements (REE), U and Th. The chemical characteristics of such elements support the primitive Earth's mantle model that preserves the solar ratios of RLEs (Wasson and Kallemeyn, 1988; Lodders et al.,2009; Wang and Jacobsen, 2016).

Aluminium is the sixth most abundant element on Earth: it is a purely refractory lithophile element and its natural abundance is provided by the stable isotope ^{27}Al. The radioactive isotope ^{26}Al quickly decayed in ^{26}Mg (^{26}Al half-life = $7.17 \pm 0.24 \times 10^5$ yr; Norris et al., 1983, Wu and Browne, 1997) during the early stage of the solar system's evolution (Lee et al., 1977; Lodders, 2003; Baker et al., 2012). The ^{26}Al decay provided substantial heating to the proto planetary bodies, and its isotopic daughter is one of the most widely used extinct radioactivity chronometers (Bizzarro, et al., 2005; Spivak-Birndorf et al. 2009; Wimpenny et al., 2019).

Taking into account the geochemical behaviour of aluminium, it is unlikely that a large amount of such element may enter the Earth's core, though it provides a major constituent of many minerals at any depth of the Earth's mantle and crust. Aluminium is also one of the main components of any melt generated from the upper mantle, in terms of 9-21 wt% Al_2O_3 on average (source: PetDB Petrological Database). Melt crystallization, segregation, rise and cooling, led to the formation of the crust over the Earth's history. An intriguing aspect is that

Al, as a crustal component, partially, or entirely, was transported into the mantle, through subduction. Such a process could involve mantle portions well below the magma source regions (Young et al., 2005; Tsuchiya and Tsuchiya, 2008; Wang and Jacobsen, 2016).

Seismic tomography reveals that near the Earth's mantle transition zone, which marks the boundary between upper and lower mantle, repositories of crustal material occur (Christensen and Yuen, 1984; Billen, 2010, King et al., 2015). They exhibit different dynamic behaviours: i) stagnation in the mantle transition zone (Japan trench; Honda, 2017 and references therein); ii) stagnation in the uppermost lower mantle (Peruvian Andes; Fukao and Obayashi 2013); iii) continuous descent, seemingly unhindered, into the lower mantle (Farallon plate, North America; Sigloch et al., 2008). Such tomographic observations suggest a mechanism of global mantle convection with an abundant mass exchange between distinct geochemical reservoirs lying in both the upper and lower mantle (van der Hilst et al., 1997; Nolet et al., 2007).

More recently, geochemical models, aimed at explaining the isotopic evolution of the silicate Earth (Kumari et al., 2016; Jones et al., 2019) or at tracing the distribution of key components (H_2O and Fe-Mg) in the lower mantle (Walter et al., 2015; Merli et al., 2016; 2017), have depicted the Earth's mantle as a chemical reservoir ("pyrolite") involving uninterrupted geochemical reactions and energy/matter flows.

In particular, Kumari et al. (2016) estimated that about 60% of the entire mantle is as depleted in fusible elements (*i.e.* Al and Ca) as its upper portion, whereas the remaining mantle is non-primitive, containing a small fraction of transient and isolated recycled crustal materials.

Jones et al. (2019), combining the geodynamic model of mantle convection with isotope and trace element geochemistry, suggest that the subduction and accumulation of dense oceanic crust produce in the deep mantle a large mass of material enriched in incompatible trace elements. The quoted authors also state that an equivalent of 50-70% of the current continental crust mass was accumulated earlier than 3 Ga ago, and that the crustal recycling and reworking dominated over juvenile additions to the continental crust, since the end of the

Archean (2.5 Ga). This suggests that since the end of the Hadean age (~ 4.6-3.8 Ga) the Earth's lower mantle has been enriched with crustal components.

Understanding the structure and chemical-physical behavior of the slabs subducted into the mantle is out of the scope of the present work. Conversely, we focus on the chemical rearrangement of the main lower mantle mineral phases in the case of a full mixing between crustal slabs and primordial lower mantle. In such a view, aluminium may be an effective "*probe*" among the major elements.

The present work deals with the modelling of Al-incorporation in perovskite, the major phase in the lower mantle, and the resulting Al-distribution, by means of quantum mechanics calculations in combination with equilibrium/off-equilibrium thermodynamics and cluster expansion technique. The cluster expansion approach allows the investigation of large atom clusters, thus providing an effective tool to model solid mixing in a statistical framework (see Merli et al. 2015, and references therein). Because of the complexity of the natural processes, it is convenient to start from a "reference" mineral phase, *i.e.* $MgSiO_3$-perovskite, whose Al-enrichment is investigated. We explore the *P*-range from 24 to 80 GPa, to unquestionably leave the perovskite-to-post perovskite transition aside (Murakami et al., 2004; Tsuchiya and Tsuchiya, 2008; Shim et al., 2008).

Our main goal is to estimate the maximum intrinsic capacity of perovskite to incorporate aluminium and its phase proportion with respect to the Al-free perovskite fraction, as a function of *P*-*T*. Subsequently, the resulting Al-partitioning will be used to discuss the global mechanism of storage of aluminium in the lower mantle.

2. GEOCHEMISTRY

2.1 Lower mantle geochemical model

Cosmochemical arguments supporting a chondritic bulk Earth composition (chondrite reference model) imply that the lower mantle must be enriched in Si with respect to a primitive upper mantle (PUM; Javoy et al., 2010; Murakami et al., 2012; Kaminski, and Javoy 2013), save that the Earth's core should be able to host ~4-6 wt% Si (McDonough 2014, Badro et al., 2014) to balance the Earth's Si-budget against the Sun's and chondrite's [$Mg/Si_{(PUM)}$~1.21-1.31 *versus* $Mg/Si_{(lower\ mantle)}$~1.01]. Conversely, according to petrological data and chondritic constraints the lower mantle is chemically equivalent to the primitive upper mantle (pyrolite reference model; McDonough and Sun,1995; Lyubetskaya and Korenaga, 2007).

Tomographic images of subducted slabs plunging into the deep mantle have been interpreted in terms of an efficient mass transfer between upper and lower mantle domains. This supports large scale mixing and therefore a homogenous Mg/Si distribution (*i.e.* pyrolite) throughout the mantle (Sigloch et al., 2008; van der Hilst et al., 1997). However, only a limited number of slabs actually sink into the lower mantle, given that most of the subducted ones flatten and seem to stagnate at either ~660 km or ~1,000 km depth (Fukao and Obayashi 2013). This points towards a comparatively ineffective mixing process and contrasts the notion of a vigorous global mantle convection. Recently, Ballmer et al. (2017) have hypothesised the presence of stable large-scale high-viscosity bridgmanite-enriched ancient mantle structures (BEAMS) that have been residing in the Earth's lower mantle since the early stage of our planet's formation. Their numerical model also predicts the incorporation of limited amounts of crustal material from shallow to deep mantle, particularly during the early stages. Such crustal portions provide stretched and stirred long-lived "fossil" fragments, in keeping with tomographic observations. Therefore, large-scale heterogeneities may account for the Earth's bulk composition, bringing the lower mantle's Mg/Si ratio closer to the solar-chondritic one unlike the upper mantle.

Hereafter, we shall refer to either the "pyrolite model" (based on the pyrolite composition throughout the mantle) or the "chondrite model" (relying on different compositions between upper and lower mantle) to describe the lower mantle.

Whatever bulk composition model is used to interpret the mantle's dynamics, the crustal components plunging into the lower mantle cause large/small-scale changes of its phase composition (Irifune et al. 1996; McDonough, 2016; Nestola et al., 2018).

2.2 **Enriched (*non-primitive*) lower mantle bulk composition**

Both chondrite and pyrolite lower mantle models are used here to estimate the non-primitive lower mantle compositions. The bulk chemical composition of the lower mantle is generally described in terms of its five major oxides (MgO, FeO, CaO, Al_2O_3 and SiO_2), which account for ~98.5 wt% of the Earth's mantle mass (Mc Donough, 2016; Palme and O'Neill, 2014). Na_2O occurrence, even if of modest impact on the large-scale geophysical and geochemical modelling (Bina and Helffrich, 2014; Palme and O'Neill, 2014 Chust et al., 2017), is still important in terms of the resulting minor mineral phases that affect the Al distribution in the lower mantle. Experiments and observations on natural samples reveal that potential Al-bearing lower mantle phases may also include K, Fe^{3+} and OH as major elements (*i.e.*: Kato et al., 2013; Wang et al., 2015; Pamato et al., 2015; Harte and Richardson, 2012). In particular, Al-bearing phases are able to host potassium if they form in a system containing at least ~ 0.09 wt% K_2O (Kato et al., 2013). Note that the mid-ocean-ridge basalt (MORB) average composition has 0.08-0.12 wt% K_2O (Gale et al., 2013), whereas pyrolite and chondrite lower mantle models are estimated to bear ~0.03 and <0.01 wt% K_2O, respectively (McDonough and Sun, 1995; Javoy et al., 2010). Therefore, K-bearing phases are not expected to play a relevant role as potential aluminium hosts among the lower mantle phases. Although ferric iron is able to affect Al^{3+} storage in perovskite-like structures *via* $Fe^{3+}\leftrightarrow Al^{3+}$ replacement

(Kurnosov et al., 2017), the $Fe^{3+}/\sum Fe_{tot}$ ratio in the primitive Earth's mantle is supposed to be very small, *i.e.* ~0.03, according to mass balance calculations (Palme and O'Neill, 2014). Bulk H_2O (hosted as OH-group) in the lower mantle influences the aluminium content incorporated by perovskite through the formation of Al-bearing hydrous phases. However, the bulk H_2O content is comparatively modest and estimated ~1500 ppm, in both pyrolite and chondrite lower mantle models (Merli et al., 2016; Muir and Brodholt, 2018).

Let us consider the lower mantle as a geochemically non-primitive object because it is mixed with a fraction of recycled crustal material (*i.e.* MORB-component). In this view, Al_2O_3 and CaO, hosted in lower mantle minerals, are potential "*probes*" which mark the occurrence of such a geodynamic process (Guignot and Andrault, 2004, Hirose et al., 2005; Korenaga, 2009; Irifune et al., 2010; Ricolleau et al., 2010).

The MORB chemical composition is enriched in incompatible major elements (aluminium, calcium and, to a lesser extent, iron) and depleted of compatible elements (magnesium) with respect to the mantle (Table 1). Therefore, a MORB-like composition at lower mantle *P-T* conditions cannot give Fe-periclase, whereas high-pressure SiO_2-rich phases (*e.g.* Ca-perovskite and bridgmanite) and additional aluminium-rich phases are expected to occur. Following experimental results about MORB bulk compositions (14-16 wt% Al_2O_3) under lower mantle conditions (30-90 GPa), the newly formed Al_2O_3-rich phases (NAL-type phase and $CaFe_2O_4$-type phase, *i.e.* CF-phase, on the join $MgAl_2O_4$-$NaAlSiO_4$) may account for about 10-12 mol% by phase composition (Guignot and Andrault, 2004, Ricolleau et al., 2010).

Assuming that subducted crustal fragments have been sliding down into the mantle over the past 4 billion years (the most generous estimate is about 11 wt% of the whole mantle; Li and McNamara, 2013), aluminium-rich domains should have developed, in contrast to expectations from a primitive lower mantle's composition (Stixrude and Lithgow-Bertelloni, 2012).

We model such an enrichment using the simple binary mixing equation of Faure (1986) to combine primitive lower mantle compositions (pyrolite and chondrite, corresponding to the end-members "A" and "A1", respectively; see Table 1) with a crust-type-composition (end-member "B"; MORB-like silicate glass; see Table 1). End-member B is close to the N-MORB average of Gale et al. (2013) and has been largely used in H*P* experiments (*i.e.* Hirose et al., 1999; 2005 Funamori et al., 2000; Guignot and Andrault, 2004; Ricolleau et al., 2010). According to the extensive compilation provided by the PetDB-database of chemical data from mid-ocean ridge basalts, the water concentrations lie in the range 0.05-1.0 wt%. The amount of H_2O stored in the deep mantle, computed by experiments and mass balance models (Ghosh et al., 2014; Marty, 2012), is in the range 800-2700 ppm (*i.e.* 0.08-0.27 wt%). Taking into account such figures and the tomographic observations that suggest that only small fractions of descending slabs reach the lower mantle (Ballmer et al. 2017), we model a non-primitive lower mantle composition by a chemical mixing of primitive pyrolite/chondrite compositions with a 3 wt% end-member B's contribution (0.1 wt% of H_2O). The resulting compositions are reported in Table 1. Such chemical mixing ideally reproduces a non-primitive lower mantle as predicted by modelling the isotopic evolution of the silicate Earth: ~3 wt% of the total mantle mass is expected to be stored and ultimately mixed within ~1 Ga in the lower mantle (Christensen and Hofmann 1994; Kumari et al., 2016; White, 2015).

3. METHODS

3.1 Chemical probability of formation: aluminium-bearing phases in the lower mantle

The probability that a phase "J" forms at *P-T*, *i.e.* $p(J|P,T)$, can be roughly estimated in terms of $p(J|P,T) \propto p(J,chem) \times \exp(-\Delta G(P,T)_{formation}/RT)$, where $p(J,chem)$ is the probability of having the required chemical species for J under the constraint of a given available elemental budget

and $\Delta G(P,T)_{\text{formation}}$ is the formation Gibbs energy. p(J,chem) is termed "*chemical probability of formation*", to underline that it reflects the likelihood of having the required elements to form the J-phase, and it is calculated as follows.

Let us assume X_k to represent the fractional abundance value of the k^{th}-oxide, in a generic system. Given that

$$\sum_{k=1,\mathrm{M}} X_k = 1 \qquad (1)$$

then X_k can also be associated with the *probability* of having the k^{th}-oxide, if the oxides are supposed to be uniformly distributed as a function of space. The chemical composition of the J-phase is then expressed formally as

$$\mathrm{J} = \sum_k n_k X_k \qquad (2)$$

Therefore, the probability of finding one mole of the J-phase as a function of its pure chemical composition, p(J,chem), is provided by the joint events of i) having (n_1-moles of X_1)(n_2-moles of X_2)…. and ii) not having any species with stoichiometric coefficient equal to 0. This corresponds to the following joint probability:

$$p(\mathrm{J},\mathrm{chem}) \propto \prod_k p(k)^{n_k} \times (1 - \sum_m p(m)) \propto \prod_j X_j^{n_j} \times (1 - \sum_m X_m) \qquad (3)$$

where $p(k)$ and $p(m)$ are the probabilities of finding the k^{th} and m^{th} oxide, respectively; the subscript k is associated with the chemical species with stoichiometric coefficients other than zero, whereas m is related to those with stoichiometric coefficients equal to zero. The p(J,chem) values calculated in this way are then normalized so that their sum yields unity.

Table 2 reports major phases and potential Al-bearing phases that experiments, numerical modelling and exceptional observations on natural findings indicated as possible minerals in a non-primitive lower mantle (Table 1).

Preliminary calculations led us to rule out periclase as a host of aluminium, save that the Al-incorporation takes place with the contribution of H (Merli et al., 2016). In such a case, the amount of Al involved would be negligible, anyway. Panero et al. (2006) estimated regular solution parameters of 12 and 66 kJ/mol for perovskite and akimotoite, respectively. Taking

255 into account i) the significantly lower energy for Al-incorporation in perovskite than in
256 akimotoite and ii) the restricted range of occurrence of the latter (Panero et al., 2006), we
257 exclude akimotoite as a possible competitor to uptake Al in the *P-T* region under investigation
258 (Stebbins et al., 2001; Li et al. 2008; Tschauner et al., 2018). Majorite garnet, which is the
259 main host of aluminium in the mantle transition region in both pyrolite and basaltic
260 compositions (Irifune and Ringwood, 1993; Litasov and Ohtani, 2007), is transformed into
261 Mg-perovskite+Ca-perovskite at pressures corresponding to the uppermost lower mantle.
262 Experiments show that aluminium is mostly incorporated by Mg-perovskite/bridgmanite in
263 pyrolite or chondrite compositions under lower mantle *P-T* conditions (Irifune et al.,1996;
264 Ricolleau t al., 2008), whereas separate aluminous phases form in basaltic compositions
265 (Hirose et a.,1999; 2005) at the same *P-T* conditions.
266 In a non-primitive lower mantle, aluminium is partitioned between perovskite/bridgmanite
267 and minor Al-bearing phases, such as:
268 i) alkali rich NAL-structure phases, like those on the join $NaMg_2Al_{4.8}Si_{1.15}O_{12}$-
269 $KMg_2Al_{4.8}Si_{1.15}O_{12}$ (Gasparik et al., 2000; Kato et al., 2013; Wu et al., 2016). However, as
270 stated above, K-bearing phases are unlikely to develop in the lower mantle because of the lack
271 of a sufficient amount of potassium;
272 ii) CF-structure and NAL-structure polymorphs, on the join $MgAl_2O_4$-$NaAlSiO_4$ (Imada et al.,
273 2011; 2012; Irifune et al., 1991). Note that the CF-structure was observed to stabilize at a
274 higher pressure (~ >40 GPa) than the NAL-structure (~ 24-40 GPa) (Imada et al., 2011;
275 Guignot and Andrault, 2004);
276 iii) possible hydrous solid solutions involving D-phase, H-phase and δ-AlOOH (Ghosh and
277 Schmidt, 2014; Pamato et al., 2015; Walter et al., 2015; Fukuyama et al., 2017).
278 In the case of NAL- and CF-phases, we chose to calculate a *chemical probability of formation*
279 p(J,chem) for a reference NAL/CF-mineral, that is $Na_{0.265}Fe_{0.245}Mg_{0.375}Ca_{0.035}Al_{1.1}Si_{0.715}O_4$.
280 Such a composition is obtained from Guignot and Andrault (2004), by averaging those that

281 the authors labelled with "CF^{A}" and "CF^{B1}", neglecting Ti and normalizing to 4 oxygen atoms
282 and 3 cations.
283 Hereafter we shall use the following acronyms, for the sake of brevity: *Mg-pv*, "Mg-
284 perovskite", for perovskite tout court, *i.e.* MgSiO3; *Mg-Al-pv*, "Al-perovskite", for Al bearing
285 Mg-perovskite, *i.e.* (Mg,Al)(Si,Al)O_3; *Mg-Fe-pv*, "bridgmanite", for Fe-bearing Mg-
286 perovskite, *i.e.* (Mg,Fe)SiO_3; *Ca-pv*, "Ca-perovskite", for Ca-bearing perovskite, *i.e.*
287 (Ca,Mg)SiO_3; "perovskite", for any solid mixing, or end member, occurring in the lower
288 mantle and having perovskite-type structure; *Fe-pe*, "Fe-periclase", *i.e.* (Mg,Fe)O; *CF*, "CF-
289 phase", for a phase in the $MgAl_2O_4$-$NaAlSiO_4$ join.
290
291 **3.2 Aluminium incorporation mechanisms of perovskite**
292
293 To evaluate the aluminium distribution in a non-primitive lower mantle, we model the Al-
294 uptake capacity of perovskite, which is the lower mantle phase able to host aluminium to such
295 an extent as to provide a relevant storage by volume (Jeanloz and Knittle, 1989; Ricolleau et
296 al.,2009).
297 We introduce the notion of "maximum Al-uptake capacity" of perovskite. "Maximum Al-
298 uptake capacity"-conditions are set through a *virtual* competition between $MgSiO_3$ and Al_2O_3
299 (ideal *pure* alumina phase) to accommodate Al, at lower mantle *P-T* conditions and in a SiO_2-
300 MgO-Al_2O_3 system. Corundum (*cor*) is the least "prejudicial" phase as an Al-host, given that
301 it does not require any further chemical species but aluminium to form and is the Al_2O_3-
302 polymorph stable in the *P-T* range of interest (Merli and Pavese 2018).
303 The incorporation mechanism of a trivalent cation in perovskite is supposed to occur through
304 three main reactions (Navrotsky et al., 2003; Akber-Knutson et al., 2005 and references
305 therein):
306 (i) $Si^{4+} + Mg^{2+} = M^{3+} + M^{3+}$

307 (ii) $Si^{4+} = M^{3+} + 1/2\ V^{0}_{O}$

308 (iii) $Si^{4+} = M^{3+} + H^{+}$.

309 Reaction (i), which takes place *via* a charge-coupled-mechanism, is the likeliest one, as shown
310 by energy calculations (Yamamoto et al., 2003; Akber-Knutson et al., 2005; Zhang and
311 Oganov, 2006). A comparison between incorporation mechanisms (i) and (ii) reveals that the
312 former is slightly exothermic, in contrast with the endothermic behaviour of the latter
313 (Navrotsky et al., 2003). NMR-measurements point to the occurrence of a charge-coupled
314 mechanism (Stebbins et al., 2001), in agreement with calculations of Akber-Knutson and
315 Bukowinski (2004), who suggest that Al tends to replace both Si and M^{2+}, in a high pressure
316 and high temperature regime. As to reaction (iii), we assume contents of H_2O, *i.e.* H^+ supplier,
317 and Al_2O_3 as much as 1500 ppm (0.15 wt%) and 4.76 wt%, respectively (Table 1), in keeping
318 with the lower mantle Al-richest composition obtained by mixing pyrolite with 3% MORB-
319 component (Table 1). In such a case, even if all the hydrogen from the dissociation
320 $OH_2 \rightarrow OH^- + H^+$ contributed to an exchange mechanism like (iii), just 0.08 mol fraction
321 aluminium might be accounted for. Moreover, according to the H_2O-partitioning estimated by
322 Merli et al. (2016), periclase is able to account for 1/3 of the trapped H_2O, thus reducing
323 further the role of reaction (iii) as a possible relevant mechanism to Al-incorporation in
324 perovskite.

325 Therefore, the Al-uptake in perovskite is modelled by the replacement of Mg-Si with Al-Al,
326 according to the exchange reaction reported below using the formalism of Kröger-Vink
327 (Kröger, 1972)

328 $$Al_2O_3 + [Mg_{Mg}]^X + [Si_{Si}]^X \leftrightarrow [Al_{Mg}]^{\bullet} + [Al_{Si}]' + MgSiO_3. \quad (4)$$

329 Assuming λ-mole of Al_2O_3 to be exchanged in the *Mg-Al-pv*, *Mg-pv* and *cor* system, then
330 equ.(4) leads to

331 $$(1-\lambda)MgSiO_3 + \lambda\ Al_2O_3 \Leftrightarrow (Mg_{1-\lambda}Al_{\lambda})(Si_{1-\lambda}Al_{\lambda})O_3. \quad (5)$$

In reaction (5) iron can affect the energy through a replacement like $Mg^{2+} \Leftrightarrow Fe^{2+}$ and competes with aluminium in terms of $Al^{3+} \Leftrightarrow Fe^{3+}$. However, we chose to neglect Fe as we are developing a first approximation model, which would provide general trends rather than details. Our choice can be further supported by the following arguments.

- The general reaction that accounts for Al_2O_3 entering in bridgmanite turns out to be

$$(Mg_{1-x}Fe_x^{2+})SiO_3 + \lambda Al_2O_3 = \left(Mg_{1-x-\lambda/2}Fe_{x-\lambda/2}^{2+}Al_\lambda\right)(Si_{1-\lambda}Al_\lambda)O_3 + \lambda\,(Mg_{\frac{1}{2}}Fe_{\frac{1}{2}}^{2+})SiO_3 \quad (6)$$

where we assume that Al replaces the same quantity of Mg and Fe^{2+}, the latter dwelling at the 12-coordination site, only (Kaminsky and Lin, 2017). The parametrization of the Gibbs energy used in the present work relies upon the cluster expansion technique (Merli et al., 2015; 2017). Such a method leads to expressing energy as a function of the number of interacting atomic pairs that belong to the same cluster determined as a function of the distance between the involved chemical species. Assuming Fe-Al pair entering the perovskite structure as much as 0.1-0.2 moles (*i.e.* Kurnosov et al., 2017; Kaminsky and Lin, 2017), the probability of having a Fe-Al interacting pair belonging to the first/second cluster is ~5-6 %. Therefore, most of the interactions with aluminium atoms are due to the pure Mg-Si matrix, which governs the "maximum intrinsic capacity" of perovskite to incorporate Al.

The role of Fe^{3+} is extensively debated and still largely uncertain. *Mg-Fe-pv* is potentially the major Fe^{3+} acceptor, but Kaminsky and Lin (2017) indicated that in natural lower mantle bridgmanites iron most likely occurs as ferrous at the 12-coordination sites. Conversely, Kurnosov et al. (2017) claim $Fe^{3+}/\Sigma Fe_{tot} = 0.33$, in synthetic bridgmanite with ferric iron sited at the same coordination site, under lower mantle conditions (P~ 35 GPa; 1300 km depth; Ismailova et al. 2016). Mass balance calculations, in turn, predict an impact of ferric iron in terms of $Fe^{3+}/\sum Fe_{tot}$~0.03, with

respect to the Earth's mantle abundances (Palme and O'Neill, 2014). If we consider as a first level of approximation pyrolite (*Mg-Fe-pv* =76 wt%; FeO_{tot} = 8.05 wt%) and chondrite (*Mg-Fe-pv* =85 wt%; FeO_{tot} = 8.12 wt%) lower mantle models (Table 1), and apply the Kurnosov et al. (2017) Fe^{3+}/Fe_{tot} ratio to *Mg-Fe-pv*, the resulting Al^{3+}/Fe^{3+} mole ratios in bridgmanite are ~3.6 and ~2.9 for pyrolite and chondrite models, respectively. Tests based on calculations that we carried out to reproduce the replacement schemes Si + Mg ⇔ Al + Fe^{3+} *versus* Si + Mg ⇔ Al + Al, indicate that the second reaction is favoured over the former one [in agreement with the results of Nishio-Hamane et al. (2005)].

3.3 Reaction models

The Al-uptake mechanism in perovskite according to reaction (5) is addressed using two approaches: i) the *open system model*, which exploits the notion of stationary thermodynamic state and allows an exchange of matter between system and reservoir (Prigogine 1968); ii) the *closed system model*, which relies on equilibrium thermodynamics, therefore excluding any sort of matter exchange. In an open system, the stationary state replaces the equilibrium state and exhibits thermodynamic observables, which remain invariant over time. Details about the open system model are reported in APPENDIX I.1-.2-.3 and a brief overview is given below.

3.3.1 Open system model

We would like to exploit the capacity of an open system to exchange matter with a reservoir, in combination with a formalism as close as possible to the consolidated equilibrium thermodynamics' one. Such a model provides a flexible tool to address problems in which the intrinsic exchanging/incorporation capacity of a given substance can be investigated, without any sort of constraint or restraint (APPENDIX I.1).

The key requirement is the fulfilment of the following equation, associated to reaction (5) *via* the equilibrium constant K (APPENDIX I.2-3):

$$K(P,T,\lambda) = exp[-\Delta G_0(P,T,\lambda)/\mathrm{R}T] = a_{Mg-Al-pv}/\left(a_{Mg-pv}^{1-\lambda} \times a_{cor}^{\lambda}\right) \approx x_{Mg-Al-pv}/\left(x_{Mg-pv}^{1-\lambda} \times x_{cor}^{\lambda}\right) \quad (7.a)$$

where x_j=phase proportion of the jth-component/phase (*cor*: corundum); a_j=jth-component/phase's activity. In equ.(7.a) the activity coefficient is approximated to unity (see APPENDIX I.3 and APPENDIX II). Expanding ΔG_0, it follows that:

$$\Delta G_0(P,T,\lambda) = \mu_0(P,T,\lambda)_{Mg-Al-pv} - \lambda \times \left[\mu_0(P,T)_{cor} - \mu_0(P,T)_{Mg-pv}\right] - \mu_0(P,T)_{Mg-pv}. \quad (7.b)$$

where μ_0 is the part of the chemical potential depending on λ, P and T, only (Ottonello 1997; 2010). For convenience, we split the chemical potential of Al-incorporating perovskite (*Mg-Al-pv*) into an Al-free part, *i.e*. pure perovskite (*Mg-pv*), and a part dependent on aluminium, that is

$$\mu_0(P,T,\lambda)_{Mg-Al-pv} = \mu_0(P,T)_{Mg-pv} + \Delta\mu_0(P,T,\lambda)_{Mg-Al-pv}, \quad (7.c)$$

where $\Delta\mu_0(P,T,\lambda)_{Mg\text{-}Al\text{-}pv}$, which accounts for the solid mixing occurrence and provides the very core of our computational model, is calculated by the cluster expansion method (Merli et al 2015, 2017).

Using equ.(7.c), equ.(7.b) becomes

$$\Delta G_0(P,T,\lambda) = \Delta\mu_0(P,T,\lambda)_{Mg-Al-pv} - \lambda\left[\mu_0(P,T)_{cor} - \mu_0(P,T)_{Mg-pv}\right]. \quad (8)$$

At given (P,T,λ)-values, we seek the {$x_{Mg\text{-}Al\text{-}pv}$, $x_{Mg\text{-}pv}$, x_{cor}}-sets that fulfil

a) equ.(7.a),

b) $x_{Mg\text{-}Al\text{-}pv}$, $x_{Mg\text{-}pv}$, $x_{cor} \geq 0$,

c) $x_{Mg\text{-}Al\text{-}pv} + x_{Mg\text{-}pv} + x_{cor} = 1$.

Among the solutions that satisfy the constraints a), b) and c), we chose the one that minimizes the Gibbs energy, namely $x_{Mg\text{-}Al\text{-}pv} \times \mu_0(P,T,\lambda)_{Mg\text{-}Al\text{-}pv} + x_{Mg\text{-}pv} \times \mu_0(P,T)_{Mg\text{-}pv} + x_{cor} \times \mu_0(P,T)_{cor}$. In

doing so, we obtain a triple, yielding *Mg-Al-pv*/*Mg-pv*/*cor* phase proportions, for each (P,T,λ) point, *i.e.* $\{x_{Mg\text{-}Al\text{-}pv}, x_{Mg\text{-}pv}, x_{cor}\}(P,T,\lambda)$. The preservation of the total chemical composition of the system constituted by each $\{x_{Mg\text{-}Al\text{-}pv}, x_{Mg\text{-}pv}, x_{cor}\}(P,T,\lambda)$-triple is not required. The resulting system therefore behaves as an open system that can exchange 2Al $\Leftrightarrow$ Mg+Si with a reservoir. In general, we are interested in modelling *observables* whose values are averages over the λ-range, so that they depend ultimately on P-T only. For instance:

$$\{x_{Mg-Al-pv}, x_{Mg-pv}, x_{cor}\}(P,T) = \frac{1}{C}\int_{\lambda-inf}^{\lambda-sup}\{x_{Mg-Al-pv}, x_{Mg-pv}, x_{cor}\}(P,T,\lambda)\,\mathrm{d}\lambda \qquad (9.\mathrm{a})$$

$$\lambda_{Al2O3}(P,T) = \int_{\lambda-inf}^{\lambda-sup}\lambda \times x_{Mg-Al-pv}(P,T,\lambda)\,\mathrm{d}\lambda / x_{Mg-Al-pv}(P,T) \qquad (9.\mathrm{b})$$

$$Tot_{Al2O3}(P,T) = \frac{1}{C}\int_{\lambda-inf}^{\lambda-sup}\left[\lambda \times x_{Mg-Al-pv}(P,T,\lambda) + x_{Al2O3}(P,T,\lambda)\right]\mathrm{d}\lambda \qquad (9.\mathrm{c})$$

where: C is a normalization constant; λ-sup=0.3 and λ-inf=0, upper and lower thresholds of λ, respectively (for λ>0.3, $x_{Mg\text{-}Al\text{-}pv}$ is negligible on the P-T range explored); λ_{Al2O3} of (9.b) is the *average* Al_2O_3 mole fraction *per* formula unit; Tot_{Al2O3} is the total Al_2O_3 stored by the (*Mg-Al-pv*)+(*Mg-pv*)+*cor* system.

3.3.2 Closed system model

For the sake of completeness, we also present the closed system model. We seek the equilibrium conditions of reaction (5) for a closed system, *i.e.* a chemically adiabatic one. Let ξ represent the aluminium occupancy factor in *Mg-Al-pv* [*i.e.* $(Mg_{1-\xi}Al_{\xi})(Si_{1-\xi}Al_{\xi})O_3$]. Therefore, we have to minimize, with respect to ξ, the Gibbs energy of the system (*Mg-pv*)+(*Mg-Al-pv*)+*cor*, *i.e.*

$$G = n_{cor} \times \mu_0(P,T)_{cor} + n_{pv} \times \mu_0(P,T)_{Mg-pv} + n_{Mg-Al-pv} \times \mu_0(P,T,\xi)_{Mg-Al-pv}, \qquad (10)$$

under the constraints of the conservation of mass:

$$M_{Al2O3} = n_{cor} + n_{Mg\text{-}Al\text{-}pv} \times \xi \qquad (11)$$

$$M = M_{SiO2} = M_{MgO} = n_{Mg\text{-}pv} + n_{Mg\text{-}Al\text{-}pv} \times (1-\xi), \qquad (12)$$

where M_{Al2O3}, M_{SiO2} and M_{MgO} are *fixed* total amounts in moles of Al_2O_3, SiO_2 and MgO.

Using the constraints above, equ.(10) becomes

$$G = \left(M_{Al2O3} - n_{Mg-Al-pv} \times \xi\right) \times \mu_0(P,T)_{cor} + \left(M - n_{Mg-Al-pv} \times (1-\xi)\right) \times \mu_0(P,T)_{Mg-pv} + n_{Mg-Al-pv} \times \mu_0(P,T,\xi)_{Mg-Al-pv}. \quad (13)$$

The Gibbs energy minimum condition requires

$$\frac{\partial G}{\partial \xi} = 0,$$

from which the following equation is derived

$$-\mu_0(P,T)_{cor} + \mu_0(P,T)_{Mg-pv} + \frac{\partial \mu_0(P,T,\xi)_{Mg-Al-pv}}{\partial \xi} = 0. \quad (14)$$

Equ.(14) formalises the equilibrium conditions for closed systems (Chust et al. 2017). Its solution, expressed by $\xi_{\text{closed system}}$, yields the composition of Al-bearing perovskite that minimises the Gibbs energy of equ.(13).

$\xi_{\text{closed system}}$ also minimises (7.b). In fact, taking into account equ.(7.c), equ.(14) is equivalent to setting $\frac{\partial \Delta G_0(P,T,\lambda)}{\partial \lambda} = 0$ in equ.(8), which implies that $K(P,T,\xi_{\text{closed system}})$ achieves an extreme value that shifts reaction (5) towards its right-hand side member as much as possible.

3.4 Computational

Structure relaxations were performed at a given pressure and 0 K by the HF/DFT-CRYSTAL14 program (Dovesi el al., 2009), which implements "A*b-initio* Linear-Combination-of-Atomic-Orbitals" for periodic systems. Only static pressure (P_{static}=-$\partial E_{\text{static energy}}/\partial V$) and zero-point pressure (P_{zp}==-$\partial E_{\text{vibration energy at 0K}}/\partial V$) were taken into account, given that even adding a correction for thermal contributions would not significantly change our results and the conclusions would be unaffected. A zero-point pressure was estimated by quantum mechanics calculations and using *pure perovskite* only, resulting in ~5 GPa. The

WCGGA functional (Wu and Cohen, 2006) was used, with a hybridization rate of 28%. Such a proportion was adopted because it provides a more satisfactory agreement with observations in terms of perovskite structure, than other choices do. The tolerances governing the accuracy of the integrals of the self-consistent-field-cycles were set at (in Ha units): 10^{-8} for coulomb overlap, 10^{-8} for coulomb penetration, 10^{-8} for exchange overlap, 10^{-8} for exchange pseudo-overlap in direct space, 10^{-16} for exchange pseudo-overlap in reciprocal space and 10^{-9} for threshold for SCF-cycles' convergence. The Mg basis set from Causà et al. (1986) was extended by the addition of diffuse *sp* and *d* shells (85-11G* contraction). Oxygen and aluminium were modelled by means of the O8-411d1 and 85-11G* basis sets of Corà (2005) and Catti et al. (1994), respectively. The outer shells' coefficients were optimised by means of the "billy" utility by Towler (2015). The eigenvalue level shifting technique was used (level shift of 0.2 Ha) to avoid conducting solutions and accelerate convergence.

The approach of Merli et al. (2015 and 2017) relying upon the cluster expansion technique was adopted to model the solid mixing in *Mg-Al-pv*. Such a method makes it possible to parametrize energy as a function of pair interactions, thus allowing one to model in a statistical framework even large atom clusters that would be difficult to handle otherwise. We expressed the Al-dependent part of the chemical potentials in equ.(7.b) as

$$\Delta\mu_0(P,T,\lambda)_{Mg-Al-pv} = \mu_0(P,T,\lambda)_{Mg-Al-pv} - \mu_0(P,T)_{pv} = \lambda \times [\mu_0(P,T,\lambda)_{Mg-Al-pv} - \mu_0(P,T)_{cor}] + \delta\mu_0(P,T,\lambda)_{Mg-Al-pv}. \quad (15)$$

$\delta\mu_0(P,T,\lambda)$, in turn, was developed in terms of

$$\delta\mu_0(P,T,\lambda)_{Mg-Al-pv} = (1-\lambda) \times \lambda \times \sum_{l=0,L;m=0,M;n=0,N} p_{lmn} P^l T^m \lambda^n. \quad (16)$$

We used perovskite's supercells, composed of (2×2×1), (2×1×2) and (1×2×2) elementary cells. A total of 80 independent Al-configurations were randomly sampled over the interval 24-80 GPa and used to calculate the pair-interaction parameters of the cluster expansion as a function of *P*, following the strategy of Merli et al. (2017). We then simulated 10^5-10^6 *Mg-Al-*

pv independent configurations in 1024 atom clusters, using the pair-interaction parameters previously determined, to carry out statistical thermodynamics calculations (Merli et al. 2015), and model the Gibbs energy of Al-bearing perovskite thereby.

ΔG_0 in equ.(7.b) were calculated neglecting the atomic vibration contribution, *i.e.* the one including zero-point vibration energy, thermal vibration energy and vibration entropy (in full: $\Delta G_{0,vib}$). In general, calculating $\Delta G_{0,vib}$ in a solid mixing that is modelled *via* a super-cell method is a difficult task, because of the complexity of compromising between representativeness of a cluster, computing time and achievable precision (about the role of vibrational components, see: van de Walle and Ceder, 2002). However, combining quantum calculations with semi-empirical potentials (GULP code; Gale 1997; 2005), which allow the investigation of large atomic clusters' lattice dynamics, we estimated, by harmonic approximation, $\Delta G_{0,vib}$ for 4 Al-Al configurations in perovskite at 20 and 70 GPa, with 0.25 Al_2O_3 mole fraction. In this way we compared $\Delta G_{0,vib}$ with $\Delta G_{0,stat+conf}$, *i.e.* the static contribution with the addition of configuration entropy, which we actually calculated. We observed $|\Delta G_{0,vib}/\Delta G_{0,stat+conf}|$~3%, in the thermal range of interest, *i.e.* 2000-3000 K. Therefore, taking into account the modest estimated weight of the thermal contribution in the solid mixing, we chose to leave it aside (as for neglecting vibration contribution, see for instance: Mohn and Trønnes 2016; Burton and van de Walle, 2003).

4. RESULTS

4.1 Chemical probability of formation of lower mantle phases

The bulk aluminium content (largest value: 4.76 wt%, related to pyrolite lower mantle mixed with 3% of crustal component; Table 1) and the available amounts of alkali elements and H_2O make the *chemical probability of formation* [*p*(J,chem)] for the minor Al-bearing phases <

505 0.9% with respect to the total phases formed under the constraint of a non-primitive lower
506 mantle composition (Table 1; Table 2). As expected, the *p*(J,chem) of *Mg-Fe-pv+Mg-pv+Ca-*
507 *pv+Fe-pe* in a non-primitive lower mantle is >78%, regardless of the geochemical model
508 used. It is worth noting that *p*(J,chem) of *Mg-Al-pv* is as large as ~96%, considering the Al-
509 bearing phases only (Table 3). The hydrous phases are *quasi* irrelevant, whereas the NAL/CF-
510 type phase exhibits a *p*(J,chem) as large as 3.87-3.57% (Table 3).
511 If we used *p*(J,chem) as an "actual" *probability of finding a given phase*, then Al would
512 distribute in terms of 4/5 *versus* 1/5 between *Mg-Al-pv* and *CF* (the CF-phase is able to host
513 almost six times as much aluminium as perovskite). This estimate is to be taken with due care
514 as *p*(*Mg-Al-pv*,chem) and *p*(*CF*,chem) quantify only the probability of having the "least
515 condition" for a given phase to form, regardless of the energy contribution and inter-phase
516 competition to capture the involved elements. Altogether, perovskite is the main candidate to
517 incorporate aluminium by far, though *CF*, too, exhibits a potential capacity for Al-storing.
518
519 **4.2 Al-uptake in perovskite: open system model *versus* closed system model**
520
521 The main advantages of using an *open system model* with respect to a *closed system model* are
522 the following:
523 -neglecting the chemical composition invariance allows the system to evolve *unconstrained*,
524 driven by the mixing Gibbs energy of the solid solution of *Mg-Al-pv*. This provides the most
525 favourable condition to estimate the *Mg-Al-pv*'s intrinsic maximum capacity to host Al,
526 resorting to a simple system composed of perovskite in combination with free-alumina (*cor*),
527 the latter accounting for the aluminium not incorporated by the former because of saturation;
528 -such a method makes it possible i) to achieve an average depiction of the output of a given
529 chemical process and ii) to explore a mechanism of Al-storage taking into account not only

the Al-occupancy in perovskite, but also the amount of perovskite that is able to host aluminium *versus* the fraction of Al-free perovskite (*Mg-Al-pv*/*Mg-pv*).

Reaction (5) was investigated using the *P*-*T* curve parametrised by Merli et al. (2016) as follows

T(K) = 11.290 × P (GPa) +1648,

for 24< P < 80 (GPa). Such a curve represents a lower mantle in a whole mantle convention of limited thermal efficiency (Mattern et al., 2005; Stixrude and Lithgrow-Bertelloni, 2005), thus approaching the layered mantle convection models (Brown and Shankland, 1981; Anderson, 1982 ; Valencia-Cardona et al., 2017).

4.2.1 Al-uptake in perovskite from open system model

Figure 1 shows $K(P,T,\lambda)$ of equ. (7.a) as a function of λ, at three chosen *P*-*T* points. In general, the larger the value of *K*, the more reaction (5) shifts to the right, *i.e*. towards *Mg-Al-pv*. For each *P*-*T* point, $K(P,T,\lambda)$ has a maximum that changes from about 0.17 (24 GPa/1919 K) to 0.26 (80 GPa/2551 K). This means that there is an Al-exchange λ-value that maximises the tendency to promote *Mg-Al-pv* at each *P*-*T* point of the geotherm. We now introduce the function $K(P,T)_{ave}$, which corresponds to the average of the equilibrium constant of reaction (5), *i.e*. $K(P,T)_{ave}=<K(P,T,\lambda)>_{\lambda}$. $K(P,T)_{ave}$ provides an overview of the general tendency of the aluminium incorporation process to shift either to the right or left in reaction (5) along the chosen *P*-*T* path (Fig. 2). $K(P,T)_{ave}$ calculated over Al-exchange processes between corundum and perovskite from 0 to 0.3 λ-value, tends to increase upon increasing *P*, *i.e*. reaction (5) shifts more and more to its right-hand side member $[(Mg_{1-\lambda}Al_{\lambda})(Si_{1-\lambda}Al_{\lambda})O_3]$. Two trends of $K(P,T)_{ave}$ are observable: one below and one above ~60 GPa, characterised by 0.008 and 0.02 GPa^{-1} slopes, respectively (Fig. 2). They are reflective of the growing differences between the $K(P,T,\lambda)$-curves, for λ > 0.15 (Fig. 1). On the explored *P*-*T* interval, the content of free-Al_2O_3,

555 *i.e. cor*, takes a very small average figure of 0.0010(±1), in terms of phase proportion.
556 Conversely, Al-free (*Mg-pv*) and Al-bearing (*Mg-Al-pv)* perovskite phases amount to
557 0.56(±2) and 0.44(±2), respectively (Fig. 3). *Mg-Al-pv* increases from 0.41 to 0.48 phase
558 proportion, from 24 to 80 GPa: this hints at a tendency to develop more and more
559 (Mg,Al)(Si,Al)O_3-phase upon *P* (Fig. 3).
560 The *cor/Mg-Al-pv* ratio monotonically decreases with increasing pressure up to 70 GPa (Fig.
561 4), from more than 0.022 to about 0.017, meaning that some 98 wt% of available Al_2O_3 is
562 taken by perovskite, in agreement with the results shown in Figures 1-3. In the range 60-80
563 GPa the data are rather scattered and weakly *P*-dependent. They indicate either some sort of
564 "saturation" (with respect to perovskite) or a poorly defined minimum. The aluminium uptake
565 capacity of perovskite is described *via* λ_{Al2O3}, see equ.(9.b), that gives the average Al_2O_3 mole
566 fraction *per* formula unit (Fig. 5). At 32 GPa perovskite hosts Al_2O_3 at its maximum capacity
567 (λ_{Al2O3}= 0.134 Al_2O_3 mole fraction) and preserves such an occupancy figure up to ~50 GPa
568 (Fig. 5). The occupancy starts to monotonically decrease beyond 50 GPa, with a slope of
569 about -0.0009 GPa^{-1} (λ_{Al2O3} = 0.105 Al_2O_3 mole fraction, at 80 GPa; Fig. 5). This takes place
570 in combination with an increase of the phase fraction of Al-bearing perovskite.
571
572 *4.2.2 Al-uptake in perovskite from a closed system model*
573 The Al-occupancy factor $\xi_{closed\ system}$, as reported in equations (10)-(11) and (12), minimises
574 the Gibbs energy and maximises the equilibrium constant of equ.(7.a), *i.e.* if $\lambda=\xi_{closed\ system}$
575 then $K(P,T,\lambda)$ takes its maximum value. $\xi_{closed\ system}$ exhibits a linear and increasing trend,
576 trailing down the mantle (Fig. 6). This implies that the perovskite structure incorporates more
577 and more aluminium as the pressure increases, if the system is *chemically adiabatic* and *cor*
578 only competes to host Al. Such a result can be seen in terms of that if a given amount of Al
579 must be "*perforce*" accommodated over perovskite and *cor*, then aluminium chooses

progressively the former with respect to the latter with increasing *P*, thus yielding a shift of reaction (5) to the right.

4.3 Solid mixing model performances with respect to some experimental data

We tested the physical soundness of our mixing energy model comparing its predictions with some experimental results related to *Mg-Al-pv* properties.

The enthalpy formation of the reaction 0.05 Al_2O_3 (*cor*) + 0.95 $MgSiO_3$ = $Mg_{0.9}Si_{0.9}Al_{0.1}O_3$ was measured to be as large as -0.8(±2.2) kJ/mol by Navrotsky et al. (2003). Such a figure is to be compared with -1.1 kJ/mol from our calculations. Although our estimation is 40% larger than the experimental value, the exothermic nature of the reaction is correctly predicted and, taking into account the uncertainty of measurements, observation and theoretical estimate are in good agreement. In Figure 7, we report the absolute values of the discrepancy between measurements (Walter et al., 2004) and our predictions on the Al-bearing perovskite cell volume. In most cases, the deviation lies below 0.8%, and just for three experimental points we observe a discrepancy above 1%. Altogether, the average disagreement is about 0.4% and indicates a chemical-physical soundness of the solid mixing model we are using.

5. DISCUSSION

5.1 Aluminium storage mechanism

Our results from the open system model point to a complex mechanism of Al-uptake in perovskite as a function of pressure (Figs.3-5). In particular, the aluminium storage involves both the *Mg-Al-pv* phase proportion and the average Al_2O_3-mole fraction incorporated by *Mg-Al-pv* (*i.e.* λ_{Al2O3}; see equ.(9.b)). Whereas λ_{Al2O3} (Fig. 5) changes comparably little and, in

606 general, moderately decreases at large pressures, the phase fraction of *Mg-Al-pv* grows by
607 ~16% upon increasing *P* (Fig. 3).
608 We underline that our model relies on mass transfer reactions within a chemically
609 unconstrained open system constituted by *Mg-pv+Mg-Al-pv+cor* that act as Al-Mg-Si
610 exchangers with an ideal reservoir; therefore, the calculated maximum Al-uptake capacity in
611 perovskite is independent of the geochemical frame.
612 A lower mantle composition with chondritic Mg/Si ratio of ~1.01 implies an amount of
613 perovskite from 83 up to 90 wt%, juxtaposed to the pyrolitic composition that predicts
614 perovskite in the narrow range of 75-78 wt% (Lyubetskaya and Korenaga, 2007, McDonough,
615 2016). The relative proportion of this phase in a lower mantle mixed with 3% of MORB-like
616 component does not significantly vary with respect to the reference models (Table 1). This is
617 consistent with the fact that the total *chemical probability of formation*, *p*(J,chem), of the Mg-
618 rich perovskite-type phases (*i.e. Mg-pv+Mg-Fe-pv+Mg-Al-pv*) does not significantly change
619 between the primitive (A and A1) and non-primitive (A+3%B and A1+3%B) lower mantle
620 models (Table 2).
621 The predicted *total* Al_2O_3 that *Mg-Al-pv* may accommodate is shown in Figure 8, along with
622 the *bulk* Al-content inferred for primitive and enriched lower mantle compositions. We point
623 out two aspects:
624 (i) the average *total* Al_2O_3 that perovskite (76 and 85 wt% in pyrolite and chondrite reference
625 models, respectively) hosts is 4.28 and 4.78 wt% of the lower mantle mass. Such figures
626 prove that perovskite is able to accommodate *almost* the entire budget of Al_2O_3 estimated for
627 non-primitive lower mantle compositions. Perovskite exhibits an average Al-hosting capacity
628 of ~90%, in the case of pyrolite model (Al_2O_3: 4.76 wt%), and > 100%, in the case of
629 chondrite model (Al_2O_3: 4.31wt%). See also Table 1 and Figure 8;
630 (ii) the *total* Al_2O_3 stored by *Mg-Al-pv* as a function of *P-T* (Fig. 8) varies in a comparatively
631 narrow range from 24 to about 60 GPa (~4.18-4.24 wt% and ~4.67-4.75 wt%, for pyrolite and

chondrite models, respectively), while it decreases going down the mantle (3.99 and 4.47 wt%, for pyrolite and chondrite models, respectively), at 80 GPa. This may be related to the occurrence of the already mentioned change of trend exhibited by the average equilibrium constant (Fig. 2). The decrease of the λ_{Al2O3}-values (Fig. 5) and the "saturation" of the Al_2O_3-partitioning between perovskite and *cor* (Fig. 4) point to: i) a progressive reduction in the Al-storage capacity of *Mg-Al-pv*; ii) a change of the *cor*/*Mg-Al-pv* trend that might reflect the onset of instability in perovskite, probably leading to the formation of other aluminium hosting phases (*i.e*. structural change to post-perovskite; Murakami et al., 2004; Shim et al., 2008; Tsuchiya and Tsuchiya, 2008; Tateno et al., 2009). We believe that it is physically incongruous that at *P*~ 60-80 GPa the *cor*/perovskite molar ratio inverts its decreasing trend, as this suggests that *Mg-Al-pv* loses competitiveness with respect to *cor* in hosting aluminium upon increasing *P*. In fact: i) *cor* undergoes a phase transition to the rhodium-oxide-like phase in the range of ~80-100 GPa (Thomson et al., 1996; Funamori and Jeanloz, 1997; Merli and Pavese, 2018); ii) the Al-content in perovskite monotonically decreases with pressure (60-80 GPa; Fig.5), thus implying a reduction of the strain, which is due to the occurrence of species other than Mg-Si. Such a reduction of the strain is expected to promote the stability of a perovskite-like structure.

Altogether, it can be observed that:

i) aluminium is *globally* incorporated foremost *via* an increase of the Al-bearing perovskite amount, rather than by an increase of the Al_2O_3-content in *Mg-Al-pv* chemical composition;

ii) the perovskite phase is able to accommodate an Al-excess consistent with 3 wt% MORB-component mixed with primitive lower mantle compositions, up to 100% and 90% of the Al_2O_3-budget, in the case of chondrite and pyrolite models, respectively.

At higher pressure than those investigated here, the transformations of corundum to a more stable structure (~80-100 GPa) as above-mentioned and of perovskite to the $CaIrO_3$-like phase (often called post-perovskite) at ~120 GPa (Murakami et al., 2004) might account for the

658 change of the trend related to the Al-storage capacity of perovskite (Fig. 4). In fact, calculated
659 phase equilibria in the $MgSiO_3$-Al_2O_3 system, modelled at *P-T* conditions relevant for the
660 Earth's deepest mantle (80-140 GPa/2000-4000 K), predict the appearance of (Al-bearing)-
661 post-perovskite coexisting with Mg-perovskite between 90 and 105 GPa, at *T* =2000 and 3000
662 K, respectively (Tsuchiya and Tsuchiya, 2008). According to the phase diagrams of these
663 authors, the perovskite structure can accommodate up to ~0.19 moles of Al_2O_3 at 80 GPa and
664 2000 K, whereas at 3000 K the solubility of alumina increases up to ~0.4 moles. Interpolation
665 yields ~0.3 moles of Al_2O_3 at 80 GPa and 2550 K. Such results can be compared with ours
666 achieved by the closed system model, which relies on the same equilibrium thermodynamics
667 approach. It is worth noting that the closed system model yields the Al_2O_3-composition of
668 *Mg-Al-pv* that mostly shifts reaction (5) to the right, *i.e.* $K(P,T,\xi_{\text{closed system}})$ has a maximum.
669 $\xi_{\text{closed system}}$ in turn, has an increasing trend trailing down the lower mantle (Figs. 1 and 6),
670 providing an Al_2O_3-content of ~0.26 moles at *P*=80 GPa, in agreement with Tsuchiya and
671 Tsuchiya (2008).
672
673 **5.2 Composition of *Mg-Al-pv* in the lower mantle**
674
675 There is a controversy on whether the negative buoyancy associated with subducted oceanic
676 crust can overcome the viscous forces in the dynamic regions of Core-Mantle-Boundary
677 (CMB) and accumulate into large thermochemical piles (*i.e.* large low-shear-velocity
678 provinces, LLSVP: Li and McNamara, 2018). Conversely, a general *consensus* is that most of
679 the subducted crust is variably stirred into the background mantle and completely dissolved,
680 in a time span that varies from 0.1 to 1 Ga (Kumari et al., 2016; White, 2015; Foley and Rizo,
681 2017; Yu et al., 2018).
682 Using the phase proportions of *Mg-pv*, *Mg-Al-pv* and *cor* as a function of the exchanged
683 alumina according to reaction (5), we can reconstruct the probability to find *Mg-Al-pv* with a

given composition in Al_2O_3 (*i.e. occurrence probability*: p_o%). Note that p_o% must not be confused with the *chemical probability of formation*, *i.e.* *p*(J,chem), discussed in section 3.1 and that represents the mere probability to have the right oxide combination to form a given phase.

The probability of the occurrence of perovskite with low Al_2O_3-content *per* formula unit (0.01-0.15 mole fraction) is ~28% at 24 GPa/1919 K, and increases up to ~43% at 80 GPa/2550 K. In general, low alumina compositions (0.01-0.15 mole fractions) are dominant at any *P-T* explored (Fig. 9). On the contrary, the occurrence of *Mg-Al-pv* with high alumina contents in the range 0.19-0.30 mole fraction drops from ~9.8% to ~2%, passing from 24 GPa/1919 K to 80 GPa/2550 K, respectively. Compositions of natural Al-bearing perovskite, occurring as diamond inclusions and "*claimed*" to be ascribable to the lower mantle (Kaminsky, 2012; Harte and Richardson 2012; Harte et. 1999), lie in the Al_2O_3-range associated with the largest occurrence probability (*i.e.* p_o%). Leaving any opinion about their representativeness of the lower mantle mineralogy aside, there is a consistency between observations and our predictions (Fig. 9).

To conclude, *Mg-Al-pv* competes with *Mg-pv* to the phase composition of the lower mantle (Fig. 3) and the probability to find *Mg-Al-pv* in the lower mantle is almost of the same order of magnitude as *Mg-pv* (Fig. 9). In addition, the distribution of Al in *Mg-Al-pv* shows that, among the possible Al-bearing perovskite phases, the $(Mg_{0.89}Al_{0.11})(Si_{0.89}Al_{0.11})O_3$ composition is the likeliest, providing some 8% of the bulk perovskite at 80 GPa (Fig. 9). The occurrence of the Al-richest composition, *i.e.* $(Mg_{0.71}Al_{0.29})(Si_{0.71}Al_{0.29})O_3$, is always a very rare event, *i.e.* $p_o\% < 1.7\%$.

6. CONCLUSIONS

We modelled the capacity of perovskite to uptake aluminium in a non-primitive Earth's lower mantle, because of an enrichment by 3 wt% of recycled crustal material (MORB-component). The investigated region stretches from 24 to 80 GPa and is geochemically described in the framework of pyrolite and chondrite reference models. The open system model here used to predict perovskite Al-incorporation capacity is independent of the geochemical framework.

Aluminium is *globally* incorporated foremost *via* an increase of the Al-bearing perovskite amount [*Mg-Al-pv*(24 GPa)/*Mg-Al-pv*(80 GPa)≈1.17], rather than by an increase of the Al_2O_3-content in its chemical composition. At 32 GPa perovskite hosts Al_2O_3 at its maximum capacity (λ_{Al2O3}=0.134 Al_2O_3 mole fraction) and conserves such a figure up to ~50 GPa; at higher pressure, a continuous decrease of Al_2O_3-content in *Mg-Al-pv* composition takes place up to 80 GPa (λ_{Al2O3}=0.107 Al_2O_3 mole fraction).

Approaching 80 GPa, perovskite reaches some sort of "saturation" of its capacity to host aluminium, which can be considered as a prelude to instability, most likely leading to the formation of other phases (*i.e.* structural change to post-perovskite) that accommodate Al. This is in keeping with the resulting phase equilibria in the $MgSiO_3$-Al_2O_3 system, earlier modelled at *P-T* conditions relevant for the Earth's deepest mantle (80-140 GPa/2000-4000 K).

The probability to observe a perovskite composition having an Al_2O_3 mole fraction up to 0.15 is about 28% at 24 GPa, increasing to 43% at 80 GPa; on the contrary, compositions in the range 0.19-0.30 Al_2O_3 mole fraction drop their occurrence probability from 9.8 to 2.0%. In light of this, the Al-content of perovskite cannot be directly related to *P-T* conditions of formation, save that "large" Al_2O_3 contents suggest unlikely deep provenance, within the range here explored.

The *total* Al_2O_3 that perovskite (amounting to 76 and 85 wt%, in pyrolite and chondrite reference models, respectively) may host is on average 4.3-4.8 wt% of the lower mantle mass. In particular, perovskite alone can account for an Al_2O_3-storage capacity that accommodates

735 100% Al_2O_3 predicted by a non-primitive chondrite model, and 90% Al_2O_3, forecast by a non-
736 primitive pyrolite model. Calcium-ferrite type phases are possible competitors of perovskite
737 in hosting aluminium (up to 1/5 of available Al), though their low *chemical probability of*
738 *formation* likely reduces such potential. In the case of a non-primitive pyrolite lower mantle,
739 Al-bearing phases other than perovskite should exist, and the CF-type phase is a candidate
740 that might compensate for the 10% gap in perovskite Al-incorporation capacity.
741
742 **AKNOWLEDGEMENTS**
743
744 This work was partly supported by PRIN-2015 20158A9CBM Grant (C.B) and PRIN 2017 -
745 2017L83S77 (A.P). The paper benefited from the English language editing provided by Steve
746 Deforie and Barbara Galassi (Brighton, U.K). The Authors are indebted to the associated
747 Editor and two anonymous Referees for their comments and suggestions, which remarkably
748 improved the quality of the originally submitted manuscript.
749
750 **APPENDIX I**
751
752 **I.1 Open and closed systems**
753
754 An open system is permeable to both energy (heat and work) and matter, which are
755 exchanged between the system and a reservoir (De Groot and Mazur 1984; Mikhailov and
756 Ertl 2017). A closed system is able to exchange with a reservoir energy only. Let us assume to
757 have a generic system in which the following reaction occurs (we restrict our discussion to
758 one reaction only, for the sake of simplicity)

$$\sum_j \nu_j A_j = \sum_k \nu_k A_k \Longrightarrow \sum_l \nu_l A_l = 0 \qquad \text{(I. a)}$$

where $\{A_j\}$ and $\{A_k\}$ are "reactants and products" or "phases", which we shall term "reactants" *tout court*. The evolution as a function of time of the l^{th}-reactant is given by

$$\frac{dn_l}{dt} = \nu_l \frac{d\varepsilon}{dt} + \frac{d\Delta n_l}{dt} \qquad \text{(I. b)}$$

where n_l means number of moles of the l^{th}-reactant; ε is the reaction rate; the first term of the right-hand side member represents the change in n_l due to the reaction (I.a); the second term accounts for a matter exchange with a reservoir.

We split the entropy of such a system into two terms (Prigogine 1968):

$$\frac{dS_{ext}}{dt} = \frac{\delta Q}{T} - \sum_l \frac{\mu_l}{T} \frac{d\Delta n_l}{dt} \qquad \text{(I. c)}$$

$$\frac{dS_{int}}{dt} = -\sum_l \frac{\nu_l \mu_l}{T} \frac{d\varepsilon}{dt} \qquad \text{(I. d)}$$

where S_{ext} is the contribution by an exchange of heat and matter with an external reservoir; S_{int} represents the entropy produced by the reaction itself. Combining equ.(I.b), (I.c) and (I.d), it follows that

$$\frac{dS}{dt} = \frac{\delta Q}{T} - \sum_l \frac{\nu_l \mu_l}{T} \left(\frac{d\varepsilon}{dt} + \frac{1}{\nu_l} \frac{d\Delta n_l}{dt} \right) \qquad \text{(I. e)}$$

where S is the total entropy. We focus our attention on *stationary* processes, which are not necessarily at equilibrium. They exhibit observables that do not change over time (Pokrovskii 2013), and therefore

$$\frac{dn_l}{dt} = 0 \qquad \text{(I. f. 1)}$$

$$\frac{dS}{dt} = 0 \qquad \text{(I. f. 2)}$$

Taking into account (I.b), (I.e) and (I.f.1), the fulfilment of the constraint (I.f.2) requires that δQ=0. Therefore, it can be concluded that a stationary system is characterized by a possible exchange of matter with a reservoir, but not an exchange of heat.

I.2 Open system representation

The correct treatment of a system like the one introduced above requires, in principle, to be able to formulate explicitly both (I.c) and (I.d). Our aim is simpler, as we would like to exploit the capacity of an open system to freely exchange matter with a reservoir, in combination with a formalism as close as possible to the consolidated equilibrium thermodynamics' one. Such a model provides a flexible tool to approach problems in which one investigates the intrinsic exchanging/incorporation capacity of a given substance, without any sort of constraint or restraint.

An internal observer (*i.e.* an observer who measures the system's observables only, unaware of the matter flow) perceives a stationary open system as one that is under equilibrium conditions (P,T and $\{n_j\}$ do not change over time and δQ=0). Therefore, all the state functions are invariant *versus* t and the system conserves its composition), with possible forward-backward reactions and without any in/out-flow of energy/matter. Let us represent the chemical potential of the l-reactant by the usual expression below,

$$\mu_l = \mu_{0l} + RTln(x_l) + RTln(\gamma_{l,int}) \qquad \text{(I. g)}$$

where μ_{0l} is the component that depends on P-T only, and coincides with the Gibbs energy of the l^{th}-reactant alone; $\gamma_{l,int}$ is the activity coefficient of the l^{th}-reactant according to the internal observer and incorporates any sort of deviation from ideal mixing.

Let us assume that $\{n_l\}$ can fluctuate, δn_i, in such a way that (I.f.1) is satisfied *on average*, yet preserving the global system's composition. Therefore, the internal observer perceives that the conservation of composition is achieved through a transformation of the reactants into each other, according to the classical relationship below

$$\frac{\delta n_l}{\nu_l} = \delta\hat{\varepsilon} \qquad \text{(I. h)}$$

for any l-reactant; $\delta\hat{\varepsilon}$ is the infinitesimal change of the reaction ratio, seen by the internal observer. Using the equation above, we have that

$$dG = \left[\sum_l \nu_l \mu_{0l} + RTln\left(\prod_l x_l^{\nu_l}\right) + RTln\left(\prod_l \gamma_{l,int}^{\nu_l}\right)\right] \delta\hat{\varepsilon} \qquad \text{(I. i)}$$

799 The internal observer states that dG=0, given that the system is supposed at equilibrium, and
800 from (I.i) the usual chemical equilibrium equation follows

$$exp\left(-\frac{\sum_l \nu_l \mu_{0l}}{RT}\right) = \frac{\prod_k x_k^{\nu_k}}{\prod_j x_j^{\nu_j}} \times \frac{\prod_k \gamma_{k,int}^{\nu_k}}{\prod_j \gamma_{j,int}^{\nu_j}} = K(P,T)_{int} \qquad \text{(I. k)}$$

801 An external observer (*i.e.* an observer that is aware of the matter flow) confirms that dG=0 as
802 the system lies in a stationary state, and using (I.b) expresses dG in terms of

$$dG = \left[\sum_l \nu_l \mu_{0l} + RTln\left(\prod_l x_l^{\nu_l}\right) + RTln\left(\prod_l \gamma_{l,ext}^{\nu_l}\right)\right] \delta\varepsilon + \left[\sum_l \delta\Delta n_l \mu_{0l} + RTln\left(\prod_l x_l^{\delta\Delta n_l}\right) + RTln\left(\prod_l \gamma_{l,ext}^{\delta\Delta n_l}\right)\right] \qquad \text{(I. l)}$$

803 where $\delta\Delta n_l$ is the fluctuation due to the amount of l-reactant supplied by the reservoir *via* a
804 matter flow; $\gamma_{l,ext}$ is the activity coefficient estimated by the external observer. Given that the
805 global system's composition does not change in a stationary state, then the following
806 relationship must hold for $\delta\Delta n_l$, too,

$$\frac{\delta\Delta n_l}{\nu_l} = \delta\zeta$$

807 which implies

$$dG = \left[\sum_l \nu_l \mu_{0l} + RTln\left(\prod_l x_l^{\nu_l}\right) + RTln\left(\prod_l \gamma_{l,ext}^{\nu_l}\right)\right](\delta\varepsilon + \delta\zeta) \qquad \text{(I. m)}$$

808 Equ.(I.m), in combination with dG=0, leads to an expression similar to (I.k), save the term
809 depending on the activity coefficients, *i.e.* $\prod_l \gamma_{l,ext}^{\nu_l}$, so that

$$exp\left(-\frac{\sum_l \nu_l \mu_{0l}}{RT}\right) = \frac{\prod_k x_k^{\nu_k}}{\prod_j x_j^{\nu_j}} \times \frac{\prod_k \gamma_{k,ext}^{\nu_k}}{\prod_j \gamma_{j,ext}^{\nu_j}} = K(P,T)_{ext} \qquad \text{(I. n)}$$

810 Therefore, the γ activity coefficients "collect" the deviations from equilibrium that the internal
811 and external observers detect. For (I.n) and (I.k) to coincide with one another, $\prod_l \gamma_{l,ext}^{\nu_l} =$
812 $\prod_l \gamma_{l,int}^{\nu_l}$ must hold.

An open system may change its composition evolving towards a stationary state, according to the expression below, for the l^{th}-reactant:

$$\int_0^{\infty} \frac{d\Delta n_l}{dt} dt = \Delta n_l(\infty) - \Delta n_l(0)$$

where it can be assumed that at $t \to \infty$ the open system has achieved a stationary state.

I.3 Reactant proportions and probability

What does it physically mean to neglect the activity coefficients in equations (I.n) and (I.k)? Let us assume that a system has a known average Gibbs energy value, *i.e.* $<G>$ at *P*-*T*, and that it may occupy given "states", each one with a probability $\{p_l\}$. Following a consolidated approach of statistical mechanics and information theory (Jaynes 1957a-b), we state that the likeliest and least prejudicial $\{p_l\}$-set constrained to yield $<G>$ must correspond to an extreme of the expression beneath

$$\Phi = -R \sum_l p_l \ln(p_l) + \psi \left[\sum_l p_l G_l - < G > \right] \qquad \text{(I. o)}$$

where G_l is the Gibbs energy of the l^{th}-state; R is the gas constant and ψ is a lagrangian multiplier. If one requires that $\delta\Phi=0$, then

$$p_l \propto \exp\left(-\frac{G_l}{RT}\right) \qquad \text{(I. p)}$$

taking $\psi=1/T$. Let us shape our system in terms of a multi-phase system, in which the "states" are represented by the "reactants" that can occur. Let the system undergo a reaction like (I.a) and be composed of the related reactants. We analyse equ.(I.a) in statistical terms. The occurrence of the left-hand or right-hand side member, can be modelled using the notion of "joint probability", thus obtaining

$$p_{left-hand\ side\ member} \propto \prod_j p_j^{\nu_j}$$

and

$$p_{right-hand\ side\ member} \propto \prod\nolimits_k p_k^{\nu_k}$$

We take the ratio $p_{right\text{-}hand\ side\ member}/p_{left\text{-}hand\ side\ member}$, and observe that it can be either written as

$$\prod\nolimits_l p_l^{\nu_l}$$

or formulated as

$$\prod\nolimits_l \left[exp\left(-\frac{G_l}{RT}\right)\right]^{\nu_l} = exp\left(-\frac{\sum_l \nu_l G_l}{RT}\right)$$

by means of (I.p). Hence, the equations above lead to

$$\prod\nolimits_l p_l^{\nu_l} = exp\left(-\frac{\sum_l \nu_l G_l}{RT}\right) \qquad \text{(I. q)}$$

Equ.(I.q) is readily likened to (I.n) and (I.k), neglecting the activity coefficients and setting for each phase $G_l \equiv \mu_{0l}$. Altogether, a chemical equilibrium equation is thus formulated in a very simple and general fashion, which holds for stationary systems, too. Therefore, neglecting the activity coefficient terms in (I.n) and (I.k) leads to revising the notion of "l^{th}-reactant proportion", x_l, in terms of "l^{th}-reactant occurrence probability", p_l, *i.e.* $x_l \equiv p_l$, once a given reaction is being considered.

APPENDIX II

II.1 Approximation to unity of the activity coefficients term of equ.(7.a)

The activity coefficient term of equ.(7.a) can be simplified as

$$\gamma = \frac{\gamma_1}{\gamma_2^{1-\lambda} \times \gamma_3^{\lambda}} \qquad \text{(II. a)}$$

where we replaced *Mg-Al-pv*, *Mg-pv* and *cor* with 1, 2 and 3, respectively. Let us introduce the geometric average of the $\gamma_{1,2,3}$s, *i.e.*

$$\gamma_{ave} = (\gamma_1 \times \gamma_2 \times \gamma_3)^{1/3}$$

851 and

$$\gamma_1 = \gamma_{ave} + \delta_1 \qquad \text{(II. b. 1)}$$

$$\gamma_2 = \gamma_{ave} + \delta_2 \qquad \text{(II. b. 2)}$$

$$\gamma_3 = \gamma_{ave} + \delta_3 \qquad \text{(II. b. 3).}$$

852 Replacing γs in (II.a) with (II.b.1-2-3), then it is obtained

$$\gamma = \frac{\left(1+\frac{\delta_1}{\gamma_{ave}}\right)}{\left(1+\frac{\delta_2}{\gamma_{ave}}\right)^{1-\lambda} \times \left(1+\frac{\delta_3}{\gamma_{ave}}\right)^{\lambda}} \approx \frac{\left(1+\frac{\delta_1}{\gamma_{ave}}\right)}{\left(1-(1-\lambda)\frac{\delta_2}{\gamma_{ave}}\right) \times \left(1-\lambda\frac{\delta_3}{\gamma_{ave}}\right)} \approx$$

$$\approx \left(1+\frac{\delta_1}{\gamma_{ave}}\right) \times \left(1+(1-\lambda)\frac{\delta_2}{\gamma_{ave}}\right) \times \left(1+\lambda\frac{\delta_3}{\gamma_{ave}}\right)$$

$$\approx 1 + \frac{\delta_1 + (1-\lambda)\delta_2 + \lambda\delta_3}{\gamma_{ave}} + o\left(\left(\frac{\delta}{\gamma_{ave}}\right)^2\right) \approx 1 \qquad \text{(II. c)}$$

853 The approximation above requires $\delta/\gamma_{ave}<1$, which holds in most cases. In fact, earlier excess
854 enthalpy determinations on some H*P*-minerals (for instance, Fe-periclase: Sreçec et al. 1987;
855 garnets: Geiger et al. 1987; olivine: Kojitani and Akaogi 1994; Al-perovskite: Akber-Knutson
856 and Bukowinski 2004; Panero et al. 2006) exhibit absolute Δ*H*-maximum-values that yield
857 average activity coefficients [estimated by $exp(\Delta H_{max}/RT)$, T=2000 K] lying between 1.07 and
858 1.34, with a geometric average of 1.2 and $<\delta/\gamma_{ave}>$~0.08. Note that $\delta_1+\delta_2(1-\lambda)+\delta_3\lambda$ is
859 expected to be in general small as the δs compensate each other, due to δ_1, δ_2, and δ_3 not
860 being of the same sign. Therefore, given that we can legitimately neglect the activity
861 coefficient in the case of equ.(7.a), x_ls and p_ls coincide with each other, according to
862 APPENDIX I.3.

REFERENCES

Akber-Knutson S. and Bukowinski M.S.T. (2004) The energetics of aluminium solubility into $MgSiO_3$ perovskite at lower mantle conditions. *Earth Planet. Sci. Lett.* **220**, 317–330

Akber-Knutson S., Steinle-Neumann G. and Asimow, P.D. (2005) Effect of Al on the sharpness of the $MgSiO_3$ perovskite to post-perovskite phase transition. *Geophys. Res. Lett.* **32,** L14303.

Anderson D.L. (1989) Composition of the Earth. *Science* **243**, 367–370.

Badro J., Cote A. S., Brodholt J. P. (2014) A seismologically consistent compositional model of Earth's core, *Proc. Nat. Acad. Sci*. USA., **111,** 7542–7545.

Baker J.A., Schiller M., Bizzarro M. (2012) ^{26}Al-^{26}Mg deficit dating ultramafic meteorites and silicate planetesimal differentiation in the early Solar System? *Geochim. et Cosmochim. Acta*, **77**, 415-431.

Ballmer M.D., Houser C., Hernlund J.W., Wentzcovitch R.M., and Hirose K. (2017) Persistence of strong silica-enriched domains in the Earth's lower mantle. *Nat. Geosci.* DOI: 10.1038/NGEO2898.

Billen, M. I. (2010) Slab dynamics in the transition zone. Phys. Earth Planet. Inter. 183, 296–308.

Brown J. M., Shankland T. J. (1981). Thermodynamic parameters in the Earth as determined from seismic profiles. *Geoph. J. Royal Astronom. Soc*. **66**, 579–596.

Christensen U. R., Yuen D. A., (1984) The interaction of a subducting lithospheric slab with a chemical or phase boundary. *J. Geophys. Res*. **89**, 4389–4402

Christensen, U. R., Hofmann A. W. (1994) Segregation of subducted oceanic crust in the convecting mantle, *J. Geophys. Res*., **99**, 19,867 –19,884.

887 Bina C.R. and Helffrich G. (2014) Geophysical Constraints on Mantle Composition. In:
888 *Treatise on Geochemistry, Second Edition,* Vol. 3 (eds: H.D. Holland and K.K Turekian),
889 Elsevier. Oxford pp. 41-65.
890 Bizzarro M., Baker J., Haack H., Lundgaard K. (2005) Rapid timescales for accretion and
891 melting of differentiated planetesimals inferred from ^{26}Al–^{26}Mg chronometry.
892 *Astrophys. J.*, **632**, L42-L44.
893 Burton B.P., van de Walle, A. (2003) First principles based calculations of the CaCO3–
894 MgCO3 subsolidus phase diagrams. *Phys. Chem. Miner.*, **30**, 88-97.
895 Catti M., Valerio G., Dovesi R. and Causà M. (1994) Quantum-mechanical calculation of the
896 solid-state equilibrium $MgO+\alpha\text{-}Al_2O_3 \rightleftarrows MgAl_2O_4$ (spinel) versus pressure. *Phys. Rev.*
897 *B*, **49**, 14179.
898 Causà M., Dovesi R., Pisani C. and Roetti, C. (1986) Electronic structure and stability of
899 different crystal phases of magnesium oxide. *Phys. Rev. B*, **33**, 1308-1316.
900 Chust T.C., Steinle-Neumann G., Dolejš D., Schuberth B. S. A. and Bunge H.P. (2017)
901 MMA-EoS: A Computational Framework for Mineralogical Thermodynamics. *J.*
902 *Geophys. Res.: Solid Earth*, **122**, 9881–9920. https://doi.org/10.1002/2017JB014501.
903 Corà F. (2005) The performance of hybrid density functionals in solid state chemistry: the
904 case of BaTiO3. *Mol. Phys*. **103**, 2483-2496.
905 De Groot S.R. and Mazur P. (1984) Non-equilibrium thermodynamics. Dover Publications.
906 Dovesi R., Saunders V.R., Roetti C., Orlando,R., Zicovich-Wilson C.M., Pascale F., Civalleri
907 B., Doll K., Harrison N.M., Bush I.J., D'Arco P., Llunell, M. (2009) CRYSTAL09
908 user's manual. University of Torino, IT, Torino.
909 Faure G. (1986) *Principles of Isotopic Geology* Wiley, New York.
910 Foley B.J., Rizo H. (2017) Long-term preservation of early formed mantle heterogeneity by
911 mobile lid convection: Importance of grainsize evolution. Earth Planet. Sci. Lett. **475**,
912 94–105

913 Fukuyama K., Ohtani E., Shibazaki Y., Kagi H., Suzuki A. (2017) Stability field of phase
914 Egg, $AlSiO_3OH$ at high pressure and high temperature: possible water reservoir in mantle
915 transition zone. *J. Mineral. Petrol. Sci*. **112**, 31-35.
916 Funamori N., Jeanloz R. (1997) High-Pressure Transformation of Al_2O_3 . *Science*, **278,** 1109-
917 1111. DOI: 10.1126/science.278.5340.1109.
918 Funamori N., Jeanloz R., Miyajima N., and Fujino K. (2000) Mineral assemblages of basalt in
919 the lower mantle, *J. Geophys. Res*., **105**, 26,037–26,043, doi:10.1029/2000JB900252
920 Gale A., Dalton C.A., Langmuir C.H., Su Y. and Schilling J.-G. (2013) The mean
921 composition of ocean ridge basalts. *Geochem. Geophys. Geosyst.***, 14,** 489–518,
922 doi:10.1029/2012GC004334.
923 Gale J.D. (1997) GULP-a computer program for the symmetry adapted simulation of solids.
924 *JCS Faraday Trans*, **93**, 629–637.
925 Gale J.D. (2005) GULP: Capabilities and prospects, *Z. Krist.*, **220**, 552-554.
926 Gasparik T., Tripathi A. and Parise J.B. (2000) Structure of a new Al-rich phase, [K,
927 Na]0.9[Mg, Fe]2[Mg, Fe, Al, Si]6O12, synthesized at 24 GPa. *Am. Mineral.*, **85**, 613–
928 618.
929 Geiger CA, Newton RC, Kleppa OJ (1987) Enthalpy of mixing of synthetic almandine-
930 grossular and almandine-pyrope garnets from high-temperature solution calorimetry.
931 *Geochim. Cosmochim. Acta*, **51**, 1755-1763.
932 Ghosh S. and Schmidt M.W. (2014) Melting of phase D in the lower mantle and implications
933 for recycling and storage of H2O in the deep mantle. *Geochim. Cosmochim. Acta*, **145**
934 72–88.
935 Guignot N. and Andrault D. (2004) Equations of state of Na–K–Al host phases and
936 implications for MORB density in the lower mantle. Phys Earth Planet. Int., 143-144:
937 107-128.

938 Harte B. and Richardson S. (2012) Mineral inclusions in diamonds track the evolution of a
939 Mesozoic subducted slab beneath West Gondwanaland. *Gond. Res*. **21,** 236–245.
940 Harte B., Harris J.W., Hutchison M.T., Watt G.R. and Wilding, M.C. (1999) Lower mantle
941 mineral associations in diamonds from Sao Luiz, Brazil. In: *Mantle Petrology: Field*
942 *Observations and High Pressure Experimentation*; *a tribute to Francis R. (Joe) Boyd*
943 *(*eds: Y. Fei, C.M. Bertka and B.O. Mysen). The Geochemical Society Special
944 Publication No 6, pp 125-153.
945 Hirose K., Fei Y., Ma Y., Mao H-K. (1999) The fate of subducted basaltic crust in the Earth's
946 lower mantle. *Nature* 397, 53–56.
947 Hirose K., Takafuji N., Nagayoshi S. and Ohishi Y. (2005) Phase transition and density of
948 subducted MORB crust in the lower mantle. *Earth Planet. Sci. Lett.* **237** 239– 251.
949 Honda S. (2017) Geodynamic Modeling of the Subduction Zone around the Japanese Islands.
950 *Monogr. Environ. Earth Planets,* **5** (2), 35–62.
951 Imada S., Hirose K., Komabayashi T., Suzuki T., Ohishi Y. (2012) Compression of
952 $Na_{0.4}Mg_{0.6}Al_{1.6}Si_{0.4}O_4$ NAL and Ca-ferrite-type phases. *Phys. Chem. Min*., **39**, 525-530.
953 Imada S., Hirose K., Ohishi Y. (2011) Stability of NAL and Ca-ferrite-type phases on the
954 join $NaAlSiO_4$-$MgAl_2O_4$. *Phys. Chem. Min*., **38**, 557-560.
955 Ismailova L., Bykova E., Bykov M., Cerantola V., McCammon C., Boffa Ballaran T., Bobrov
956 A., Sinmyo R., Dubrovinskaia N., Glazyrin K., Liermann H.P., Kupenko I., Hanfland M.,
957 Prescher C., Prakapenka V., Svitlyk V., Dubrovinsky L. (2016) Sgtability of Fe,Al-
958 bearing bridgmanite in the lower mantle and synthesis of pure Fe-bridgmanite. *Sci.*
959 *Advances*, **2**, e1600427.
960 Irifune T., Ringwood A.E., 1993 Phase transformations insubducted oceanic crust and
961 buoyancy relationships at depth of 600–800 km in the mantle. *Earth Planet. Sci.* **117**,
962 101–110.

963 Irifune T., Shinmei T., McCammon C.A., Miyajima N., Rubie D.C. and Frost D.J. (2010) Iron
964 partitioning and density changes of pyrolite in Earth's lower mantle. *Science* **327**, 193–
965 195.
966 Irifune T., Fujino K., Ohtani E. (1991) A new high-pressure form of $MgAl_2O_4$. *Nature*, **349**,
967 409-411.
968 Irifune T., Koizumi T., Ando, J. I. (1996) An experimental study of the garnet–perovskite
969 transformation in the system $MgSiO_3$–$Mg_3Al_2Si_3O_{12}$. *Phys. Earth Planet. In.* **96**, 147–157.
970 doi:10.1016/0031-9201(96)03147-0.
971 Jaynes E.T. (1957a) "Information Theory and Statistical Mechanics" (PDF). *Phys. Rev*. Series
972 II, **106**, 620–630.
973 Jaynes E.T. (1957b) "Information Theory and Statistical Mechanics" (PDF). *Phys. Rev*. Series
974 II, **108**, 171-190.
975 Javoy M., Kaminski E., Guyot F., Andrault D., Sanloup C., Moreira M., Labrosse S., Jambon
976 A., Agrinier P., Davaille A. and Jaupart C. (2010) The chemical composition of the
977 Earth: Enstatite chondrite models. *Earth and Planet. Sci. Lett*, **293**, 259-268. DOI:
978 10.1016/j.epsl.2010.02.033.
979 Jeanloz R., Knittle E. (1989) Density and composition of the lower mantle. *Phil.Trans. Royal*
980 *Soc Lon.* **A328(1599),** 377–389 doi:10.1098/rsta.1989.0042
981 Jones R.E. van Keken P. E., Hauri E., Tucker J. M., Vervoort, J., Ballentine C. J. (2019)
982 Origins of the terrestrial Hf-Nd mantle array: Evidence from a combined geodynamical-
983 geochemical approach. *Earth and Planet. Sci. Lett*, **518**, 26-39
984 Kaminski E. and Javoy, M. (2013) A two-stage scenario for the formation of the Earth's
985 mantle and core. *Earth Planet. Sci. Lett.* **365,** 97-107.
986 Kaminsky F. (2012) Mineralogy of the lower mantle: a review of super-deep mineral
987 inclusions in diamond. *Earth Sci. Rev*. **110**, 127–147.

Kaminsky F. and Lin J-F. (2017) Iron partitioning in lower mantle minerals: toward a chemically heterogeneous lower mantle. *Am Miner.*, **102**, 824-832.

Kato C., Hirose K., Komabayashi T., Ozawa H. and Ohishi, Y. (2013) NAL phase in K-rich portions of the lower mantle. *J. Geophys. Res.* **40**, 5085–5088.

King, S. D Frost . D. J., Rubie, D. C. (2015) Why cold slabs stagnate in the transition zone. *Geology* **43**, 231–234.

Kojitani H, Akaogi M (1994) Calorimetric study of olivine solid solutions in the system Mg_2SiO_4-Fe_2SiO_4. *Phys. Chem. Miner*., **20**, 536–540.

Korenaga J. (2009) A method to estimate the composition of the bulk silicate Earth in the presence of a hidden geochemical reservoir. *Geochim. Cosmochim. Acta,* **73,** 6952–6964.

Kröger F.A. (1972) *The Chemistry of Imperfect Crystals*. North-Holland, Amsterdam

Kumari S., Paul D. and Stracke A. (2016) Open system models of isotopic evolution in Earth's silicate reservoirs: Implications for crustal growth and mantle heterogeneity. *Geochim. Cosmochim. Acta* **195** 142–157.

Kurnosov A., Marquardt H., Frost D.J., Boffa Ballaran T. and Ziberna L. (2017) Evidence for a Fe^{3+}-rich pyrolytic lower mantle from (Al,Fe)-bearing bridgmanite elastic data. *Nature*, **543**, 543-546.

Lee T., Papanastassiou D.A., Wasserburg G.J. (1977) Al-26 in the early Solar-System – fossil or fuel. *Astrophys. J*., **211**, L107-L110.

Jie Li J., Viktor V. Struzhkin V.V., Mao H-k, Shu J., Hemley R.J., Fei Y., Mysen B., Dera P., Prakapenka V., Shen G. (2004) Electronic spin state of iron in lower mantle perovskite. *Proc. Nat. Acad. Sci*. USA., **101** 14027-14030

Li , L., Weidner, D.J., Brodholt, J., Alfè, D., Price, G.D. (2008) Ab initio molecular dynamics study of elasticity of akimotoite $MgSiO_3$ at mantle conditions. *Phys. Earth and Planet. Inter*. **173**, 115-120.

1013 Li M., McNamara A. K. (2013) The difficulty for subducted oceanic crust to accumulate at
1014 the Earth's core-mantle boundary. *J. Geophys. Res. Solid Earth*, **118**, 1807–1816,
1015 doi:10.1002/jgrb.50156
1016 Li M. , McNamara A. K. (2018) The influence of deep mantle compositional heterogeneity
1017 on Earth's thermal evolution. *Earth Planet. Sc. Lett.*, **500**, 86–96
1018 Litasov K. D., Ohtani E (2007) Effect of water on the phase relations in Earth's mantle and
1019 deep water cycle. Special Paper of the Geological Society of America, **421**, 115-156
1020 DOI: 10.1130/2007.2421(08)
1021 Lodders K. (2003) Solar system abundances and condensation temperatures of the elements.
1022 *Astrophys. J.* **591**, 220–1247.
1023 Lodders K., Palme H., and Gail H-P. (2009) Abundances of the elements in the solar system.
1024 In: *Astronomy and Astrophysics* Vol. VI/4B, Chap. 4.4 (ed. J.E Trumper). Landolt-
1025 Bornstein, New Series Berlin, Springer-Verlag, pp. 560-630.
1026 Lyubetskaya T. and Korenaga J. (2007) Chemical composition of Earth's primitive mantle
1027 and its variance *J. Geoph. Res.* **112**, B03211, doi:10.1029/2005JB004223.
1028 Mahan B., Siebert J., Blanchard I., Borensztajn S., Badro J. and Moynier F. (2018)
1029 Constraining compositional proxies for Earth's accretion and core formation through high
1030 pressure and high temperature Zn and S metal-silicate partitioning. *Geochim.*
1031 *Cosmochim. Acta*, **235**, 21-40.
1032 Marty B. (2012). The origins and concentrations of water, carbon, nitrogen and noble gases
1033 on Earth. *Earth Planet. Sci. Lett*. **313**, 56–66.
1034 Mattern E, Matas J., Ricard Y., Bass J. (2005) Lower mantle composition and temperature
1035 from mineral physics and thermodynamic modelling. *Geophys. J. Int.* **160**, 973–990.
1036 McDonough WF and Sun S-S (1995) The composition of the Earth. *Chem. Geol.* **120**: 223-
1037 253.
1038 McDonough W. F. (2014), Compositional model for the Earth's core. In The Mantle and

1039 Core, edited by R. W. Carlson, pp. 559–577, Elsevier, Amsterdam.
1040 Merli M. and Pavese A. (2018) Electron-density critical points analysis and catastrophe
1041 theory to forecast structure instability in periodic solids. *Acta Crystallograph. Section A*:
1042 *Foundations and Advances* **74**, 102-111.
1043 Merli M., Sciascia L., Pavese A. and Diella V. (2015) Modelling of thermo-chemical
1044 properties over the sub-solidus MgO–FeO binary, as a function of iron spin
1045 configuration, composition and temperature. *Phys. Chem. Min*. **42**, 347-362.
1046 Merli M., Bonadiman C., Diella V. and Pavese A. (2016) Lower mantle hydrogen partitioning
1047 between periclase and perovskite: A quantum chemical modelling. *Geoch. Cosmochim.*
1048 *Acta* **173**, 304-318.
1049 Merli M., Bonadiman C., Diella V., Sciascia L. and Pavese A. (2017) Fe-periclase reactivity
1050 at Earth's lower mantle conditions: *ab-initio* geochemical modelling. *Geochim.*
1051 *Cosmochim. Acta*, **214**, 14-29. https://doi.org/10.1016/j.gca.2017.07.030.
1052 Mikhailov A.S., Ertl G. (2017) Thermodynamics of Open Systems. In: Chemical Complexity.
1053 The Frontiers Collection. Springer, Cham.
1054 Mohn C.E. and Trønnes R. (2016) Iron spin state and site distribution in FeAlO3-bearing
1055 bridgmanite. *Earth Plan. Sci. Lett*., **440**, 178-186.
1056 Murakami M., Hirose K., Kawamura K., Sata N. and Ohishi Y. (2004) Post-perovskite phase
1057 transition in MgSiO3. *Science* **304**, 855-858
1058 Muir J.M.R., Brodholt J.P. (2018) Water distribution in the lower mantle: Implications for
1059 hydrolytic weakening. *Earth Plan. Sci. Lett*., **484** , 363-369. 10.1016/j.epsl.2017.11.051
1060 Murakami M., Ohishi Y., Hirao N. and Hirose K. (2012) A perovskitic lower mantle inferred
1061 from high-pressure, high-temperature sound velocity data. *Nature* **485,** 90- 95.
1062 Navrotsky A., Schoenitz M., Kojitani H., Xu H., Zhang, J., Weidner D.J. and Jeanloz R.
1063 (2003) Aluminium in magnesium silicate perovskite: Formation, structure, and energetics

of magnesium-rich defect solid solutions. *J. Geophys. Res.* **108**, B7, 2330, doi:10.1029/2002JB002055.

Nestola F., Korolev N., Kopylova M., Rotiroti N., Pearson D.G., Pamato M.G., Alvaro M., Peruzzo L, Gurney J.J., Moore A.E. and Davidson J. (2018) $CaSiO_3$ perovskite in diamond indicates the recycling of oceanic crust into the lower mantle. *Nature* **555**. 237-241.

Nishio-Hamane D., Nagai T., Fujino K., Seto Y., Takafuji N. (2005) Fe^{3+} and Al solubilities in $MgSiO_3$ perovskite: implication of the Fe^{3+}AlO3 substitution in $MgSiO_3$ perovskite at the lower mantle condition. *Geophy. Res. Lett*. **32**, L16306.

Nolet G., Allen R. and Zhao D. (2007) Mantle plume tomography. *Chem. Geol*. **241**, 248–263.

Norris T.L., Gancarz A.J., Rokop D.J., Thomas K.W. (1983) Half-life of ^{26}Al. *J. Geophys. Res*., **88** (S1), B331-B333.

Ohtani, E., Litasov, K., Suzuki, A., and Kondo, T. (2001) Stability field of new hydrous phase, δ-AlOOH, with implications for water transport into the deep mantle: *Geophys. Res. Lett.*, **28,** 3991–3993.

Ohtani E., Amaike Y., Kamada S., Sakamaki T. and Hirao N. (2014) Stability of hydrous phase H $MgSiO_4H_2$ under lower mantle conditions. *Geophys. Res. Lett.*, **41**, 8283-8287

Ottonello G. (1997) *Principles of Geochemistry*. Columbia University Press, New York

Ottonello G., Civalleri B., Ganguly J., Perger W.F., Belmonte D. and Vetuschi Zuccolini M., (2010) Thermo-chemical and thermos-physical properties of the high pressure phase Anhydrous B ($Mg_{14}Si_5O_{24}$): an *ab initio* all-electron investigation. *Am. Mineral*. **95**, 563–573.

Palme H. and O'Neill, H., (2014) . Cosmochemical estimates of mantle composition. In: *Treatise on Geochemistry*, 2nd Edition. Vol. 3 (ed. R. W Carlson). Elsevier, Oxford pp. 1–39.

1090 Pamato M.G., Myhill R., Boffa Ballaran T., Frost D.J., Heidelbach F. and Miyajima N. (2015)
1091 Lower-mantle water reservoir implied by the extreme stability of a hydrous
1092 aluminosilicate. *Nat. Geosci.* **8**, 75–79.
1093 Panero W.R., Akber-Knutson S. and Stixrude L. (2006) Al_2O_3 incorporation in MgSiO3
1094 perovskite and ilmenite. *Earth Planet. Sci. Lett*. **252**, 152-161.
1095 PetDB Petrological Database (https://www.earthchem.org/petdb)
1096 Prigogine I. (1968) Introduction to thermodynamics of irreversible processes. Third Edition.
1097 John Wiley & Sons Inc, N.Y. 9
1098 Pokrovskii V.N. (2013) A derivations of the main relations of non-equilibrium
1099 thermodynamics. *IRSN Thermodynamics,* 906136, pp 9. doi: 10.1155/2013/906136
1100 Ricolleau A., Fiquet G., Addad A., Menguy N., Vanni C., Perrillat J.P., Daniel I., Cardon H.,
1101 and Guignot N. (2008) Analytical transmission electron microscopy study of a natural
1102 MORB sample assemblage transformed at high pressure and high temperature, *Am. Min*.,
1103 **93**, 144–153, doi:10.2138/am.2008.2532.
1104 Ricolleau A., Fei Y., Cottrell E., Watson H.C., Deng L., Zhang L., Fiquet G., Auzende A.-L.,
1105 Roskosz M., Morard G. and Prakapenka V. (2009) Density profile of perovskite under the
1106 lower mantle conditions. *Geophys. Res. Lett*. **36**, L06302.
1107 Ricolleau A., Perrillat J.P., Fiquet G., Daniel I., Matas J., Addad A. Menguy N., Cardon H.,
1108 Mezouar M. and Guignot N. (2010) Phase relations and equation of state of a natural
1109 MORB: Implications for the density profile of subducted oceanic crust in the Earth's
1110 lower mantle. *J. Geophys. Res.*,**115**: B08202.
1111 Shim S-H, Catalli K., Hustoft J., Kubo A., Prakapenka V.B, Caldwell W.A., Kunz M.
1112 (2018) Crystal structure and thermoelastic properties of $(Mg_{0.91}Fe_{0.09})SiO_3$ postperovskite
1113 up to 135 GPa and 2,700 K. *Proc. Nat. Acad. Sci. U. S. A* **105**, 7382–7386
1114 Sreçec I., Ender A., Woermann E., Gans W., Jacobsson E., Eriksson G., Rosen E. (1987)
1115 Activity-composition relations of the magnesiowüstite solid solution series in equilibrium

with metallic iron in the temperature range 1050–1400 K. *Phys. Chem. Miner.*, **14**, 492–498.

Sigloch K., McQuarrie N. and Nolet G. (2008) Two-stage subduction history under North America inferred from multiple-frequency tomography, *Nat. Geosci.* **1**, 458–462, doi:10.1038/ngeo231.

Spivak-Birndorf, M. Wadhwa, P. Janney (2009) 26Al–26Mg systematics in D'Orbigny and Sahara 99555 angrites: implications for high-resolution chronology using extinct chronometers. *Geochim. Cosmochim. Acta*, **73**, 5202-5211.

Stebbins J.F., Kroeker S. and Andrault D. (2001) The mechanism of solution of aluminium oxide in MgSiO3 perovskite. *Geophys. Res. Lett*. **28**, 615–618.

Stixrude L., Lithgow-Bertelloni C. (2005), Thermodynamics of mantle minerals—I. Physical properties, *Geophys. J. Int*., **162**, 610–632.

Stixrude L. and Lithgow-Bertelloni C. (2012) Geophysics of chemical heterogeneity in the mantle. *Annual Rev. Earth Planet. Sci. Lett.* **40**, 569–595.

Tateno S., Hiros, K. Sata, N. and Ohishi, Y. (2009) Determination of post-perovskite phase transition boundary up to 4400K and implications for thermal structure in D''layer. *Earth Planet. Sci. Lett.* **277**, 130–136.

Thomson K. T., Wentzcovitch R. M. and Bukowinski, M. S. T. (1996) Polymorphs of Alumina Predicted by First Principles: Putting Pressure on the Ruby Pressure Scale. *Science* **274**, 1880–1882.

Towler M. (2015) CRYSTAL Resources Page. Theory of Condensed Matter http://www.tcm.phy.cam.ac.uk/~mdt26/crystal.html.

Tschauner O., Ma C., Prescherb C., Prakapenka V.B. (2018) Structure analysis and conditions of formation of akimotoite in the Tenham chondrite. *Meteor. and Planet. Sci*, **53**, 62-74.

Tsuchiya J., and Tsuchiya T. (2008) Post-perovskite phase equilibria in the $MgSiO_3$-Al_2O_3 system. *Proc. Nat. Acad. Sci. U. S. A* **105**, 19160-19164.

1142 Valencia-Cardona J.J., Shukla G., Wu Z. , Houser C., Yuen D.A, Wentzcovitch R. M. (2017)
1143 Influence of the iron spin crossover in ferropericlase on the lower mantle geotherm.
1144 Geophys. Res.Lett., **44**, 4863–4871, doi:10.1002/2017GL073294.
1145 van der Hilst R. D., Widiyantoro S. and Engdahl E. R. (1997) Evidence for deep mantle
1146 circulation from global tomography. *Nature* **386**, 578–584.
1147 van de Walle A., Ceder G. (2002) The effect of lattice vibrations on substitutional alloy
1148 thermodynamics. *Rev. Mod. Phys*., **74**, 11-45.
1149 Walter M.J., Kubo A., Yoshino T., Brodholt J.P., Koga K.T and Ohishi Y., (2004) Phase
1150 relations and equation-of-state of aluminous Mg-silicate perovskite and implications for
1151 Earth's lower mantle. *Earth Planet. Sci. Lett*. **222** 501–516.
1152 Walter M.J. , Thomson A.R., Wanga W., Lord O.T., Ross J., McMahon S.C., Baron M.A.,
1153 Melekhova E., Kleppe A.K. and Kohn S.C. (2015) The stability of hydrous silicates in
1154 Earth's lower mantle: Experimental constraints from the systems $MgO–SiO_2–H_2O$ and
1155 $MgO–Al_2O_3–SiO_2–H_2O$. *Chem. Geol.,* **418**, 16–29.
1156 Wang K. and Jacobsen S.B. (2016) An estimate of the Bulk Silicate Earth potassium isotopic
1157 composition based on MC-ICPMS measurements of basalts. *Geochim. Cosmochim. Acta*,
1158 **173**, 223-232.
1159 Wang X., Tsuchiya T., and Hase A. (2015) Computational support for a pyrolitic lower
1160 mantle containing ferric iron, Nat. Geosci., **8,** 556–559. doi:10.1038/ngeo2458.
1161 Wasson J. T. and Kallemeyn G. W. (1988) Compositions of chondrites. *Philos. Trans. R. Soc.*
1162 *London, Ser. A,* **325**, 535 – 544.
1163 White, W.M., 2015 Probing the Earth's deep interior through geochemistry. *Geochem.*
1164 *Perspect.***4 (2),** 95–251.
1165 Wimpenny J., Sanborn M.E., Koefoed P., Cooke I.R., Stirling C., Amelin Y. and Qing-Zhu
1166 Yin Q-Z. (2019). Reassessing the origin and chronology of the unique achondrite Asuka

881394: Implications for distribution of 26Al in the early Solar System. *Geochim. Cosmochim. Acta*, **244**, 478–501.

Wu Y., Wu X., Lin J., McCammon C.A., Xiao Y., Chow P., Prakapenka V.B., Yoshino T., Zhai S. and Qin S. (2016) Spin transition of ferric iron in the NAL phase: Implications for the seismic heterogeneities of subducted slabs in the lower mantle. *Earth Planet. Sci. Lett.* **434** 91-100.

Wu S.C., Browne E. (1997). Comments on evaluation of ^{26}Al electron-capture and position decay data. Comments on Evaluation CEA. ISBN 2 7272 0211 3.

Wu Z. and Cohen R. E. (2006) More accurate generalized gradient approximation for solids. *Phys. Rev. B*, **73**:235116.

Yamamoto T., Yuen D.A. and Ebisuzaki T. (2003) Substitution mechanism of Al ions in MgSiO3 perovskite under high pressure conditions from first-principles calculations. *Earth Planet. Sci. Lett.* **206**, 617-625.

Young E.D., Simon J.I., Galy A., Russell S.S., Tonui E. and Lovera O. (2005) Supra-canonical ^{26}Al/^{27}Al and the residence time of CAIs in the solar protoplanetary disk. *Science* **308,** 5719.

Yu C., Day E.A., de Hoop M.V., Campillo M. and Goes S., Blythe R.A. and van der Hilst R.D. (2018) Compositional heterogeneity near the base of the mantle transition zone beneath Hawaii. *Nat. Comm*. **9**, 1266.

Zhang F. and Oganov A.R. (2006) Mechanisms of Al^{3+} incorporation in $MgSiO_3$ post-perovskite at high pressures. *Earth Planet. Sci. Lett.* **248**, 69-76.

Fukao Y. & Obayashi, M. 2013 Subducted slabs stagnant above, penetrating through, and trapped below the 660 km discontinuity. *J. Geophys. Res.* **118**, 5920 5938.

CAPTIONS TO THE FIGURES

Figure 1. Equilibrium constant, $K(P,T,\lambda)$, of the fundamental alumina exchange reaction (5) *versus* λ, which expresses the exchanged amount of Al_2O_3 in the *Mg-Al-pv*, *Mg-pv* and *cor* system. $K(P,T,\lambda)$, calculated by the open system model, is displayed at 24 GPa/1919 K (blue line), 44 GPa/2145 K (red line) and 80 GPa/2551 K (black line), by way of example. Black filled circles indicate the maxima at the three chosen *P-T* points, and correspond to the λ-values that most shift the reaction (1-λ) $MgSiO_3$+λ Al_2O_3 $\leftrightarrow$ $(Mg_{1-\lambda}Al_{\lambda})(Si_{1-\lambda}Al_{\lambda})O_3$ to the right (equ.5, of the text).

Figure 2. $K(P,T)_{ave}$ *versus P*, according to the chosen geotherm and calculated by the open system model. Blue line and red line show two different trends for the average equilibrium constant, $K(P,T)_{ave}$, of the reaction (5). Note that $K(P,T)_{ave}=\langle K(P,T,\lambda)\rangle_{\lambda}$ (see 4.2.1 section for further explanations).

Figure 3. Phase proportions of Al-free perovskite (*Mg-pv*), Al-bearing perovskite (*Mg-Al-pv*) and corundum (*cor*) *versus P*, according to the chosen geotherm. *Mg-Al-pv* fractions have an average Al_2O_3 composition provided by λ_{Al2O3}, calculated according to equ.(9.b) on the *P-T* range of interest and shown in Fig.5. Al-free perovskite is an extreme notion, which provides a "limit" to define a tendency of such mineral to incorporate aluminium.

Figure 4. Al_2O_3-partitioning between corundum and perovskite (*cor*(mol)/*Mg-Al-pv*(mol)) *versus P*, according to the chosen geotherm and calculated by the open system model. The red box shows the region of maximum Al-uptake for perovskite (saturation region), suggesting that at such *P-T* conditions the Al-incorporation is weakly dependent on pressure. At higher pressure, the *cor*/*Mg-Al-pv* ratio trend hints at a possible instability of perovskite (transition to another phase, such as post-perovskite, *ppv*?). See text for further discussion.

Figure 5. Average Al_2O_3 mole fraction in perovskite, λ_{Al2O3}, determined by the open system model and calculated *via* equ.(9.b), as a function of *P* along the chosen geotherm. In the *P*-region 30-50 GPa, λ_{Al2O3} is *quasi* constant (interpolation solid line).

Figure 6. Al_2O_3 mole fraction in perovskite, $\xi_{closed\ system}$, determined by the closed system model and calculated *via* equ.(14), as a function of *P* along the chosen geotherm. At $\lambda=\xi_{closed\ system}$, $K(P,T,\lambda)$ takes an extreme value, so that reaction (5) is shifted to the right as much as possible.

Figure 7. Cell volume disagreement (%), between measurements and our calculations, in the case of Al-bearing perovskite, as a function of *P*. Experimental values from Walter et al (2004).

Figure 8. The predicted *total* Al_2O_3 (wt%) stored in *Mg-Al-pv*, calculated by the open system model, assuming perovskite amounts of 76% (red dots) and 85% (blue dots) of the lower mantle mass, in pyrolite and chondrite reference models (Table 1), respectively. Bulk Al_2O_3 contents of pyrolite (A) and chondrite (A1) primitive lower mantle models are shown by red and blue solid lines, respectively. Bulk Al_2O_3 contents of pyrolite-type and chondrite-type non-primitive lower mantle models calculated by adding a 3 wt% of MORB-component (B) are represented by red and blue dotted lines, respectively. MORB composition from Hirose et al. (1999). *P-T* region of 24-80 GPa/1919-2550 K is referred to the chosen geotherm.

Figure 9. Probability (p_o%) of *Mg-Al-pv* occurrence with a given Al_2O_3 mole content *per* formula unit, according to the open system model. Each curve is associated to key *P-T* values (*P* in legend), along the chosen geotherm. The Al_2O_3 contents of natural Al-bearing

perovskite (↔) *claimed* from the lower mantle, are provided by Kaminsky and Lin (2017). In the inset table, the absolute probability to find Al-bearing perovskite (*Mg-Al-Pv*) against Mg-perovskite (*Mg-pv*) is reported for the explored *P*-*T* region of the lower mantle.

Table 1

Table 1. Lower mantle (pyrolite, end-member A, and chondrite, end-member A1) and MORB-like silicate glass (end-member B) major oxides compositions. Enriched LM models according to Faure(1986) mixing equation.

Pyrolitic lower mantle model	A	A+3% B	B
wt%			
SiO_2	45.00	45.14	49.64
Al_2O_3	4.45	4.76	14.88
FeO_t	8.05	8.15	11.43
MgO	37.80	36.92	8.51
CaO	3.55	3.76	10.52
Na2O	0.36	0.44	2.90
H_2O	*0.15	0.149	**0.10
(Mg-pv+Mg-Fe-pv+Mg-Al-pv)$^+$	76.00	75.56	31.30

Chondritic lower mantle model	A1	A1+3% B	B
wt%			
SiO_2	47.30	47.37	49.64
Al_2O_3	3.99	4.31	14.88
FeO_t	8.12	8.22	11.43
MgO	37.36	36.50	8.51
CaO	2.29	2.54	10.52
Na_2O	0.34	0.42	2.90
H_2O	*0.15	0.149	**0.10
(Mg-pv+Mg-Fe-pv+Mg-Al-pv)$^+$	85.00	84.89	31.30

end member A from McDonough and Sun (1995)
end member A1 from Merli et al. (2016), modified
end member B= MORB-like silicate glass of Hirose et al.(1999)

+ = global estimates (wt%) of pure perovskite (*Mg-pv*), bridgmanite *(Mg-Fe-pv)* and Al beraring perovskite (*Mg-Al-pv*)
*= lower mantle water estimates from Merli et al. (2016) and Muir and Brodholt (2018)
**= MORB water estimates from Ghosh et al.(2014) and Marty (2012)

Table 2

Table 2. Probability, expressed in %, of having the appropriate elemental availability to form a given phase (*chemical probability of formation* = *p* (J,chem); see section 3.1). Calculations are carried out by Pyrolite (A) and Chondrite (A1) lower mantle reference models, and by their compositions mixed with 3 wt% of MORB-component (A+3%B; A1+3%B)

		Pyrolite		Chondrite	
Phase name	**Composition**	**A**	**A+3%B**	**A1**	**A1+3%B**
Fe-periclase	$(Mg_{0.8}Fe_{0.2})O$	33.59	33.24	32.22	31.91
Ca-perovskite	$CaSiO_3$	0.674	0.745	0.452	0.523
Mg-perovskite	$MgSiO_3$	23.89	23.84	24.63	24.55
Bridgmanite	$(Mg_{0.9}Fe_{0.1})SiO_3$	20.76	20.83	21.44	21.49
Mg-Al-perovskite	$(Mg_{0.9}Al_{0.1})(Si_{0.9}Al_{0.1})O_3$	20.24	20.41	20.49	20.66
sum		**64.90**	**65.08**	**66.56**	**66.70**
δ-phase[1]	AlO(OH)	0.052	0.058	0.044	0.049
H-phase[2]	$(MgSi,Al_2)O_4H_2$	0.045	0.047	0.043	0.045
D-phase[3]	$Al_2SiO_4(OH)_2$	0.002	0.002	0.002	0.002
NAL/CF[4]	$Na_{0.265}Fe_{0.245}Mg_{0.375}Ca_{0.035}Al_{1.1}Si_{0.715}O_4$	0.737	0.825	0.679	0.769
sum		0.836	0.932	0.768	0.865

end-member A from McDonough and Sun (1995)
end-member A1 from Merli et al.(2016), modified
end-member B= MORB-like silicate glass of Hirose et al. (1999)

1: Ohtani et al. (2001); 2: Ohtani et al. (2014); 3: Pamato et al. (2015); 4: Guignot and Andrault (2004)

Table 3

Table 3. C*hemical probability of formation* [*p* (J,chem)] expressed in % of potential lower mantle Al-bearing phases.

		Pyrolite		Chondrite	
Phase name	**Composition**	**A**	**A+3%B**	**A1**	**A1+3%B**
Mg-Al-perovskite	$(Mg_{0.9}Al_{0.1})(Si_{0.9}Al_{0.1})O_3$	96.04	95.63	96.39	95.98
δ-phase[1]	AlO(OH)	0.25	0.27	0.20	0.23
H-phase[2]	$(MgSi,Al_2)O_4H_2$	0.21	0.22	0.20	0.21
D-phase[3]	$Al_2SiO_4(OH)_2$	0.01	0.01	0.01	0.01
NAL/CF[4]	$Na_{0.265}Fe_{0.245}Mg_{0.375}Ca_{0.035}Al_{1.1}Si_{0.715}O_4$	3.50	3.87	3.20	3.57
		100.00	100.00	100.00	100.00

end-member A from McDonough and Sun (1995)
end-member A1 from Merli et al.(2016), modified
end-member B= MORB-like silicate glass of Hirose et al. (1999)

1: Ohtani et al. (2001); 2: Ohtani et al. (2014); 3: Pamato et al. (2015); 4: Guignot and Andrault (2004)

Figure 1

Click here to download high resolution image

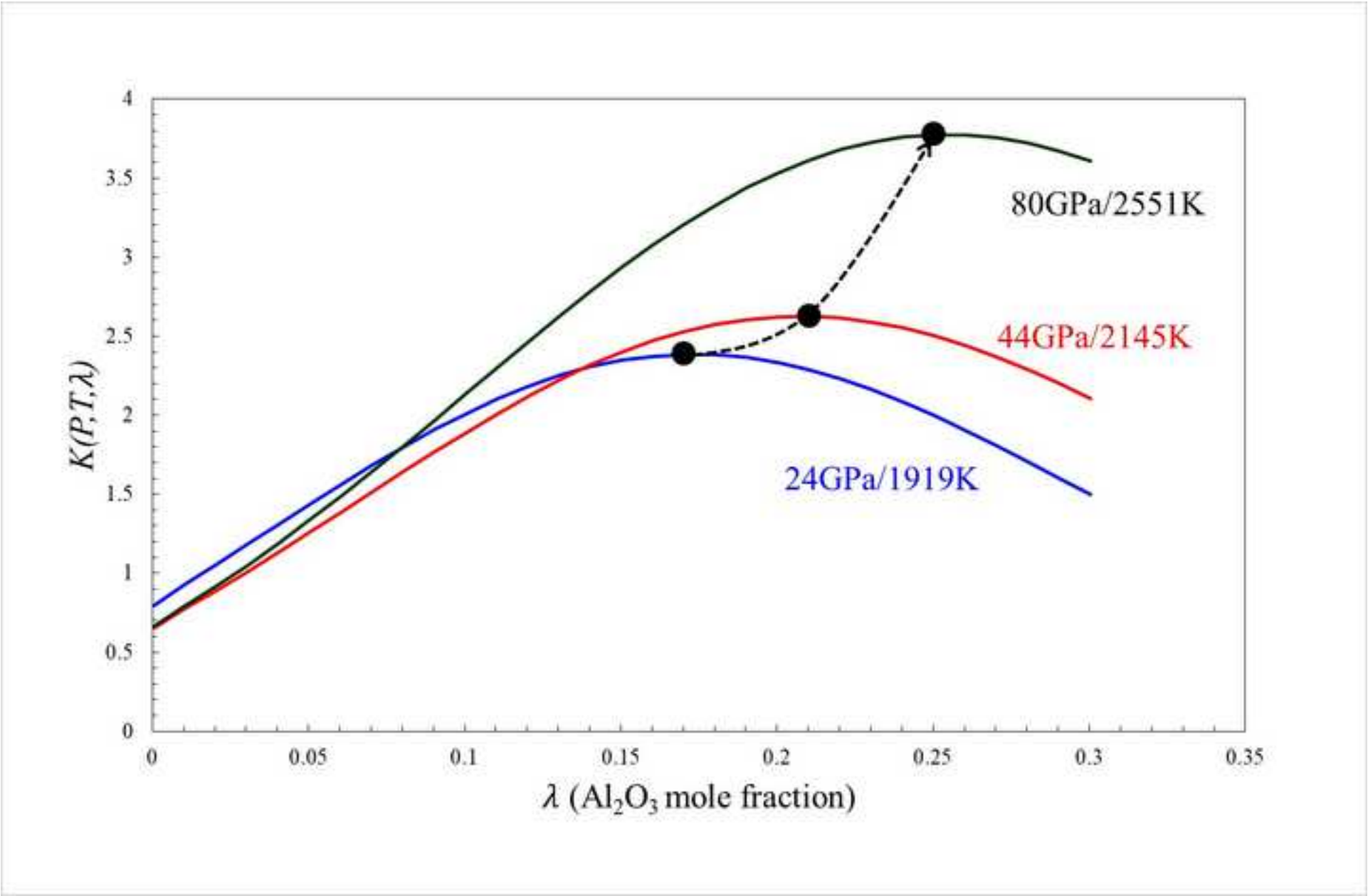

Figure 2

Click here to download high resolution image

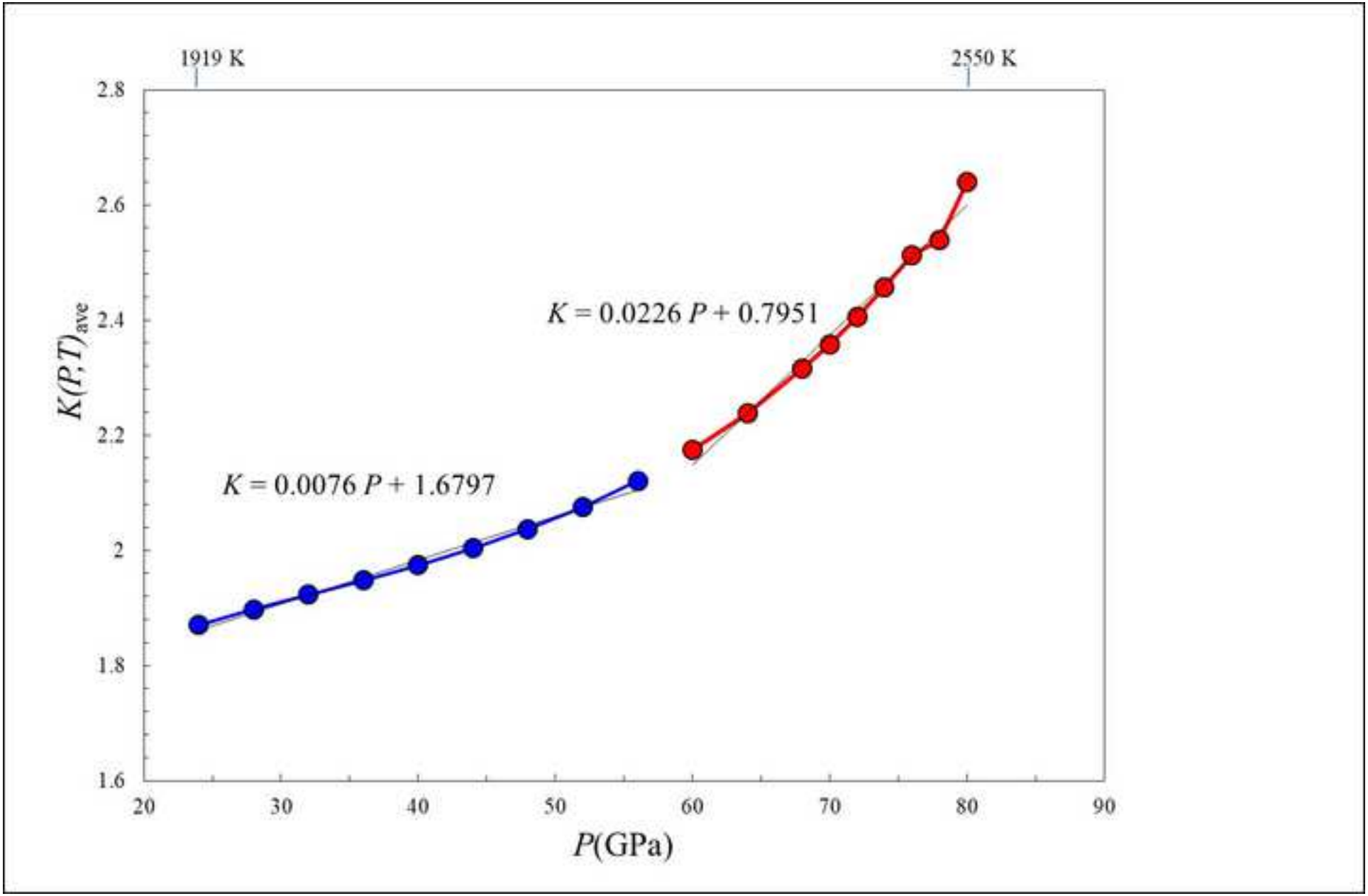

Figure 3

Click here to download high resolution image

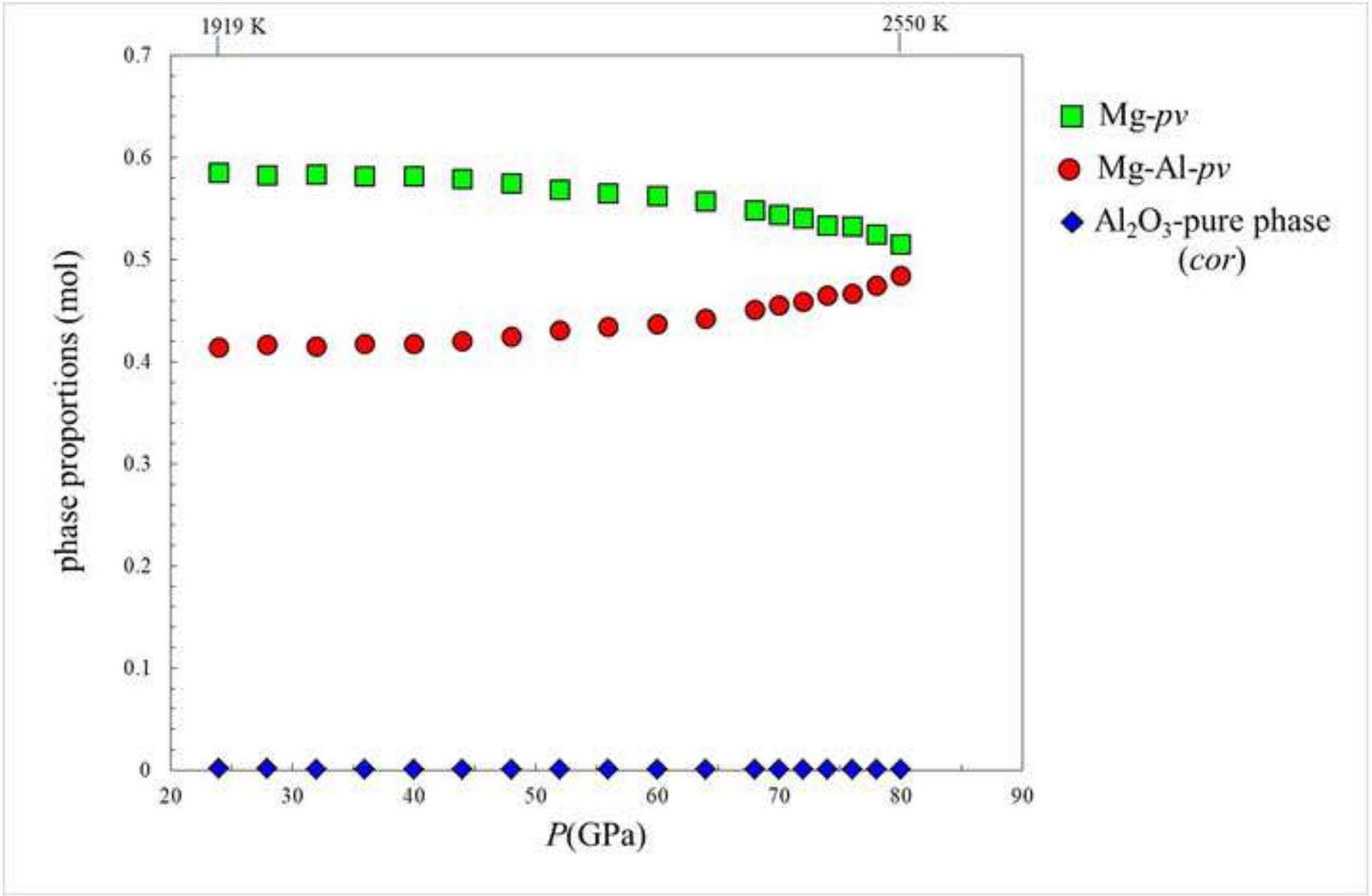

Figure 4

Click here to download high resolution image

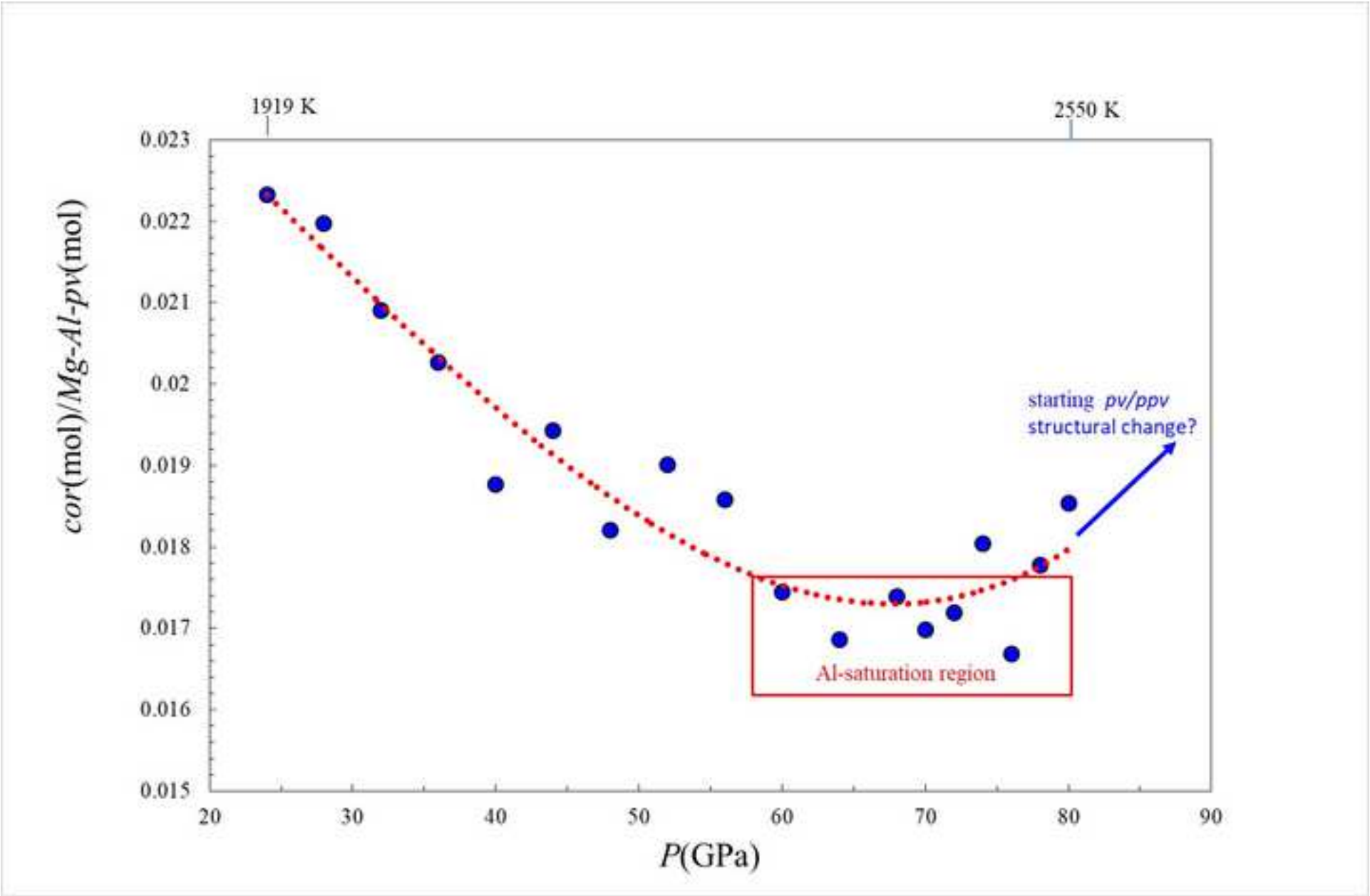

Figure 5

Click here to download high resolution image

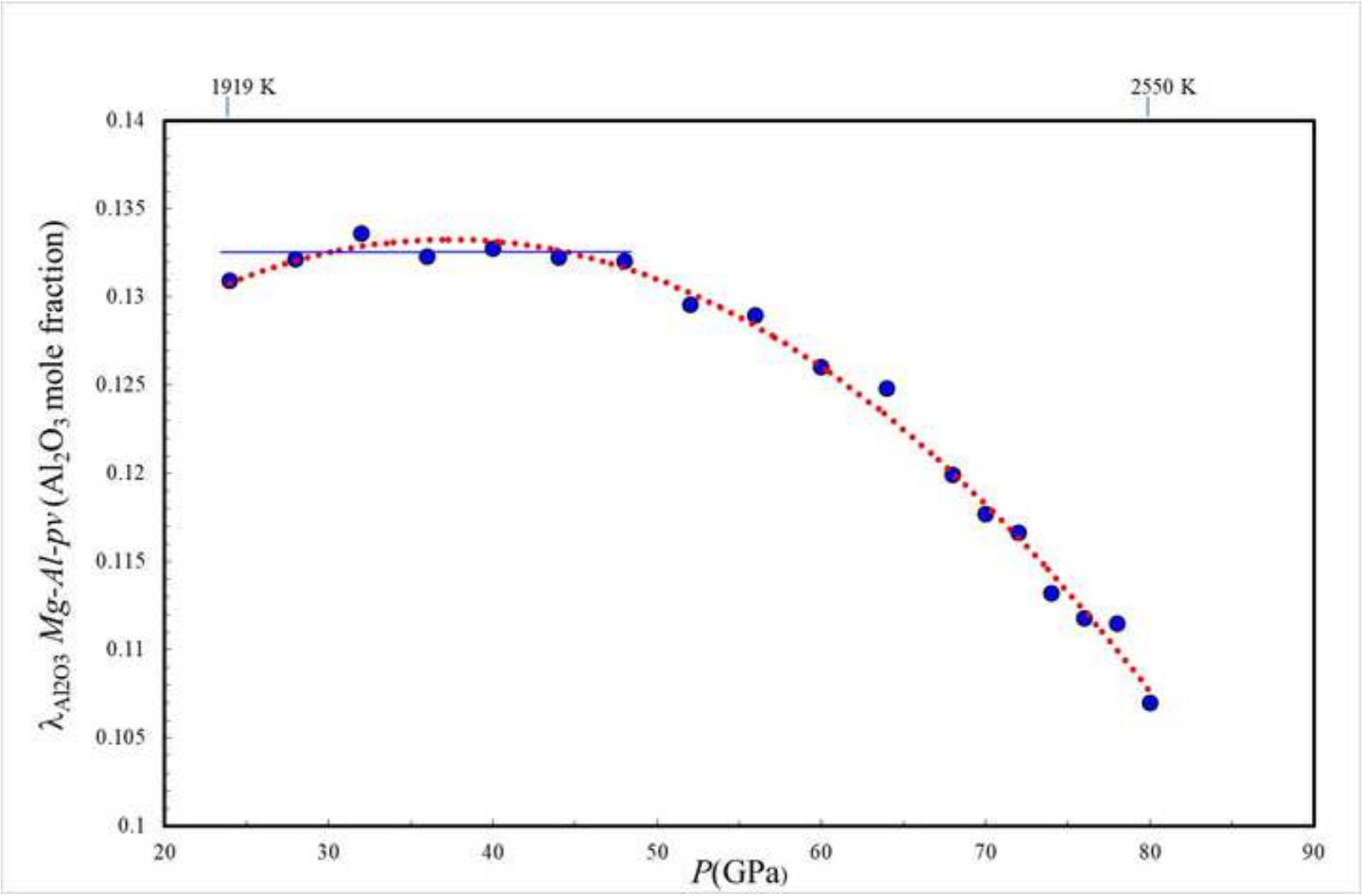

Figure 6

Click here to download high resolution image

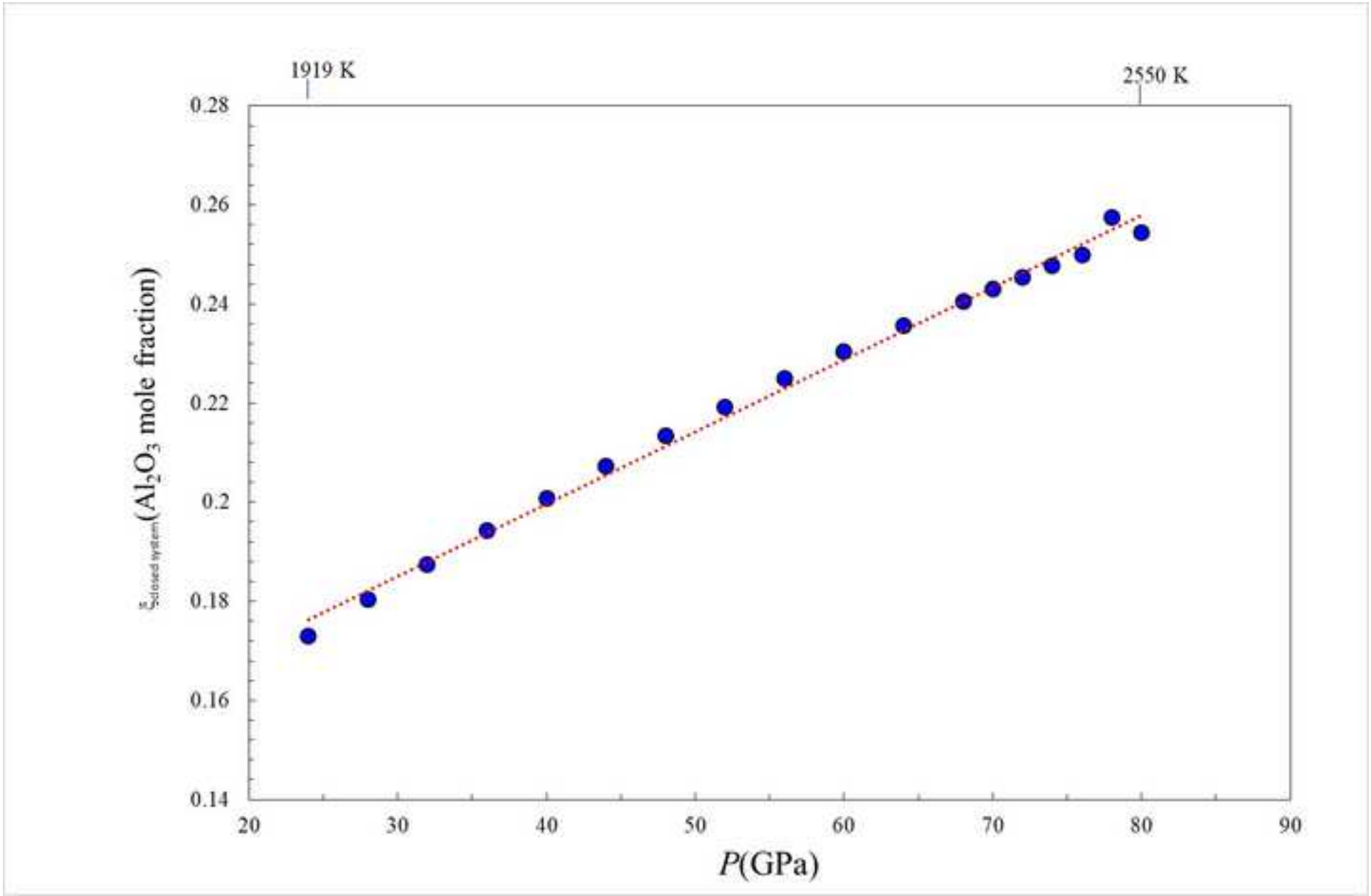

Figure 7

Click here to download high resolution image

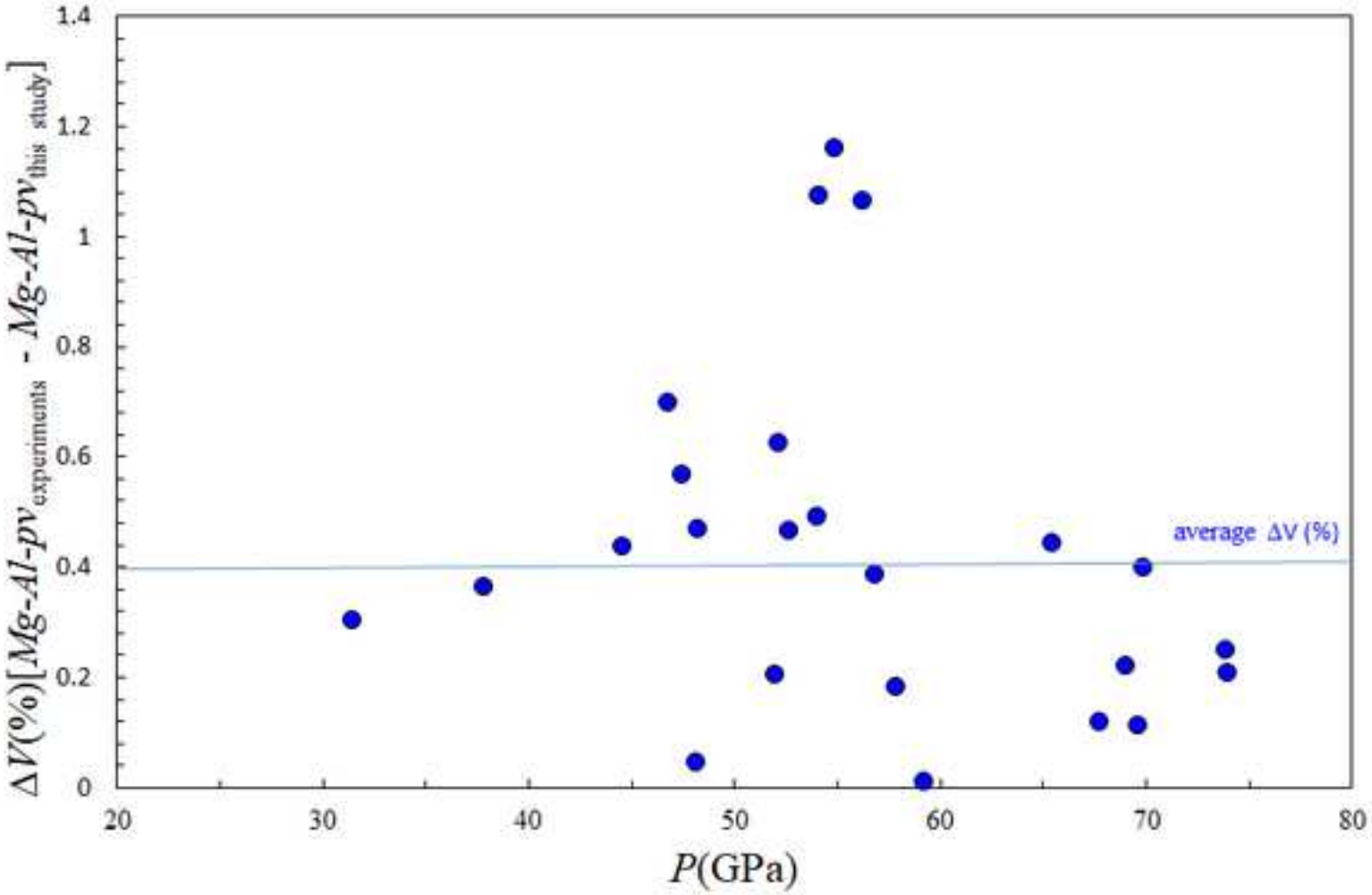

Figure 8

Click here to download high resolution image

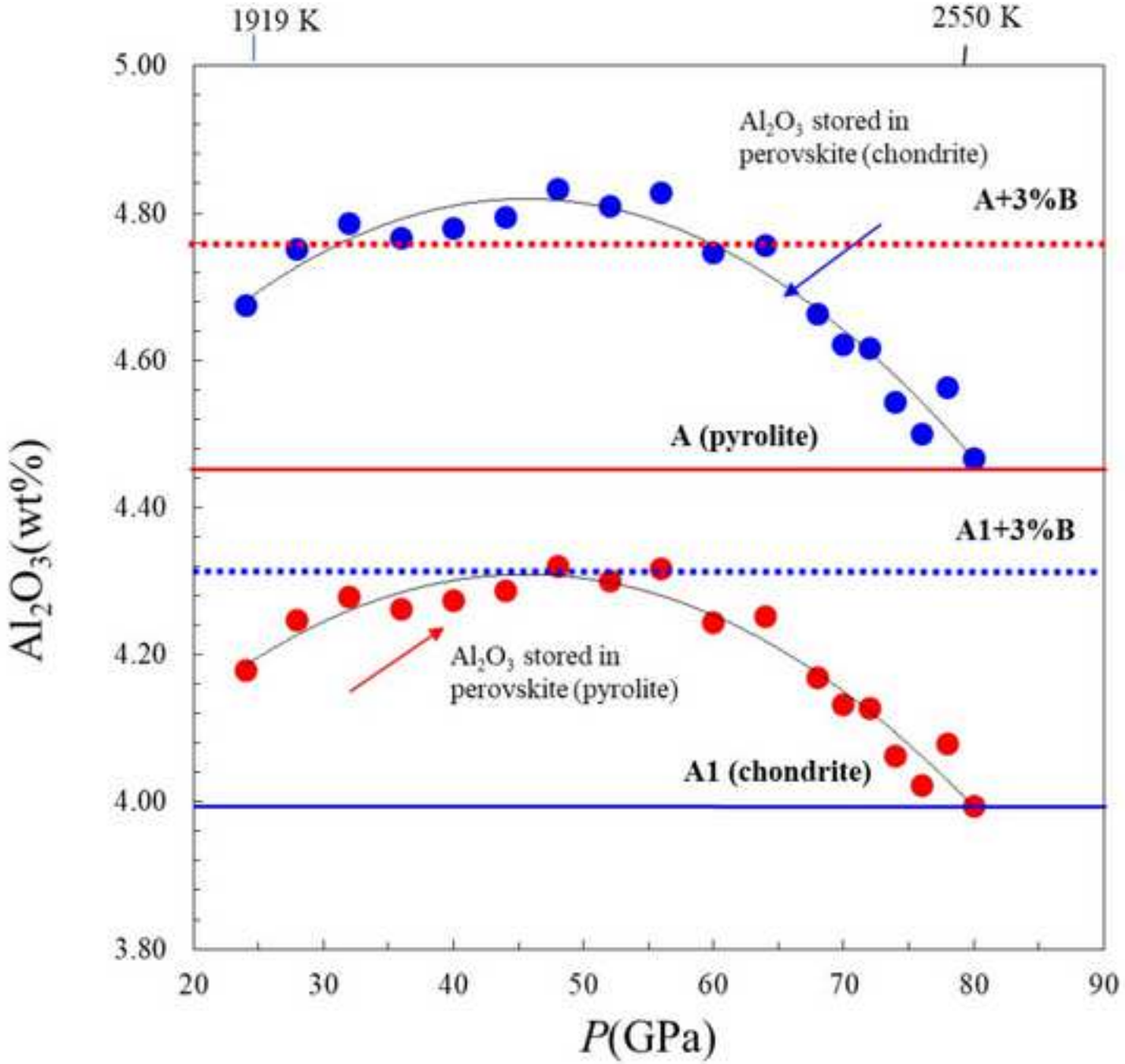

Figure 9

Click here to download high resolution image

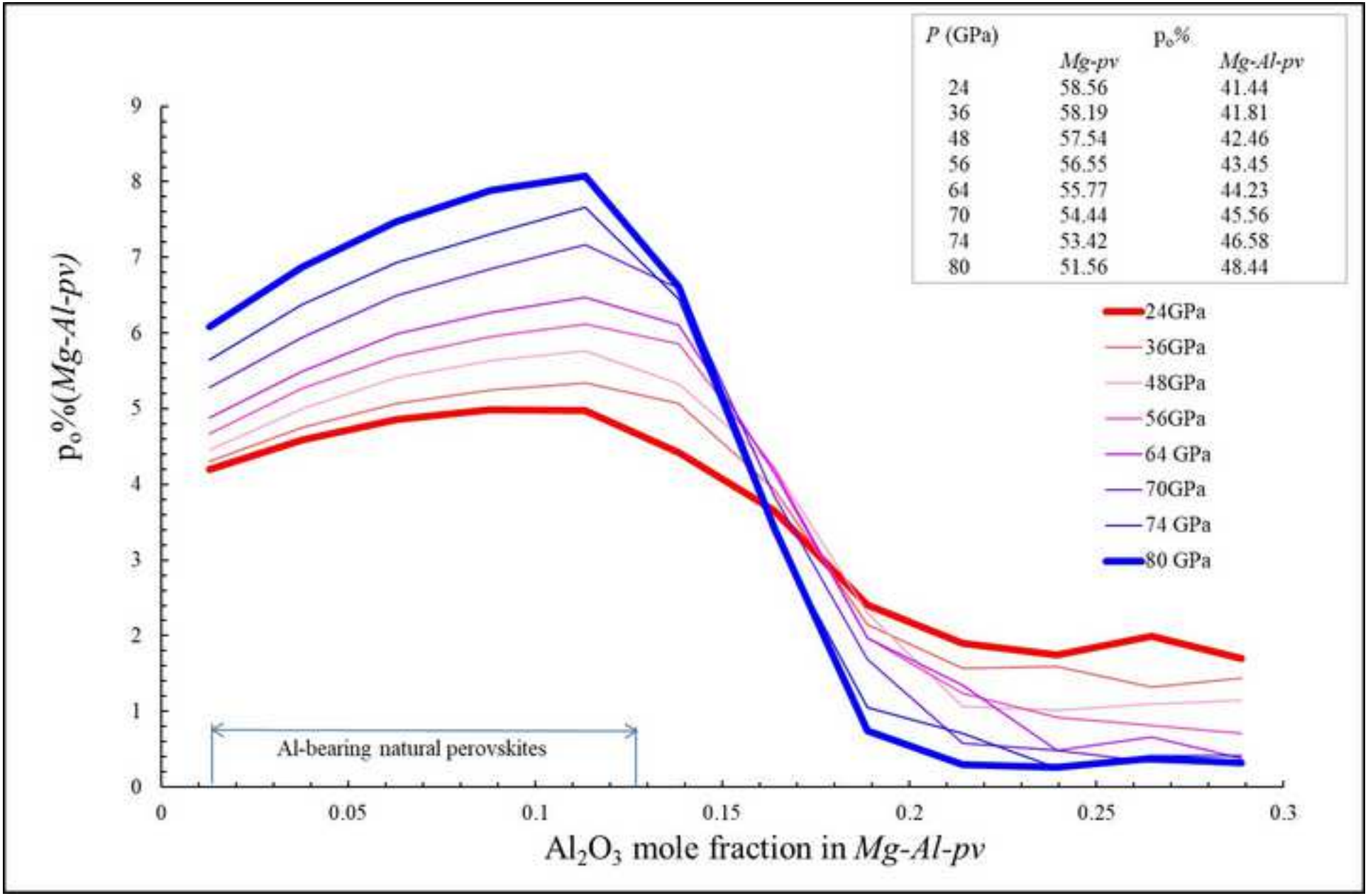

***Declaration of Interest Statement**

0.3 upper-x

P	T	K
24	1919	1.8701
28	1964	1.8972
32	2009	1.9226
36	2054	1.9479
40	2100	1.9745
44	2145	2.0036
48	2190	2.0367
52	2235	2.0753
56	2280	2.1207
60	2325	2.1746
64	2371	2.2387
68	2416	2.3149
70	2438	2.3582
72	2461	2.4053
74	2484	2.4566
76	2506	2.5125
78	2829	2.5396
80	2551	2.6393

P	T	X	K
24	1919	0.0005	0.7937262
24	1919	0.0105	0.9293135
24	1919	0.0205	1.0568378
24	1919	0.0305	1.1839746
24	1919	0.0405	1.3111602
24	1919	0.0505	1.4376564
24	1919	0.0605	1.5622545
24	1919	0.0705	1.6835027
24	1919	0.0805	1.7998221
24	1919	0.0905	1.9095857
24	1919	0.1005	2.0111818
24	1919	0.1105	2.1030729
24	1919	0.1205	2.1838465
24	1919	0.1305	2.2522621
24	1919	0.1405	2.3072891
24	1919	0.1505	2.3481417
24	1919	0.1605	2.3742988
24	1919	0.1705	2.38552
24	1919	0.1805	2.3818495
24	1919	0.1905	2.3636093
24	1919	0.2005	2.3313859
24	1919	0.2105	2.2860057
24	1919	0.2205	2.2285073
24	1919	0.2305	2.1601033

0.1705	2.3855